14-year acceleration along the Japan trench and the Sagami trough

Lou Marill[1], David Marsan[2], Anne Socquet[3], Mathilde Radiguet[1], Nathalie Cotte[4], and Baptiste Rousset[5]

[1]ISTerre
[2]Universite de Savoie Mont Blanc
[3]Université Grenoble Alpes, ISTerre
[4]University Joseph Fourier / CNRS
[5]University of California, Berkeley

November 21, 2022

Abstract

An acceleration of the background seismicity and a shortening of the slow slip events on the Boso peninsula (Japan) recurrence intervals suggest a slow decoupling of the Philippine Sea-North America (PHS-NAM) subduction interface from 1990 to 2011. Motivated by these observations, we used GPS (Global Positioning System) time series to study the 14-year evolution of interface coupling offshore Honshu with a specific focus on the Kanto region. We processed the GPS data in double difference and analyze them with a trajectory model that accounts for seismic and aseismic variations, and that includes an inter-seismic acceleration term. We inverted the surface acceleration obtained, on both the Pacific-North America (PAC-NAM) and the PHS-NAM interfaces. The inverted slip rate changes over time compares well with previous studies: we observe slip deceleration between 39$ˆo$-41$ˆo$ N and slip acceleration between 37$ˆo$-39$ˆo$ N, with a maximum amplitude of 3.45 mm/yr$ˆ2$ corresponding to an equivalent geodetic coupling change of 0.64. Our analysis reveals a novel and robust slip acceleration South of 36.5$ˆo$ N that we interpret as a decoupling of the PAC-NAM interface. It is located noticeably far from the 2011 Tohoku earthquake rupture and is therefore unlikely connected to it. We link the slip rate changes to the background seismicity changes and retrieve the slip acceleration from either the seismicity rate or the surface displacement. Our results further demonstrate that inter-seismic slip rate can significantly evolve over years to decades, and suggest a simple relationship between the background seismicity and the slip on the subduction interface.

14-year acceleration along the Japan trench and the Sagami trough

Lou Marill[1], David Marsan[1], Anne Socquet[1], Mathilde Radiguet[1], Nathalie Cotte[1], and Baptiste Rousset[2]

[1]Univ. Grenoble Alpes, Univ. Savoie Mont Blanc, CNRS, IRD, Univ. Gustave Eiffel, ISTerre, 38000 Grenoble, France
[2]Univ. Calif. Berkeley, Dept. Earth & Planetary Sci., Berkeley, CA 94720 USA

Key Points:

- We reveal a novel and robust acceleration of the fault slip for the Pacific plate underneath the Boso peninsula and offshore Kanto.
- This slip acceleration is coherent with the observed shortening of reccurrence times of the Boso slow slip events.
- We propose a simple relationship that relates observed changes in background seismicity ratxe and in slip rate along the Japan trench.

Corresponding author: Lou Marill, lou.marill@univ-smb.fr

Abstract

An acceleration of the background seismicity and a shortening of the slow slip events on the Boso peninsula (Japan) recurrence intervals suggest a slow decoupling of the Philippine Sea-North America (PHS-NAM) subduction interface from 1990 to 2011. Motivated by these observations, we used GPS (Global Positioning System) time series to study the 14-year evolution of interface coupling offshore Honshu with a specific focus on the Kanto region. We processed the GPS data in double difference and analyze them with a trajectory model that accounts for seismic and aseismic variations, and that includes an inter-seismic acceleration term. We inverted the surface acceleration obtained, on both the Pacific-North America (PAC-NAM) and the PHS-NAM interfaces. The inverted slip rate changes over time compares well with previous studies: we observe slip deceleration between 39^o-41^o N and slip acceleration between 37^o-39^o N, with a maximum amplitude of 3.45 mm/yr^2 corresponding to an equivalent geodetic coupling change of 0.64. Our analysis reveals a novel and robust slip acceleration South of 36.5^o N that we interpret as a decoupling of the PAC-NAM interface. It is located noticeably far from the 2011 Tohoku earthquake rupture and is therefore unlikely connected to it. We link the slip rate changes to the background seismicity changes and retrieve the slip acceleration from either the seismicity rate or the surface displacement. Our results further demonstrate that inter-seismic slip rate can significantly evolve over years to decades, and suggest a simple relationship between the background seismicity and the slip on the subduction interface.

1 Introduction

A common assumption regarding to the seismic cycle is to consider the inter-seismic strain rate as being constant over time (Savage & Thatcher, 1992). Recently, long-term changes in slip rate, or interface coupling, have been observed or suggested in the context of subduction zones. Long-term slow slip events (L-SSEs) with a duration of a few years have been documented in Alaska (duration of 2 to 9 years) (Li et al., 2016; Rousset et al., 2019) and in various regions of Japan (Tokai district, Kii peninsula and Bungo channel, duration from 1 to 5 years) (Hirose et al., 1999; Kobayashi, 2014; Kobayashi & Tsuyuki, 2019; Miyazaki et al., 2003; Ochi & Kato, 2013; Ozawa et al., 2001, 2013; Ozawa, Suito, Imakiire, & Murakmi, 2007; Yagi & Kikuchi, 2003; Yoshioka et al., 2015). Variations at even longer time scales (decades) have also been observed. In Sumatra, Prawirodirdjo et al. (2010) measure an increase of coupling between the 1990s and 2010 in the Batu and Enggano islands. Based on coral observations that allow the estimation of relative sea level changes, Meltzner et al. (2015) find an increase in coupling starting 20-40 years before the 1861 M_w 8.5 earthquake in southern Simeulue (Newcomb & McCann, 1987) and, on the opposite, a L-SSE lasting 15 years before the 2005 M_w 8.6 earthquake in the Banyak islands. In Japan, Hasegawa and Yoshida (2015), Heki and Mitsui (2013), Loveless and Meade (2016), Mavrommatis et al. (2014, 2015) and Yokota and Koketsu (2015) observe slip rate variations over 15 years along the Japan Trench before the 2011 Tohoku earthquake. At the Mendocino triple junction, Materna et al. (2019) document slip rate variations between four $M \geq 6.5$ regional earthquakes from 2005 to 2019. In South America, Melnick et al. (2017) and Ruiz et al. (2017) identified a change in loading rate likely triggered by the 2010 M_w 8.8 Maule earthquake. This change is seen up to the 2015 M_w 8.3 Illapel earthquake North of Maule rupture (Melnick et al., 2017) and up to the 2016 M_w 7.6 Chiloé earthquake South (Ruiz et al., 2017).

While long past changes in slip rate or seismic coupling are particularly challenging to infer from in situ observables in subduction zones, continental faults are easier to study for that purpose. Slip rates can be inferred for the Pleistocene-Holocene periods using for instance geological mapping, cosmogenic nuclide geochronology, displaced alluvial fans measurements, Lidar mapping, and/or differential GPS (Global Positioning System) fault scarp surveys. Foy et al. (2012), Ganev et al. (2012), Oskin et al. (2008)

and Rust et al. (2018) compare Pleistocene-Holocene and current slip rates for several continental faults and observe long-term variations: at the Garlock (California) and the Talas-Fergana (Himalayas) faults the slip rate is currently twice lower than the average Quaternary rate, while on the contrary the slip rate is currently twice higher in the Mojave Desert and the Clayton Valley (California).

The mechanisms responsible for such variations in inter-seismic slip rate at the decadal time scale are yet to be understood. Since they overlap the time scale of post-seismic, and, more generally, of crustal and upper-mantle visco-elastic relaxation processes, they could be related to recent earthquakes and mega-thrust earthquakes, as previously suggested by Heki and Mitsui (2013) or Melnick et al. (2017). Variations that precede, rather than follow, large earthquakes are yet to be interpreted in terms of dynamical processes, which could conceivably be similar to those controlling SSEs of much shorter durations. In any case, dynamical modelling and physical understanding of these phenomena first require well constrained kinematic observations.

We here present a study of inter-seismic slip rate changes at the Japan trench and the Sagami through subduction zones (Figure 1), from January 1997 to February 2011. As large scale variations in geodetic movements can be caused by reference frame issues, a first goal of this study is to provide a full re-analysis of the Japanese GPS data that is completely independent from the F3 solution (Nakada et al., 2005) on which are based previous studies of decadal slip rate variations (Mavrommatis et al., 2014; Yokota & Koketsu, 2015). The other goal is to complement the observations of Mavrommatis et al. (2014) and Yokota and Koketsu (2015) by extending the investigation of the surface displacements to the Kanto region (Figure 1). This region is known to have undergone a strong acceleration of the background seismicity rate (Marsan et al., 2017; Reverso et al., 2016), as well as a shortening of the Boso slow slip events recurrence times from 1996 to 2014 (Fukuda, 2018; Hirose et al., 2012; Ozawa, 2014). These observations suggest that plate decoupling, involving the three tectonic plates that control surface deformation in Kanto, has been going on for at least a decade before the 2011 M_w 9.0 Tohoku earthquake. Given the distance between the Kanto region and potential mainshock candidates that could possibly explain the northern Honshu changes in slip rate (namely, the 2003 M_w 8.3 Tokachi earthquake, see Figure 1), any variation in local slip rate in Kanto could not be conceivably related to unmodeled post-seismic processes of such mainshocks. The Kanto region is therefore a natural candidate for possible decadal slip rate variations.

In more details, this study complements the analyses of Mavrommatis et al. (2014) and Yokota and Koketsu (2015) by (1) performing a re-analysis of the GPS data, (2) including the Kanto region, and (3) testing the sensitivity of the inverted changes in slip rate relative to the inclusion of slip on the Philippine Sea plate, of different a priori distributions, including a seismicity-based prior, and of GPS vertical components. After summarizing the tectonic setting of the Honshu island (Section 2), we describe our processing and analysis of GPS data (Section 3) as well as the inversion of slip rate distribution (Section 4). We then analyze the mean surface velocity and the acceleration fields, and invert for inter-seismic coupling and the on-fault slip acceleration (Section 5). We discuss the robustness of our obtained slip acceleration and its relationship with regional seismicity (Section 6), and finally interpret the results in light of both the subsequent rupture of the 2011 M_w 9.0 Tohoku earthquake and the clear acceleration in the wider Kanto region (Section 7).

2 Honshu tectonic setting

The subduction of the Pacific (PAC) plate beneath the North America (NAM) plate induced the following great instrumental earthquakes: the 1994 M_w 7.7 Sanriku earthquake (A. Ito, 2004), the 2003 M_w 8.0 Tokachi earthquake (Yamanaka & Kikuchi, 2003) and the 2011 M_w 9.0 Tohoku earthquake (Hooper et al., 2013) (Figure 1). While the 1994

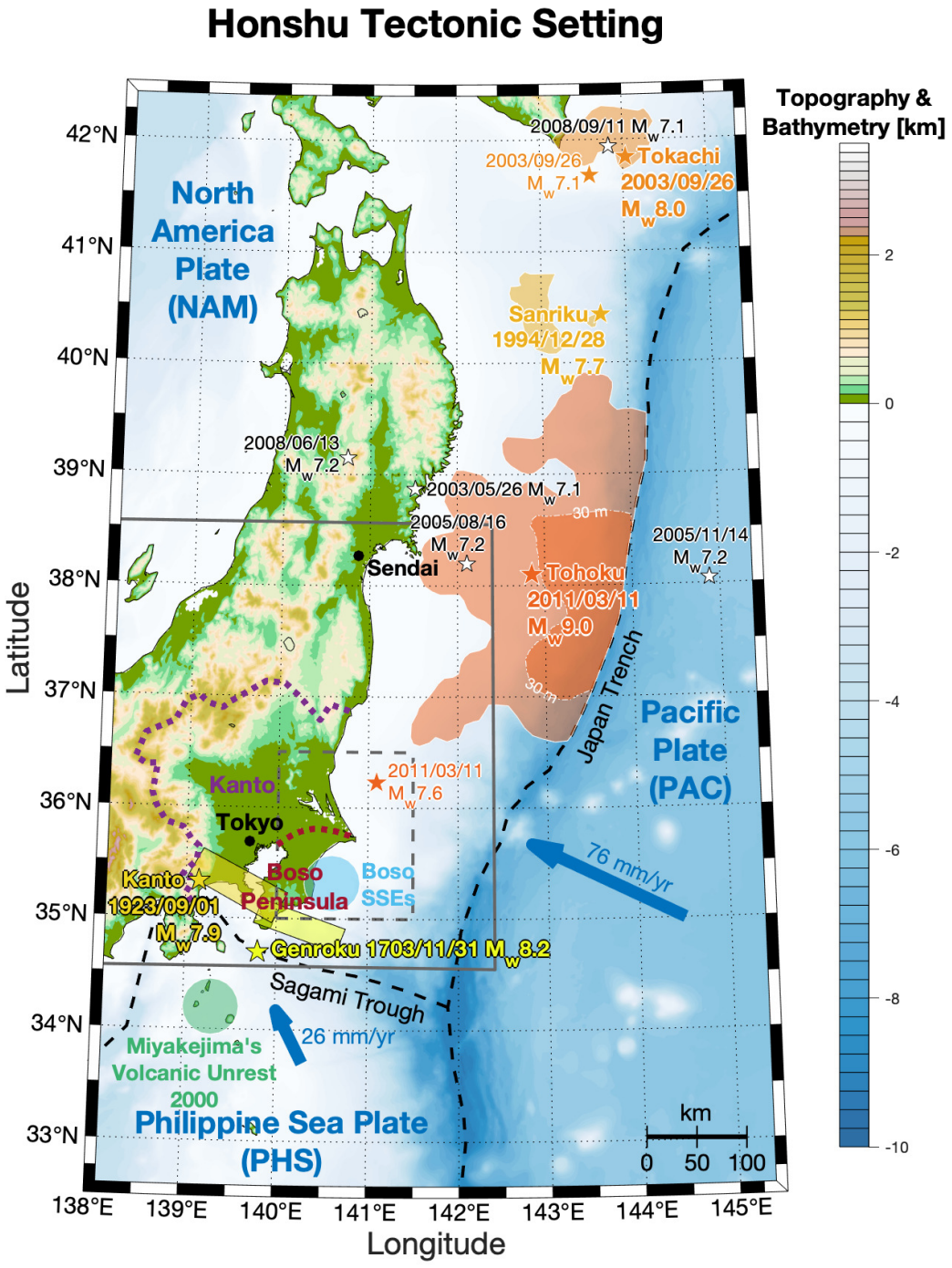

Figure 1. Tectonic setting of Honshu island. The colored stars represent the historical and instrumental great earthquakes, $M_w \geq 7.7$, as well as major aftershocks; format date is year/month/day; ruptured areas are also indicated (same color as the corresponding star) (Hooper et al., 2013; A. Ito, 2004; Komori et al., 2017; Shishikura, 2014; Yamanaka & Kikuchi, 2003). The white stars represent the $M_w \geq 7.1$ earthquakes occurring between 1996 and 2011. The blue circle represents the Boso SSEs rupture area (Fukuda, 2018). The green circle represents the location of the 2000 Miyakejima volcanic unrest (Cattania et al., 2017). The continuous gray square is the Figure 2a zoom and the dashed gray square is the Figure 9a zoom. Plate motions are deduced from Nishimura et al. (2007)'s Euler poles.

Sanriku and the 2003 Tokachi earthquakes mostly affected the northern part of Honshu and Hokkaido, the 2011 Tohoku earthquake ruptured a large part of the Japan trench and impacted all the North of Honshu, the rupture itself terminating not far from the Kanto region. Two great known historical earthquakes struck the Kanto region, at the interface between the Philippine Sea (PHS) plate and the NAM plate: the 1703 M_w 8.2 Genroku Kanto earthquake (named Genroku in Figure 1) and the 1923 M_w 7.9 Taisho Kanto earthquake (named Kanto in Figure 1) (Komori et al., 2017; Shishikura, 2014). These two earthquakes outline resisting asperities on the PHS plate which are expected to appear as strongly coupled in coupling models. Komori et al. (2017) and Shishikura (2014) show that great earthquakes along the Sagami Trough have a recurrence interval between 250 and 800 years. As both earthquakes ruptured near Tokyo, any forthcoming occurrence of one of these earthquakes could have disastrous consequences.

Recurrent SSEs have been occurring offshore Boso peninsula with a recurrence interval of ∼6 years between 1983 and 2007 (Ozawa, Suito, & Tobita, 2007). These SSEs ruptured roughly the same area (blue circle in Figure 1), had a characteristic size ($M_w \sim$ 6.6) and lasted from 14 days (in 1996 and 2007) to 43 days (in 2002) (Fukuda, 2018). Fukuda (2018), Hirose et al. (2012) and Ozawa (2014) suggest that a shortening of the Boso SSE recurrence interval took place between 1996 and 2014, which can be seen as the signature of an increasing loading in this area. Finally, an important volcanic unrest, with a major caldera collapse, happened around Miyakejima island in 2000 (thereafter named the 2000 Miyakejima volcanic unrest, see Figure 1) (Cattania et al., 2017; T. Ito & Yoshioka, 2002). It was associated with an intense seismicity swarm: over 100,000 earthquakes occurred in a 2-month period, including five $M_w > 6.0$ earthquakes (T. Ito & Yoshioka, 2002) for a total seismic moment release estimated to $M_0 = 3.6 \times 10^{19}$ N.m (Cattania et al., 2017). This volcanic collapse was large enough to impact the surface displacement of the North America plate up to 30^o N, and produced a large transient deformation with centimetric displacements recorded on the Boso peninsula.

To determine the velocity of the PAC and PHS plates relative to the NAM plate, we use the Euler poles from Nishimura et al. (2007), given in Table 1. Using this Euler poles, we can computed the velocity of the PAC and the PHS plates relative to the NAM plate at each point. The average velocity is taken as the reference plate velocity, and we obtain for PAC, $v_{PAC} \approx 76$ mm/yr, and for PHS, $v_{PHS} \approx 26$ mm/yr.

Table 1. Euler Rotation Poles

Plate	Reference Plate	Latitude (deg)	Longitude (deg)	Rotation Rate (deg/Ma)
NAM*	EUR	75.85	130.92	-0.351
PAC	EUR	63.10	79.20	-0.919
PHS	EUR	36.61	138.96	-9.956

Note: From Nishimura et al. (2007).
Abbreviations: NAM: North America plate; PAC: Pacific plate;
PHS: Philippine Sea plate; EUR: Eurasia plate.
*NAM correspond to the Central Japan Block (CJB) in Nishimura et al. (2007).

3 Data processing and analysis

3.1 Data processing

The 1421 stations of the GNSS (Global Navigation Satellite System) Earth Observation Network System in Japan and 44 IGS (International GNSS Service, http://igscb.nasa.jpl.org)

sites worldwide, were processed over the 1997-2011 period following a double difference approach using the GAMIT/GLOBK software suite (Herring et al., 2015, 2018a, 2018b). As in Herring et al. (2016), we assemble our stations into sub-networks for the daily processing. We reduce 24-hour measurement sessions to daily estimates of station position, choosing the ionosphere-free combination and fixing the ambiguities to integer values. We use precise orbit positions from the IGS, precise EOP (Earth Orientation Parameters) from the IERS (International Earth Rotation and Reference Systems Service) bulletin B (monthly), phase centers of the antennas from IGS tables, ocean-tidal loading corrections from the FES2004 (Finite Element Solution) model, as well as atmospheric loading corrections (tidal and non-tidal). Using the Vienna Mapping Function (Boehm et al., 2006), we estimate one tropospheric zenith delay parameter every 2h, and one couple of horizontal tropospheric gradients per 24h session. We combine the daily sub-network solutions in a regional stabilisation approach (Herring et al., 2015). Then, we generate coordinate time series and map them into the ITRF2014 (International Terrestrial Reference Frame) reference frame (Altamimi et al., 2017) by applying Helmert transforms to adjust IGS station coordinates to those defined in the ITRF in a least square iterative process, using the PYACS (Python Yet Another Combination Software) Python module (Tran, 2009). We then identified and removed the outliers of the generated time series: individual values differing by 15 mm or more from the median value within a 20-day sliding window. Thereafter, the time series are those without outliers.

3.2 Earthquakes and slow deformation events affecting the time series

In order to relate large earthquakes to potential co-seismic jumps and post-seismic transients in the GPS time series, we make use of the ISC (International Seismological Centre) earthquake catalog limited to $M_w \geq 6.4$ earthquakes around Japan (from 28.6^o to 47.4^o N, and from 126.5^o to 149.2^o E). This moment magnitude (M_w) threshold allows to keep only earthquakes with a visible influence on the time series, and avoids over-fitting. For all earthquakes, we use the M_w estimated by the Japan Meteorological Agency. The GPS time series can also be affected by slow deformation transients, defined as either (1) the Boso slow slip events (SSEs) (Fukuda, 2018), or (2) the 2000 Miyakejima volcanic unrest (Cattania et al., 2017; Nakada et al., 2005; Uhira et al., 2005). The parameters considered for the modelling of those slow deformation events are summarized in Table 2.

Table 2. Characteristics of the slow deformation events

Event type	Starting date (t_s) (year/month/day)	Center position (latitude ; longitude)	M_w	Duration (t_d) (days)
Boso SSE	2002/10/02	35.30 ; 140.70	6.67	43
Boso SSE	2007/08/12	35.35 ; 140.40	6.65	14
Miyakejima volcanic unrest	2000/06/26	34.20 ; 139.30	7.00*	64

Notes: Boso slow slip events (SSEs) from Fukuda (2018); the 2000 Miyakejima volcanic unrest from Cattania et al. (2017), Nakada et al. (2005) and Uhira et al. (2005).
*Computed from the total moment release: $M_0 = 3.6 \times 10^{19}$ N.m (Cattania et al., 2017).

3.3 Time series analysis with a trajectory model

We select the 299 stations located in Honshu with a longitude greater than 139^o E. This way, we focus our analysis on the Honshu island, including the Kanto region. Most of our selected stations are in common with Loveless and Meade (2010), Mavrommatis et al. (2014) and Yokota and Koketsu (2015). To model the surface displacements from

GPS time series, we use a modified version of the trajectory model of Bevis and Brown (2014) based on Jara et al. (2017):

$$\begin{aligned} x(t) &= x_R + v(t-t_R) + \frac{1}{2}a(t-t_R)^2 + \sum_{k=1}^{2}\left[s_k \sin\left(2k\pi(t-t_R)\right) + c_k \cos\left(2k\pi(t-t_R)\right)\right] \\ &+ \sum_{a=1}^{n_A} b_a \mathrm{H}(t-t_a) + \sum_{j=1}^{n_J} c_j \mathrm{H}(t-t_j) + \sum_{s=1}^{n_S} d_s \mathrm{J}(t-t_s) \\ &+ \sum_{i=1}^{n_I} m_i \mathrm{H}(t-t_i) \times \log\left(1 + \frac{t-t_i}{T_R}\right) \end{aligned} \tag{1}$$

where t is time, t_R is the reference time (01/01/1997), x_R is the reference position, v is the initial velocity (or the inter-seismic velocity if a is fixed to 0), and a is the inter-seismic acceleration; $\sum_{k=1}^{2}\left[s_k \sin\left(2k\pi(t-t_R)\right) + c_k \cos\left(2k\pi(t-t_R)\right)\right]$ corresponds to the annual ($k=1$) and semi-annual ($k=2$) seasonal model; $\sum_{a=1}^{n_A} b_a \mathrm{H}(t-t_a)$ accounts for the antenna jumps, where n_A is the number of antenna changes at the station, b_a is the amplitude associated to the Heaviside function H, and t_a is the antenna change time; $\sum_{j=1}^{n_J} c_j \mathrm{H}(t-t_j)$ corresponds to the co-seismic jumps model, where n_J is the number of earthquakes influencing the station, c_j, the amplitude associated to H, and t_j, the earthquake time; $\sum_{s=1}^{n_S} d_s \mathrm{J}(t-t_s)$ corresponds to the slow deformations model, where n_S is the number of slow deformation events influencing the station, d_s, the amplitude associated to the function J (explicited hereafter), and t_s, the slow deformation starting time (see Table 2); and $\sum_{i=1}^{n_I} m_i \mathrm{H}(t-t_i) \times \log\left(1 + \frac{t-t_i}{T_R}\right)$ corresponds to the post-seismic transients model, where n_I is the number of earthquakes with post-seismic transients influencing the station (i.e. $n_I \leq n_J$), m_i, the amplitude of the transient, T_R, a characteristic time (fixed at 100 days, as this corresponds to the value that best fits the post-seismic signal in the time series), and t_i, the earthquake time.

For the slow deformation events listed in Table 2, we define the function J as:

$$\mathrm{J}(t-t_s) = \begin{cases} 0 & \forall t < t_s \\ -\frac{1}{2}\cos(\pi t_{norm}) + \frac{1}{2} & \forall t \in [t_s; t_s + t_d] \\ 1 & \forall t > t_s + t_d \end{cases} \tag{2}$$

where t_d is the duration of the slow deformation events (see Table 2) and $t_{norm} = \frac{t-t_s}{t_d}$.

To define the influence radius of an earthquake, we adapted the Nevada Geodetic Laboratory formula (http://geodesy.unr.edu/explanationofplots.php) into:

$$r(M_w) = 10^{0.43M_w - 0.7} \tag{3}$$

where M_w is the moment magnitude of the event, and r, the influence radius (in km) of the event. If the distance between the station and the earthquake epicenter is smaller than r, then we consider that the earthquake influences the station displacement. Similarly, in the case of SSEs, we use the moment magnitudes as given in Table 2.

For the purpose of modelling the time series, we assume that only $M_w \geq 7.1$ earthquakes (white stars in Figure 1, as well as the 2003 Tokachi earthquake and its M_w 7.1 aftershock) can produce significant post-seismic transient deformations. We fix a unique

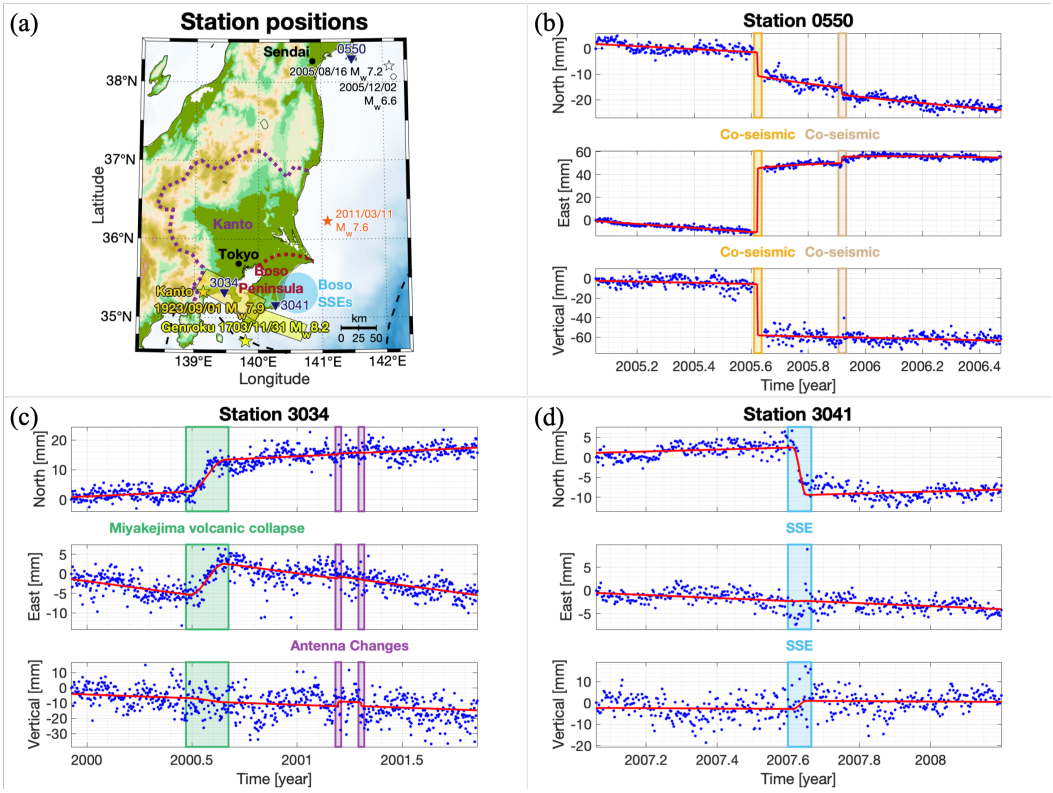

Figure 2. Examples of jumps (antenna changes, earthquakes) and slow deformation (SSEs, volcanic unrest). (a): Zoom of Figure 1 with the location of 0550 (b), 3034 (c) and 3041 (d) stations (navy triangle); . (b): Model for the 2005 M_w 7.2 Miyagi earthquake (orange rectangle, white star in (a)) with post-seismic transient and another M_w 6.6 earthquake (brown rectangle, white circle in (a)). (c): Model for the 2000 Miyakejima volcanic unrest (green rectangle) and two antenna changes (purple rectangles). (d): Model for the 2007 Boso slow slip event (cyan rectangle). In (b), (c) and (d), the blue dots represent the position time series and the red line represents the trajectory model.

characteristic time, $T_R = 100$ days, allowing a good fit of the observed post-seismic transients. We tested other T_R values and also the use of an exponential instead of a logarithmic function, and kept the model minimizing the RMSE (Root-Mean-Square Error).

The trajectory model parameters (x_R, v, a, s_k, c_k, b_a, c_j, d_s and m_i) are optimized independently for each station and component using a least-square inversion and following a three step strategy. In the first step, we compute b_a, c_j and d_s optimizing the jumps (from antenna changes and earthquakes) and slow deformation events locally, i.e., using the time series from 200 days before the event to 200 days after the end of the event (t_a, t_j or t_s) and computing:

$$x_{jump\_window}(t) = x_R + v(t - t_R) + \sum_{a=1}^{n_a} b_a \mathrm{H}(t - t_a) + \sum_{j=1}^{n_j} c_j \mathrm{H}(t - t_j) + \sum_{s=1}^{n_s} d_s \mathrm{J}(t - t_s) + \sum_{i=1}^{n_i} m_i \mathrm{H}(t - t_i) \times \log\left(1 + \frac{t - t_i}{T_R}\right) \quad (4)$$

We first proceed to a local estimate for the jumps affecting the time series. To do so, we go through the time series and take the first jump (antenna change or co-seismic) or slow deformation (hereafter considered as a "jump" also); if there is no jump in the whole time series, the program proceeds to the next step. We consider first a 400-data point window centered on the jump date (t_s). If another jump happens between the first jump and the end of the window, we extend the window with an extra 200 data points after the second jump. We keep extending the window this way until no more jump stays in the last 200 data points of the window: to illustrate this process, Figure 2c shows a window with three jumps (the 2000 Miyakejima volcanic unrest and two antenna changes). Once the window length is fixed, we fit Equation (4) within that window. As given in Equation (4), an inter-seismic velocity v and post-seismic transients are also modeled for the window, so to get the most accurate estimate of the jumps as possible. In case there is a post-seismic transient in the window, we force the transient to have the same sign as the associated co-seismic jump ($m_i \times c_j > 0$ for i and j corresponding to the same earthquake), individually for each component (NS, EW or vertical). Then, the we go to the next jump not included in the current window and starts again, until it reaches the last jump. Figure 2 illustrates how the fitting and modelling perform for some selected time windows and stations. Once we have the b_a, c_j and d_s optimized for all the jumps of the time series, we remove these jumps to obtain $x_{step1}(t)$, which is thus the time series corrected for co-seismic offsets, antenna jumps and slow transients (Table 2).

In the second step, we compute m_i by optimizing the values of the post-seismic transients using the time series from 2 years before the earthquake to 2 years after and fitting:

$$\begin{aligned} x_{post-seismic\_window} &= x_R + v\,(t-t_R) + \sum_{k=1}^{2}\left[s_k \sin\left(2k\pi\,(t-t_R)\right) + c_k \cos\left(2k\pi\,(t-t_R)\right)\right] \\ &\quad + m_i \mathrm{H}\,(t-t_i) \times \log\left(1 + \frac{t-t_i}{T_R}\right) \end{aligned} \tag{5}$$

We take 2-year data before the earthquake to estimate the seasonal and semi-seasonal terms within the window, which results in a better estimation of the post-seismic transient. We also take at most 2 years of data after the earthquake: if there is another post-seismic transient within the 2 years data then we terminate the window one day before the second post-seismic transient. To determine whether a $M_w \geq 7.1$ requires a post-seismic transient from the data, we use the Akaike Information Criterion (AIC) (Akaike et al., 1998). The AIC measures which model fits best the data among models that have different numbers of parameters. Here, we use the AIC to compare the models without and with a post-seismic transient (hence an extra parameter): for a given station, we require that at least one of the three component returns a large AIC value, while the two other components have positive AIC values (hence an improvement of the model when adding the post-seismic phase for all three components, and at least one with a very significant improvement). If this best model is indeed the one with a post-seismic transient, we remove this transient from the time series. Then, we iterate this step to all subsequent $M_w \geq 7.1$ earthquakes influencing the station and substract the modelled post-seismic transients from $x_{step1}(t)$ to obtain $x_{step2}(t)$.

In the third step, we model $x_{step2}(t)$ as:

$$x_{step2}(t) = x_R + v\,(t-t_R) + \frac{a}{2}\,(t-t_R)^2 + \sum_{k=1}^{2}\left[s_k \sin\left(2k\pi\,(t-t_R)\right) + c_k \cos\left(2k\pi\,(t-t_R)\right)\right] \tag{6}$$

and compute x_R, v, a, s_k and c_k by optimizing the seasonal and inter-seismic phenomena using the whole time series. Then we remove these contributions to get the final residuals of our raw time series.

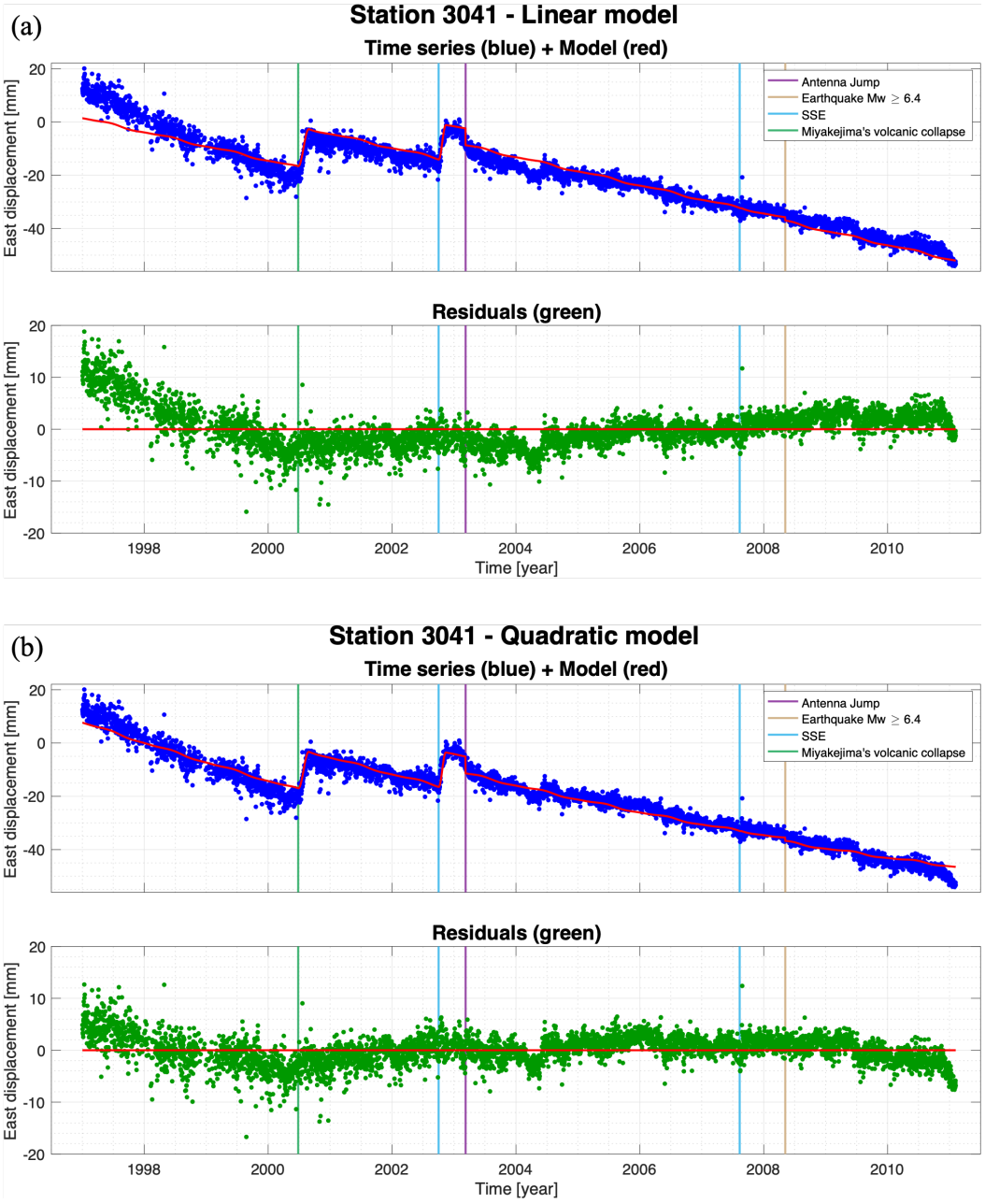

Figure 3. Linear (a) and quadratic (b) trajectory models for station 3041, from 1997 to 2011. Blue points: raw time series. Red line: trajectory model (Equation (1)). Green points: residual time series. Green line: the 2000 Miyakejima volcanic unrest. Blue lines: the 2002 and 2007 Boso slow slip events. Purple line: antenna change. Brown line: a $M_w \geq 6.4$ earthquake without post-seismic transient.

In Equation (1) we added an acceleration term (a) that is usually absent from trajectory models (Bevis & Brown, 2014). This term is motivated by the observation that the residuals of linear trajectory models ($a = 0$) very often display a decadal curvature (Figure 3a). We add a quadratic term, representative of the acceleration, to test if the inter-seismic velocity could have undergone significant changes in Honshu over the 1997-2011 period. Figure 3b shows how the curvature is accounted for with this extra term. To properly estimate the acceleration, a, we require the time series to have at least seven years of data between 1997 and 2011.

3.4 Statistical significance of the acceleration

We test the significance of adding a quadratic term using synthetic data. To generate synthetic time series, we first compute the Fourier Transform of the quadratic model residuals (Figure 3b bottom) and randomize the phase. Finally, the inverse Fourier Transform yields a synthetic time series which colored noise follows the spectral characteristics of the original residual time series. For each station individually, we generate 100 synthetic time series, compute the corresponding 100 acceleration terms within this synthetic noise, and determine the standard deviations σ_{aN} and σ_{aE} of the 100 North component and 100 East component accelerations respectively. These standard deviations represent the uncertainties on the acceleration term that can be expected from the noise in our data. They are then compared with the actual accelerations, a_N and a_E (from Equation (1)), by computing the signal-to-noise ratios $\frac{a}{\sigma_a}$ for both components. The stations for which, at least one of the two ratios, $\frac{a}{\sigma_a} > 3$ are considered as showing a significant acceleration. Finally, 187 sites present a significant acceleration, corresponding to 62% of the initial set.

4 Inversion model of the loading rate and its acceleration on the subduction interface

To determine the average coupling and the slip acceleration on the subduction interface, we perform separate least-square slip inversions (Tarantola & Valette, 1982) of the surface velocity and the acceleration fields, respectively, using a modified version of Kositsky and Avouac (2010)'s software package, including the regularization of Radiguet et al. (2011). We only use horizontal displacement time series at this stage; the addition of the vertical displacements will be discussed later (Section 5.2). The forward model is $d = Gm$, where d is the observed data (surface velocity or acceleration field), G, the transfer function matrix computed using Okada (1985), and m, the model on the fault (slip rate or its acceleration, depending on the analysis). The best model (m) is determined using the misfit function:

$$S(m) = \frac{1}{2}\left[(Gm-d)^t C_d^{-1}(Gm-d) + (m-m_0)^t C_m^{-1}(m-m_0)\right] \tag{7}$$

where m_0 is the prior model, C_m is the covariance matrix for the model parameters, C_d is the covariance matrix for the data (velocity or acceleration field), and t denotes the transpose operation. Minimizing $S(m)$ of Equation (7), we obtain the model function:

$$m = m_0 + C_m G^t \left(GC_m G^t + C_d\right)^{-1}(d - Gm_0) \tag{8}$$

4.1 Plate geometry and imposed rake

As the Kanto region (Figure 1) is characterized by a double subduction, we run two tests for each inversion (velocity and acceleration fields): (1) considering only the Pacific-North America (PAC-NAM) subduction, and (2) considering both the Philippine Sea-North America (PHS-NAM) and the PAC-NAM subductions. We discretize the faults into triangular sub-fault patches of ∼15 km size. For the PAC plate interface, we use the Kamchatka-Kuril Island-Japan region of the Slab 2 model (Hayes et al., 2018). We keep

only the part from the Sagami Trough (∼34.2^o N, see Figure 1) to the North of Honshu island (∼41^o N), and from the trench down to 90 km depth. For the PHS plate interface, we use Ishida (1992)'s model. We impose a fixed rake angle for each sub-fault. To determine this angle, we compute the PAC and PHS plate velocity vectors relative to the NAM plate at each sub-fault using the Euler poles given in Table 1. Then, we determine the rake, which will be different for each sub-fault, by projecting the velocity vector direction on the sub-fault surface.

4.2 Data covariance matrix

The data covariance matrix (C_d) is a diagonal matrix whose dimension is twice the number of stations, since there are two horizontal channels per station. The diagonal values are determined by the data uncertainties for the North and East components:

$$\forall\ 0 \leq i \leq n_{sta} - 1, \begin{cases} C_d\left(2i+1, 2i+1\right) = \left(errE_i\right)^2 \\ C_d\left(2i+2, 2i+2\right) = \left(errN_i\right)^2 \end{cases} \tag{9}$$

where i is the index of the station, n_{sta} is the number of stations, $errN_i$, the uncertainty of the data i according to the North component, and $errE_i$, the uncertainty of the data i according to the East component.

The 5% and 95% quantiles of the velocity uncertainties are found at 0.16 and 0.36 mm/yr, respectively, with a mean of 0.23 mm/yr. As acceleration uncertainties, we take the standard deviation of the acceleration computed from the synthetic time series (see Section 3.4). The 5% and 95% quantiles of the acceleration uncertainties are found at 0.020 and 0.158 mm/yr^2, respectively, with a mean of 0.080 mm/yr^2.

4.3 Model covariance matrix

The model covariance matrix (C_m) introduces two meta-parameters: the standard deviation of the model parameters (σ_m) and the correlation length (λ). We define $C_m\left(i,j\right)$, the elements of the model covariance matrix between the sub-faults i and j, based on Radiguet et al. (2011):

$$C_m\left(i,j\right) = \sigma_m^2 \times \left(\frac{1}{1+\frac{\lambda}{\lambda_0}}\right)^2 \exp\left(-\frac{d\left(i,j\right)}{\lambda}\right) \tag{10}$$

where λ_0 is a scaling factor fixed to the characteristic sub-fault size (15 km), and $d(i,j)$ is the distance between the centers of sub-faults i and j. The correlation length λ prescribes the distance over which the slip is correlated, and therefore controls the smoothing of the model. For the PAC plate, we use $\lambda = 50$ km corresponding to three times the sub-fault size. For the PHS, we use $\lambda = 180$ km to avoid over-fitting and trade-off issues, as explained later (Section 4.5).

The standard deviation σ_m controls the trade-off between the quality of the fit and the departure from the a-priori model (m_0). We choose σ_m using a L-curve, namely: L_∞ norm vs χ^2. The L_∞ norm of the cumulative slip reflects the model roughness, and is defined as:

$$L_\infty = \max(|m - m_0|) \tag{11}$$

while χ^2 measures the quality of the fit, and is defined as:

$$\chi^2 = \frac{1}{2n_{sta}} \times \left(Gm - d\right)^t C_d^{-1} \left(Gm - d\right) \tag{12}$$

For the velocity field inversion, we take $\sigma_m = 10^{0.79}$ to limit the slip rate maximum to the plate velocity. The L-curve in Supplementary Figure S1 shows that the lowest χ^2 for $L_\infty \geq 76$ mm/yr is obtained for $\sigma_m = 10^{0.79}$. We set the σ_m value for the

acceleration inversion based on an argument that relates this value with the $\sigma_m = 10^{0.79}$ value used for the slip rate inversion. We will show later (Figure 7 and Section 6.3) that the maximum change in seismic coupling C between 1997 and 2011 amounts to $\Delta C = 0.66$. Given the convergence rate of 76 mm/yr for PAC and NAM, this is equivalent to an acceleration of 3.45 mm/yr^2 at maximum, over 14 years. We therefore smooth the inverted slip acceleration so that it can reach 3.45 mm/yr^2 at maximum, hence $L_\infty \geq$ 3.45 mm/yr^2. Given this constraint, the L-curve (Supplementary Figure S2) gives $\sigma_m = 10^{0.02}$ for the acceleration inversion. We finally notice that the χ^2 values are large ($\chi^2 =$ 273 and $\chi^2 = 21$ for the slip rate and the acceleration, respectively), which is due to the relatively small uncertainties we obtain. The latter are likely under-estimated since they only account for estimation, not model, errors. We however use them anyway as they allow to weight (in a relative sense) the inversion; absolute values of χ are therefore of little use here.

4.4 Slip restitution

For each inversion, we evaluate the resolution by assessing the ability of each sub-fault to resolve a unit slip. We compute the surface displacements caused by a unit slip located on one sub-fault, and invert these displacements using the parameterization previously explained, to obtain a field of slip values. The associated resolution matrix from Tarantola and Valette (1982) is:

$$R = C_m G^t (G C_m G^t + C_d)^{-1} G \tag{13}$$

The resolution matrix diagonal values range from 0 if the slip is not resolved, to 1 if it is fully resolved. Rather than the resolution itself, we look at the restitution index of the sub-faults corresponding to the sum of R along each row, ranging from 0 to 1.5 (Supplementary Figure S3 for the slip rate and Supplementary Figure S4 for the slip acceleration). We display with gridded meshes the sub-faults with less than 90% of the slip restored.

4.5 Prior model

At first, we use a null prior model, i.e., (1) a fully uncoupled model for the coupling, hence slip rates equal to the convergence rate, and (2) a zero acceleration model for the slip acceleration. We additionally test a fully coupled prior model (Supplementary Figure S5): this prior brings only small differences in the well restored area of the PAC plate. However, while changing the PHS plate prior model does not affect the inverted PAC interface coupling, the PAC plate prior model impacts the inverted PHS interface coupling (as shown by comparing Figure 4, Supplementary Figure S6 and Supplementary Figure S7). Because of this sensitivity to the PAC prior, we must keep in mind that the results for PHS plate are to be taken with caution.

For the slip acceleration, we test a prior model based on the seismic acceleration observed by Marsan et al. (2017) in order to test whether slip and background seismicity are linked. The computation of the slip acceleration prior model and the results are shown later in the discussion (Section 6.4).

5 Analysis and inversion results

5.1 Velocity field and coupling

The spatial pattern of the horizontal inter-seismic surface displacements is given by the velocity terms v of the linear trajectory model (Equation (1) when imposing $a = 0$; see Section 3.3). Using the stable North America reference frame, we compare our velocity field (Figure 4, black arrows) to the one of Mavrommatis et al. (2014). We observe the same West-North-West direction of the velocity along the East coast of Honshu, as

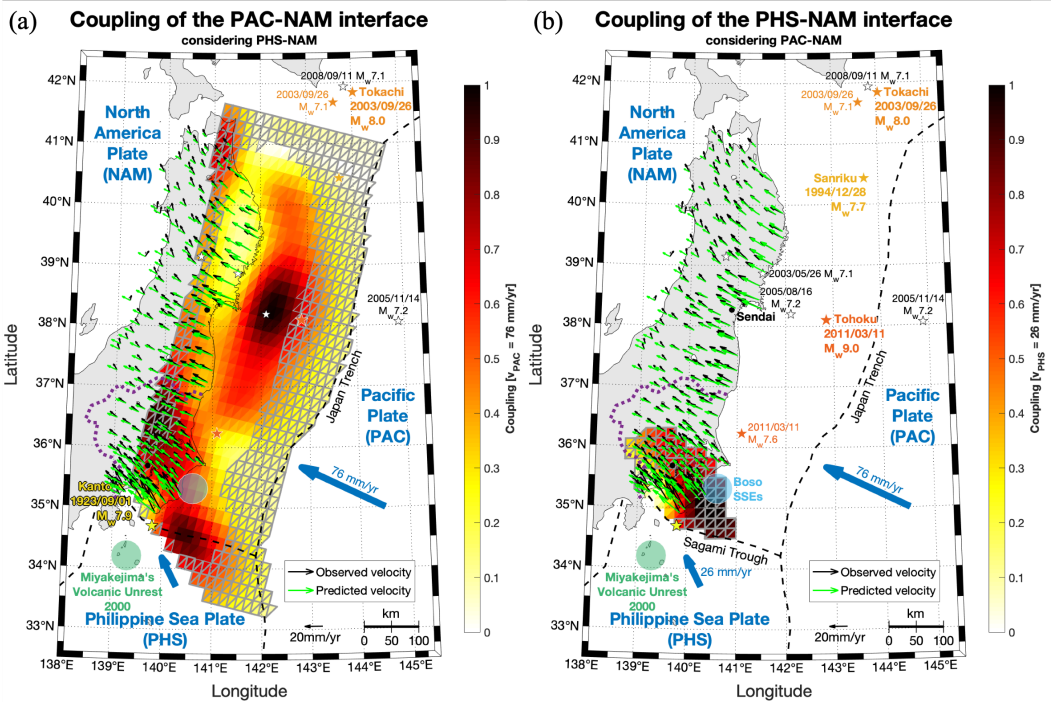

Figure 4. Inter-seismic coupling of the Pacific-North America (PAC-NAM) interface (a) and the Philippine Sea-North America (PHS) interface (b). Black arrows: observed velocity field, in a stable NAM reference frame. Green arrows: predicted velocity field. Gray grid: sub-faults for which the slip is poorly restored (see Section 4.4). The amount of coupling is shown with the color scale (from freely slipping in white to fully coupled in black). The convergence slip rates used to determine the coupling of each plate are $v_{PAC} = 76$ mm/yr for the PAC and $v_{PHS} = 26$ mm/yr for the PHS. Other elements are described in Figure 1.

well as a rotation towards the East when going North. The velocities have an amplitude of ∼17.5 mm/yr along the East coast and ∼9 mm/yr along the West coast of Honshu. The velocity field of Mavrommatis et al. (2014) is rotated by ∼5 mm/yr clockwise with respect to our field. This systematic difference is likely due to a different definition of the North America plate in both studies, although the effect of a different processing of the GPS time series cannot be excluded. This quantitative agreement between our inter-seismic velocity field and Mavrommatis et al. (2014) gives us confidence in the quality of our model for Honshu, hence also for the Kanto region.

We infer the inter-seismic coupling from the slip rates inverted according to Section 4. Figure 4 shows this coupling obtained when performing this inversion jointly on both the PAC-NAM and the PHS-NAM interfaces. On the PAC-NAM interface (Figure 4a), we see a strongly coupled area offshore Honshu from 38^o to 39^o N and from 141.7^o to 142.5^o E, as was already evidenced by Loveless and Meade (2010) and Perfettini and Avouac (2014). The PHS-NAM interface is also a strongly coupled along the Sagami Trough west of 141^o E. The wide coupled area and the coupling under Kanto was already observed by Loveless and Meade (2010), Nishimura et al. (2007), Noda et al. (2013) and Sagiya (2004). We also show in Supplementary Figures S8 and S9 the coupling obtained on PAC and PHS for smaller and larger σ_m values, hence allowing for a smoother or rougher coupling.

5.2 Acceleration field and slip acceleration

Our acceleration field (Figure 5, black and gray arrows) exhibits a landward acceleration North of Honshu with the amplitude decreasing when going East, and a trenchward acceleration South of 38.5^o N. The first order of our acceleration pattern and amplitude are compatible with the ones observed by Mavrommatis et al. (2014) and Yokota and Koketsu (2015). Nevertheless, a notable difference is found in the Kanto region, where Yokota and Koketsu (2015) show a very limited acceleration compared to the rest of Honshu. Instead, we find an eastward acceleration with an amplitude of the same order as the north Honshu acceleration. According to our statistical test of the acceleration significance (see Section 3.4) most acceleration values in the Kanto region are significant (Figure 5, black arrows). This acceleration suggests that some plate uncoupling took place between 1997 and 2011.

To resolve this, we first invert the slip acceleration field on the PAC-NAM subduction interface only. Figure 5 shows both accelerated (red) and decelerated (blue) slips. The slip acceleration corresponds to forward slip on the subduction interface, or equivalently a decrease in coupling. A remarkable result is the acceleration area South of 36.5^o N, consistent with the observed surface acceleration as mentioned earlier. This acceleration remains clearly visible even while varying the σ_m parameter (Supplementary Figure S10). Because the presence of the PHS plate cannot be ignored for the stations in Kanto, we perform a second inversion using both the PAC and PHS plates, cf. Supplementary Figure S11. Very limited changes are observed, with a decrease of the slip acceleration on the PAC plate limited to 0.6 mm/yr^2 at maximum, and an acceleration of the order of 0.3 mm/yr^2 on the PHS plate. Since there exists a trade-off between slip accelerations on either plates (see Section 4.5), we cannot resolve with accuracy the proportion of acceleration hosted by each plate. Our analysis however clearly demonstrates that there exists a significant increase in slip rate between 1997 and 2011 South of 36.5^o N, that is compatible with previous observations of acceleration in seismicity (Reverso et al., 2016) and SSE shortening in recurrence intervals (Fukuda, 2018; Hirose et al., 2012; Ozawa, 2014).

The residuals between the observed and modeled surface acceleration (Supplementary Figure S12) shows little spatial coherence at the large scale, implying that the model does well in capturing the large scale pattern, even though the residuals are almost always significantly larger than the uncertainties as discussed in Section 4.3.

The vertical component of the GPS time series being more noisy than the horizontal component, we did not use it in the models presented in the main text. We however evaluate the impact of adding the vertical displacements to the horizontal ones when inverting for the slip acceleration. We first notice that, indeed, the vertical accelerations do not exhibit a spatially coherent pattern, likely because of the noise (that includes all non-tectonic phenomena) contaminating the acceleration signal (Supplementary Figure S13b). Moreover, the inverted slip acceleration is in effect very little affected by the vertical acceleration, as shown in Supplementary Figure S13a.

6 Refined analyses and sensitivity tests

We here provide further analyses to (1) compare our results with those of Mavrommatis et al. (2014) and Yokota and Koketsu (2015), in particular the processing of the GPS data (Section 6.1) as well as the inclusion of slow deformation transients (Section 6.2); (2) assess how the slip acceleration translates in terms of progressive coupling / uncoupling (Section 6.3); (3) address how our results can be compared to changes in seismicity rates, by defining a "seismic-based" prior to the slip acceleration model (Section 6.4).

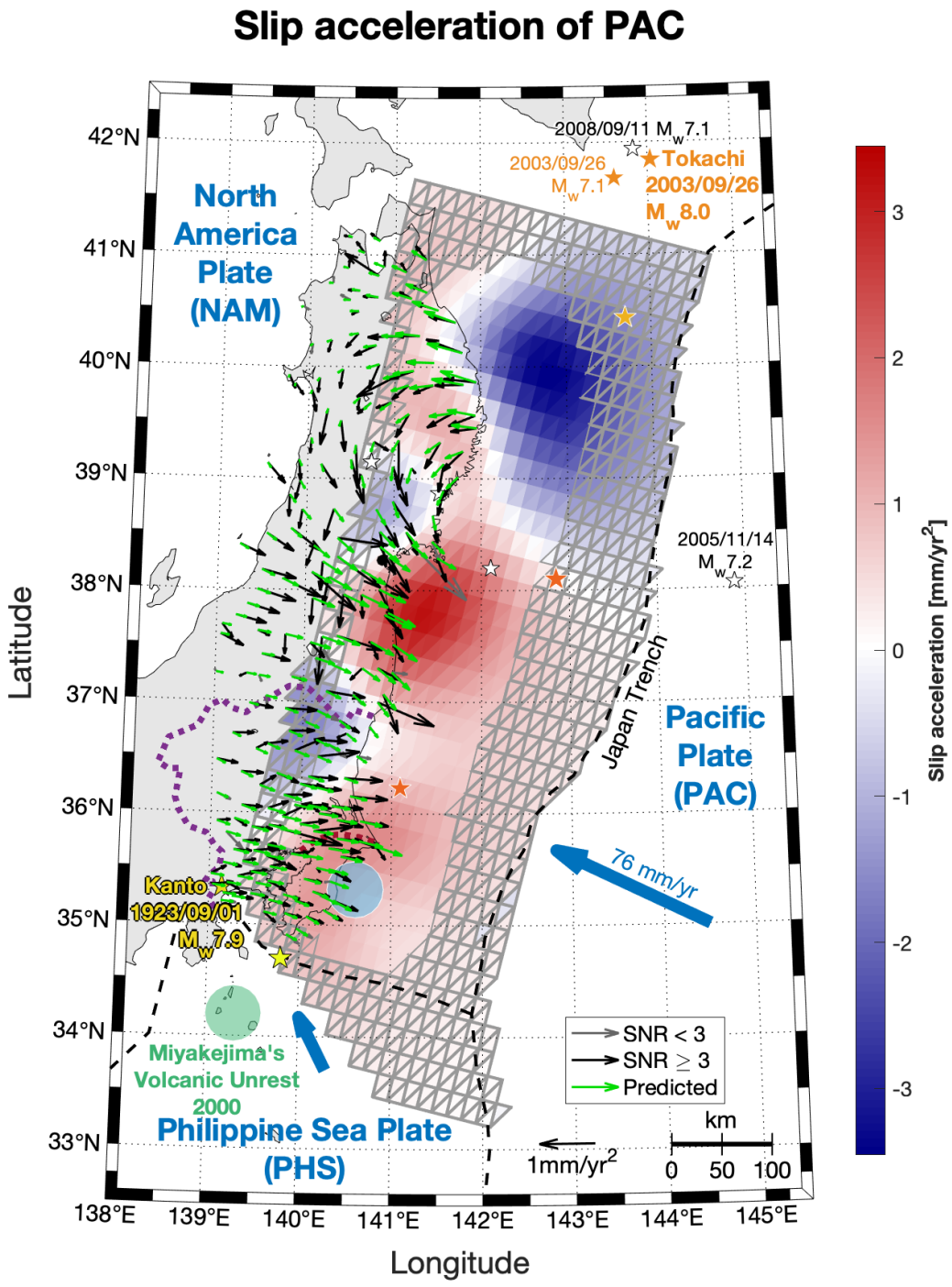

Figure 5. Slip acceleration of the Pacific (PAC) plate. The black and grey arrows depict the observed acceleration field: we distinguish the stations which have a signal-to-noise ratio greater than 3 (black), and those which fail to meet this criterion (grey, see Section 3.4). The green arrows represent the acceleration field predicted by the model. The amount of slip acceleration on the PAC slip interface is shown with the blue to red color-scale. The gray grid shows the sub-faults for which the slip is poorly restored (see Section 4.4).

6.1 This study with GAMIT/GLOBK processing versus F3 solution

A significant difference with the data presented in Mavrommatis et al. (2014) and Yokota and Koketsu (2015) is the GPS data processing approach, and the choice of a reference frame (International Terrestrial Reference Frame, ITRF version). We have here made use of the GAMIT/GLOBK software to derive daily positions that we combine and map into ITRF2014 (Altamimi et al., 2017) using PYACS (see Section 3.1). Both Mavrommatis et al. (2014) and Yokota and Koketsu (2015) instead used the GEONET F3 solution published by the Geospatial Information Authority of Japan. The F3 solution (Nakagawa et al., 2009) was processed with Bernese software (Walser et al., 2015) and mapped into the ITRF2005 reference frame (Altamimi et al., 2007). Tsuji et al. (2017) explain that the analysis for the F3 solution use the mapping function of Niell (1996), an estimated delay gradient and an absolute phase center and variations model.

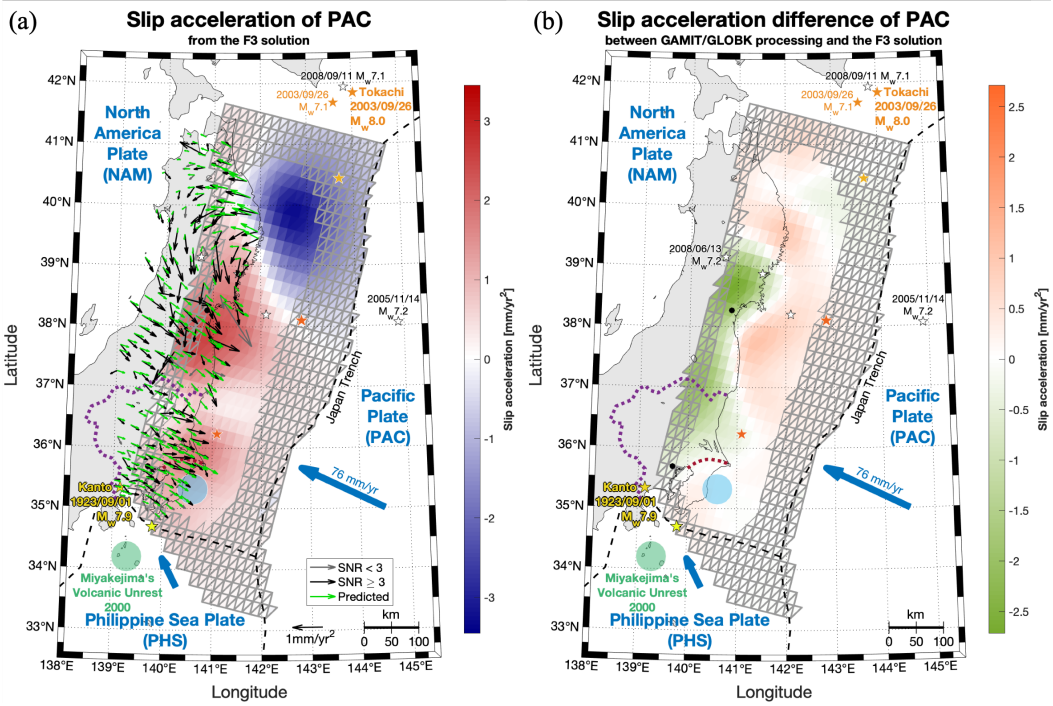

Figure 6. Slip acceleration of the Pacific (PAC) plate from the F3 solution. (a): Slip acceleration from the F3 solution; same legend than Figure 5. (b) Slip acceleration difference between the slip acceleration from GAMIT/GLOBK processing (Figure 5) and the slip acceleration from the F3 solution (a).

In order to compare our solution with the F3 solution we use the Helmert parameters given by the ITRF website (http://itrf.ensg.ign.fr) to rotate the F3 solution into the ITRF2014 (more details in Supplementary Text S1 and Supplementary Table S1). Then, we apply the analysis described in Section 3 to the converted F3 solution, by again fitting the trajectory model of Equation (1), and then inverting the acceleration field on the PAC plate (Section 4). The obtained acceleration field, shown in Figure 6, displays the same eastward acceleration North of Honshu and westward South of 39^o N as in Figure 5, in Mavrommatis et al. (2014) and in Yokota and Koketsu (2015). The F3 solution implies higher acceleration amplitudes (∼0.5 mm/yr) on the Eastern side of the island than our solution (∼0.1 mm/yr). Looking more specifically at Kanto, we observe significant acceleration with the F3 solution and GAMIT/GLOBK processing (black ar-

row, Figures 5 and 6) that were not reported by Mavrommatis et al. (2014) nor by Yokota and Koketsu (2015).

6.2 Influence of Boso slow slip events

Contrary to Mavrommatis et al. (2017) and Yokota and Koketsu (2015), we here consider the Boso SSEs in the time series modelling (see Sections 3.2 and 3.3), i.e., we correct for the deformation transients caused by the SSEs. To evaluate the impact of removing these SSEs, we additionally compute the inter-seismic velocities and the associated coupling without performing this correction (Supplementary Figure S14a). As naturally expected, for the PAC plate, the Boso SSE area is where the changes between both models are (Supplementary Figure S14b). The area that is most affected is however larger than the Boso SSEs slip area due to the inversion smoothing. For the PHS plate, the coupling is on average decreased by about 0.05 to 0.1, since we let the slow slip events contribute to the release of some of the accumulated slip (Supplementary Figure S15).

More importantly, we find that the inclusion or not of the Boso SSEs has a limited impact on the inverted slip acceleration on the PAC plate in the wider Kanto region (Supplementary Figure S16). Our results are therefore not very dependent on the actual modelling (or not) of the SSEs.

6.3 Coupling change compared to slip acceleration

The accelerated slip on the subduction interface corresponds to a change in coupling that can be simply evaluated. To do so, we estimate the coupling both in 1997 and 2011 using the displacement rates modeled at all stations at the dates 01/01/1997 and 06/02/2011. Namely, we extract the modeled velocity at the first date, which is by definition the linear term of the quadratic model (Equation (1)), and compute the associated coupling (Supplementary Figure S17a). Adding the acceleration term, we then compute the mean velocity at the second date and the associated coupling (Supplementary Figure S17b), and finally obtain the difference in coupling ΔC (Figure 7).

In Section 4.3, we mentioned that a coupling change of $\Delta C = 0.64$ over 14 years is equivalent to a mean slip acceleration $a_{slip} = 3.45$ mm/yr^2, given the PAC-NAM convergence rate. In fact, Figures 5 and 7 display similar relative variations, up to a simple proportionality factor imposed by the convergence rate ($v_{PAC} = 76$ mm/yr) and the duration of observation ($\Delta t = 14.1$ yr):

$$a_{slip} = \Delta C \, \frac{v_{PAC}}{\Delta t} \tag{14}$$

We find that the coupling changes can be large, with an average of -0.2 to -0.3 South of 36.5^o N (Figure 7).

6.4 Seismic acceleration and slip acceleration

We compare our results and complement them with the acceleration of background seismicity obtained by Marsan et al. (2017), who studied how the rate of background earthquakes changed along the Japan Trench from 1990 to 2011. They declustered the earthquake activity taking place within 20 km of the PAC slip interface, modeled the time evolution of the obtained background rate with a parabolic polynomial $\widehat{\mu}(t)$, and computed a background rate change coefficient ϕ defined as the modeled rate just before the 09/03/2011 M 7.3 foreshock of the Tohoku mainshock divided by the modeled rate on the 01/01/1990:

$$\phi = \frac{\widehat{\mu}(t = 09/03/2011)}{\widehat{\mu}(t = 01/01/1990)} \tag{15}$$

Using the same data and methodology, we compute the seismic acceleration ϕ but only from 01/01/1997 to 06/02/2011 (Figure 8a) to be consistent with the time interval used

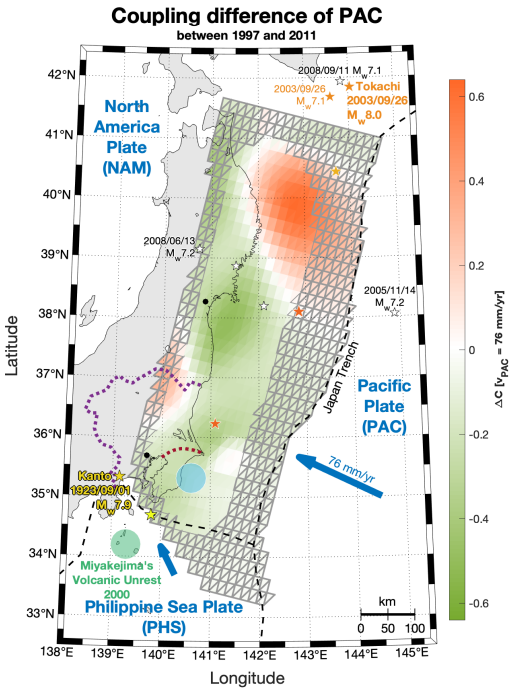

Figure 7. Coupling difference ΔC of the Pacific (PAC) plate between 1997 and 2011. The amount of ΔC on the PAC is shown with the green-orange color-scale: orange sub-faults are more coupled in 2011 (and green in 1997). The gray grid shows the sub-faults where the slip is poorly restored (see Section 4.4). Other elements are described in Figure 1.

in the GPS analysis. We then convert this seismic acceleration ϕ into the expected slip acceleration over the same period, defining a new prior model as shown in Figure 8c. This conversion is based on the assumption that the slip rate (dx_{slip}/dt) and the background seismicity rate ($\widehat{\mu}$) are proportional (the proportionality coefficient is assumed constant in time, but is allowed to vary spatially). In our modeling, the modeled slip rate is $dx_{slip}/dt = v_{slip} + a_{slip}\,(t - t_R)$; we thus have for any initial t_1 and ending t_2 dates:

$$\phi = \frac{v_{slip} + a_{slip}\,(t_2 - t_R)}{v_{slip} + a_{slip}\,(t_1 - t_R)} \tag{16}$$

We here use $t_1 = 1997$ so that $t_1 = t_R$ (same reference time than for Equation (1)), and $t_2 = 2011.1$. We thus get that the slip acceleration when comparing slip rates at those t_1 and t_2 is:

$$a_{slip} = (\phi - 1)\frac{v_{slip}}{t_2 - t_R} \tag{17}$$

with $v_{slip} = (1 - C)v_{PAC}$ where C is the coupling coefficient and $v_{PAC} = 76$ mm/yr. As we only examine changes over time, this approach allows to discard the unknown proportionality coefficient between the slip and seismicity rates.

Marsan et al. (2017) made use of two distinct declustering methods, so to only keep acceleration patterns that remain robust with regard to the specific assumptions underlying each of these methods. As a result, locations with incoherent acceleration values obtained with these two methods were discarded from the analysis (explaining the apparent lacunarity of Figure 8a). This is notably the case for a ∼150 km-long portion of the trench centered on the Tohoku mainshock (between about 36.5^o and 38^o N) and downdip of it where the two methods give opposite results when declustering the 2003 intra-slab and 2005 Miyagi earthquake aftershock sequences. In our present slip rate inversion from

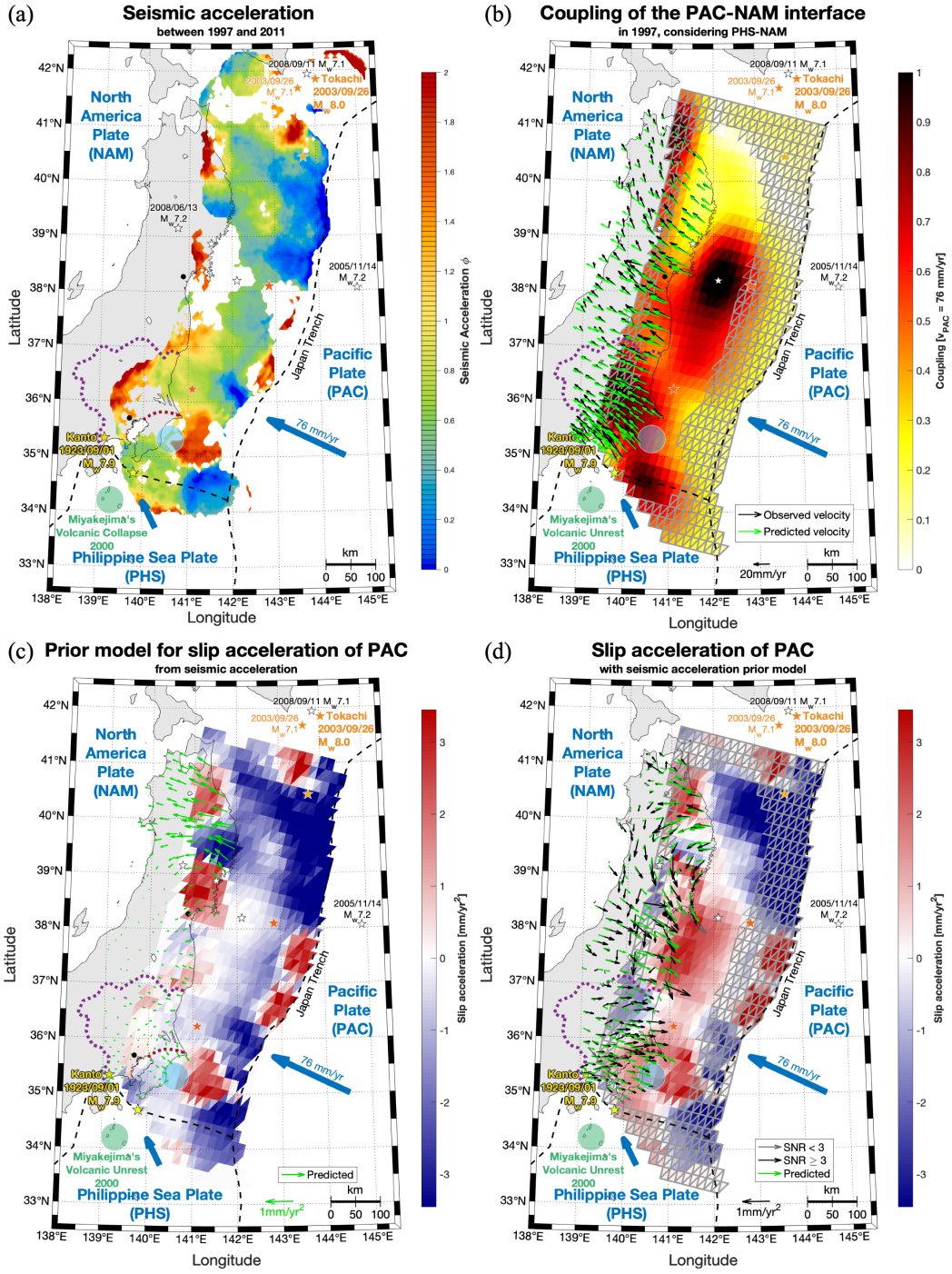

Figure 8. Seismic acceleration of the Pacific (PAC) plate between 1997 and 2011 as slip acceleration prior. (a): Seismic acceleration of the Pacific (PAC) plate between 1997 and 2011, based on Marsan et al. (2017); the color-scale gives the acceleration value ϕ of the seismicity rate: blue ($\phi < 1$) represents deceleration and red ($\phi > 1$) acceleration. Other elements are described in Figure 1. (b) Coupling of the Pacific-North America (PAC-NAM) interface; same legend as Figure 4. (c): Prior slip acceleration model of the PAC plate based on the seismic acceleration (a) and the coupling (b) with Equation (17); same legend as Figure 5. (d): Slip acceleration of the PAC plate; same legend as Figure 5.

GPS observations, we cannot leave sub-faults with no a priori value at all, and therefore, by default, we interpolate the ϕ value on those sub-faults, by considering the sub-faults within a 30 km radius and taking a weighted (according to distance) average of the corresponding seismic accelerations. This interpolation yields a mild deceleration ϕ value for most of this zone.

The slip rate prior obtained using the seismicity is shown in Figure 8c, and show good correlation with the already inverted slip rate of Figure 5, albeit (1) with no acceleration downdip of the 36.5^o-38^o N portion of the trench, due to the disagreement between the two declustering methods there as already commented, and (2) with a stronger signal updip along the trench, in areas where the GPS inversion has no resolution. We show the inverted slip acceleration field using this prior in Figure 8d. The coupling used in Figure 8b is obtained with a fully uncoupled prior model; Supplementary Figure S18 shows the results using the coupling as given by a fully coupled prior model. Apart from the improved resolution along the trench (cf. item (2) above), the most notable difference with Figure 5 is South and East of the Boso SSEs area: even if we have a good restitution there, the slip acceleration is partly controlled by the prior model, so that we do not observe acceleration nor deceleration with a null prior model, while with the prior model based on seismicity we obtain acceleration (East) and deceleration (South) consistent with the strong changes in seismicity observed there (Figure 8d and Supplementart Figure S18d).

7 Discussion

Our analysis completes previous similar studies (Heki & Mitsui, 2013; Loveless & Meade, 2010; Mavrommatis et al., 2014; Yokota & Koketsu, 2015) in several ways: (1) by testing different methods for computing the daily GPS solution ; (2) by accounting for SSEs in Boso as well as the 2000 Miyakejima volcanic unrest : these transients were removed from the GPS time series (Section 3.3), even though this is found to have little consequences on the estimated slip acceleration, cf. Section 6.2; (3) by including the PHS slip interface underneath Kanto and along the Sagami Trough (as shown in Figure 4b). The addition of the PHS plate does not significantly modify the results obtained with the PAC plate alone, see Section 5.2 and Supplementary Figure S11; (4) by adding prior information based on background seismicity changes (Section 6.4). From this, we confirm and strengthen the robustness of previous observations, mainly relating to a significant acceleration of the slip for the PAC subduction, in the range of 1.5 to 2.5 mm/yr^2 centered at 37^o to 38^o N, and corresponding to the downdip extension of the area that slipped by more than 30 m during the 2011 M_w 9.0 Tohoku earthquake. Such a slip acceleration corresponds to a decrease in coupling of the order of -0.3 to -0.4 over the 1997-2011 period (Figure 7). This area is well delineated by a marked reversal in sign of the acceleration to the north: all tested models (Figures 5 to 8) find a robust slip deceleration of $\sim$3 mm/yr^2 north of 39^o N, which origin could be related to the 1994 Sanriku earthquake and subsequent afterslip (Heki et al., 1997) and/or to the 2003 Tokachi earthquake (Heki & Mitsui, 2013). This contrasts with a milder transition more to the south (at about 36.5^o N), South of which another patch of slip acceleration is found which amplitude depends on the model (Figures 5 to 8). It has been argued by Hasegawa and Yoshida (2015) that the downdip acceleration (between 37^o and 38^o N) must have contributed to further stressing of the main asperity that eventually failed in 2011. Whether this acceleration is a common phenomenon in this region or not cannot be answered with certainty. Hardebeck (2012) discusses the near complete release of the differential stress at the time of the 2011 shock, along with the fact that the released seismic moment only amounts to a 0.23-0.77 of the moment that accumulated in the 1142 years since the last equivalent megathrust earthquake in this region, the 869 AD Jogan earthquake that triggered a tsunami with comparable characteristics to those of the 2011 Tohoku event (e.g. Minoura et al., 2001, 2013; Sugawara et al., 2012). Indeed, even accounting for large post-

seismic relaxation lasting several decades (as seen after the 1960 Chile earthquake) (e.g. Melnick et al., 2018; Wang et al., 2007) and incomplete plate coupling, a M_w 9 earthquake would need to occur every 300-700 years to match the average modeled rate of moment accumulation (Ozawa et al., 2002). The stressing rate (hence slip rate) is thus likely to vary during the extended inter-seismic period. The short-term (i.e., over 14 years) average coupling could then be an over-estimation of the longer time-averaged coupling. The fact that we observe a 14 year-long decrease of coupling (even after removing co- and post-seismic effects of the intermediate size earthquakes that have occurred in the region during this time period) therefore is coherent with the fact that there must exist significant variations of coupling during the earthquake cycle in this region.

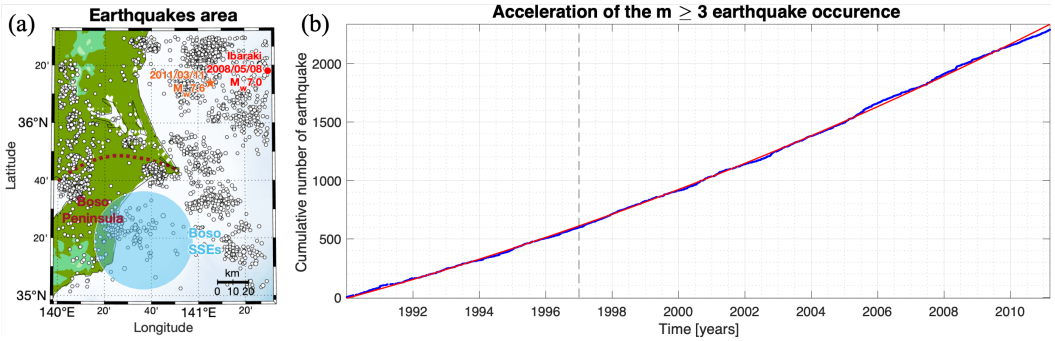

Figure 9. Acceleration of $m \geq 3$ earthquakes within 10 km of the Pacific-North America (PAC-NAM) interface (b) in the 35^o-36.5^o N, 140^o-141.5^o E box (a), for the 1990-March 2011 period. (a): White circles: $m \geq 3$ earthquakes within 10 km of the PAC-NAM interface; red circle: 2008 M_w 7.0 Ibaraki earthquake; other elements are described in Figure 1. (b): Blue dots: cumulative number of $m \geq 3$ earthquakes; red line: quadratic model. The quadratic fit is shown in red, and gives an acceleration in seismicity rate of +86% for 1990-2011 and +44% for 1997-2011 (the vertical dashed line shows the 01/01/1997 date).

Our analysis finds a broad slip acceleration in the 35^o to 36^o N area, although weaker (by a factor 2) than for the 37^o-38^o N region. This was not identified by previous studies, although this is a robust feature of our inversions (Figures 5 to 8). Even though some trade-off exists between accelerated slip along the PAC-NAM and the PHS-NAM interfaces, our analysis suggests the slip acceleration along the former dominates (Figure 5 and Supplementary Figure S11); we however cannot reject the possibility that some of this acceleration took place along the PHS-NAM interface. Compared to the rest of our studied area, this zone is characterized by small earthquakes, with the noticeable exception of the 2008 M_w 7.0 Ibaraki earthquake. Because of this, the seismicity dynamics is relatively smooth, and is not dominated by strong aftershock sequences, as is on the contrary observed more to the north (Ozawa et al., 2012). A direct analysis of the seismicity ($m \geq 3$) rate can thus be conducted without having to correct for aftershock sequences. Figure 9 confirms the existence of a significant acceleration of the earthquake rate in the region from 35^o to 36.5^o N, 140^o to 141.5^o E, that cannot be attributed to the 2008 Ibaraki mainshock and its aftershock sequence (especially as it occurs relatively late in the considered 1997-2011 interval). We further notice that this area hosts SSEs (offshore Boso), as well as seismicity swarms that could be the signature of small SSEs outside the Boso area that have so far escaped detection through GPS measurements (Gardonio et al., 2018; Reverso et al., 2016). The accelerated seismicity would thus be directly related to an acceleration of the controlling aseismic forcing rate at these specific locations. This is coherent with (1) the strong acceleration in background rate observed by Marsan et al. (2017) over the 1990-2011 period, (2) the remarkable acceleration in seismicity rate

in the Boso area for the same period (Reverso et al., 2016), as well as (3) the shortening of Boso inter-SSE periods of times (Ozawa, 2014). In the last two cases, slip acceleration on the PHS-NAM interface is likely to be the main cause. All these observations point to a decoupling of the PAC and PHS interfaces there, estimated to about 0.2 to 0.3 for PAC as shown in Figure 7. This area did not rupture during the 2011 mega-thrust earthquake, perhaps because the coupling at shallow depths along the Japan Trench is too low there, so that the rupture could not break new strong asperities that would have extended it further south.

Conclusions

To obtain new insights into the changes in surface displacement seen in Northern Japan (Honshu), we performed a different GPS processing than the F3 solution as used by Mavrommatis et al. (2014) and Yokota and Koketsu (2015), and developed our own analysis. We processed the data using the GAMIT/GLOBK suite based on double difference positioning and modeled the resulting time series with a trajectory model that accounts for slow deformation events as well as co- and post-seismic effects of intermediate to large earthquakes. We then inverted the slip rate distribution on the modeled PAC plate. As observed by previous analyses, the main feature north of 37^o N is a fault slip acceleration, corresponding to a decoupling, downdip the Tohoku rupture, that could be related to the 2011 megathrust rupture - i.e., that at least could have hastened it.

Our main finding is that a distinct zone of slip acceleration is located South of 36.5^o N (Figure 5). Fukuda (2018), Hirose et al. (2012) and Ozawa (2014) have suggested that a shortening of the recurrence interval of the SSE offshore Boso Peninsula has taken place starting in the decade before the 2011 mainshock. Here we show that, more generally, a large extent of the PAC subduction slip interface (i.e., larger than the typical size of the Boso SSE on the PHS) has been accelerating steadily since 1997. This acceleration is robust, and remains present in all the various sensitivity tests carried out (namely: comparing the inter-seismic and inter-SSE solutions, using the F3 solution, changing the post-seismic relaxation time, using the seismic acceleration as prior model). We moreover checked how this result could be influenced by the inclusion of the PHS plate in the inversion, in addition to PAC. Adding PHS does not negate the wide acceleration on PAC south of 36.5^o N, and could even contribute (up to $\sim$0.3 mm/year^2) to it, in coherence with the reduced waiting times between Boso SSEs. This observation of an accelerated slip rate noticeably far from the 2011 rupture remains to be explained. It adds up to previous observations in other plate convergence contexts (Materna et al., 2019; Meltzner et al., 2015; Prawirodirdjo et al., 2010) that the slip rate, and thus the plate coupling, could evolve significantly over years to decades outside the widely observed post-seismic slip following any mainshock.

Acknowledgments

We would like to thank Michel Bouchon, Mohamed Chlieh and Piero Poli for very valuable discussions and suggestions. This work has been supported by the Agence Nationale de la Recherche (ANR-17-CE31-0002-01) AtypicSSE project and by Université Savoie Mont-Blanc. We are very grateful to the Geospatial Information Authority of Japan (GSI) for making the GEONET GNSS data available. Most of the computations presented in this paper were performed using the GRICAD infrastructure (https://gricad.univ-grenoble-alpes.fr), which is partly supported by the Equip@Meso project (reference ANR-10-EQPX-29-01) of the programme Investissements d'Avenir supervised by the Agence Nationale pour la Recherche, and the CIMENT infrastructure (https://ciment.ujf-grenoble.fr), which is supported by the Rhône-Alpes region (grant CPER07_13 CIRA : http ://www.ci-ra.org) and France-Grille (http://www.france-grilles.fr). Time series data will be accessible on the Observatoire des Sciences due l'Univers de Grenoble website (https://doi.osug.fr/data/public/GNSS_products/

References

Akaike, H., Parzen, E., Tanabe, K., & Kitagawa, G. (1998). *Selected papers of Hirotugu Akaike*. New York, NY: Springer. doi: https://doi.org/10.1007/978-1-4612-1694-0

Altamimi, Z., Collilieux, X., Legrand, J., Garayt, B., & Boucher, C. (2007). ITRF2005: A new release of the International Terrestrial Reference Frame based on time series of station positions and Earth Orientation Parameters. *Journal of Geophysical Research*, *112*(B09401). doi: https://doi.org/10.1029/2007JB004949

Altamimi, Z., Métivier, L., Rebischung, P., Rouby, H., & Collilieux, X. (2017). ITRF2014 plate motion model. *Geophysical Journal International*, *209*(3), 1906–1912. doi: https://doi.org/10.1093/gji/ggx136

Bevis, M., & Brown, A. (2014). Trajectory models and reference frames for crustal motion geodesy. *Journal of Geodesy*, *88*(3), 283–311. doi: https://doi.org/10.1007/s00190-013-0685-5

Boehm, J., Werl, B., & Schuh, H. (2006). Troposphere mapping functions for GPS and very long baseline interferometry from European Centre for Medium-Range Weather Forecasts operational analysis data. *Journal of Geophysical Research: Solid Earth*, *111*(B2). doi: https://doi.org/10.1029/2005JB003629

Cattania, C., Rivalta, E., Hainzl, S., Passarelli, L., & Aoki, Y. (2017). A nonplanar slow rupture episode during the 2000 Miyakejima dike intrusion. *Journal of Geophysical Research: Solid Earth*, *122*, 2054—2068. doi: https://doi.org/10.1002/2016JB013722

Foy, T. A., Frankel, K. L., Lifton, Z. M., Johnson, C. W., & Caffee, M. W. (2012). Distributed extensional deformation in a zone of right-lateral shear: Implications for geodetic versus geologic rates of deformation in the eastern California shear zone-Walker Lane. *Tectonics*, *31*(TC4008). doi: https://doi.org/10.1029/2011TC002930

Fukuda, J. (2018). Variability of the space-time evolution of slow slip events off the Boso Peninsula, central Japan, from 1996 to 2014. *Journal of Geophysical Research: Solid Earth*, *123*, 732–760. doi: https://doi.org/10.1002/2017JB014709

Ganev, P. N., Dolan, J. F., McGill, S. F., & Frankel, K. L. (2012). Constancy of geologic slip rate along the central Garlock fault: implications for strain accumulation and release in southern California. *Geophysical Journal International*, *190*(2), 745–760. doi: https://doi.org/10.1111/j.1365-246X.2012.05494.x

Gardonio, B., Marsan, D., Bouchon, M., Socquet, A., Jara, J., Sun, Q., ... Campillo, M. (2018). Revisiting slow slip events occurrence in Boso Peninsula, Japan, combining GPS data and repeating earthquakes analysis. *Journal of Geophysical Research: Solid Earth*, *123*, 1502–1515. doi: https://doi.org/10.1002/2017JB014469

Hardebeck, J. L. (2012). Coseismic and postseismic stress rotations due to great subduction zone earthquakes. *Geophysical Research Letters*, *39*(L21313). doi: https://doi.org/10.1029/2012GL053438

Hasegawa, A., & Yoshida, K. (2015). Preceding seismic activity and slow slip events in the source area of the 2011 Mw 9.0 Tohoku-Oki earthquake: a review. *Geoscience Letters*, *2*(6). doi: https://doi.org/10.1186/s40562-015-0025-0

Hayes, G. P., Moore, G. L., Portner, D. E., Hearne, M., Flamme, H., Furtney, M., & Smoczyk, G. M. (2018). Slab2, a comprehensive subduction zone geometry model. *Science*, *362*(6410), 58–61. doi: https://doi.org/10.1126/science.aat4723

Heki, K., & Mitsui, Y. (2013). Accelerated pacific plate subduction following interplate thrust earthquakes at the Japan trench. *Earth and Planetary Science Letters*, *363*, 44–49. doi: https://doi.org/10.1016/j.epsl.2012.12.031

Heki, K., Miyazaki, S., & Tsuji, H. (1997). Silent fault slip following an interplate

thrust earthquake at the Japan trench. *Nature*, *386*(6625), 595–598. doi: https://doi.org/10.1038/386595a0

Herring, T. A., Floyd, M. A., King, R. W., & McClusky, S. C. (2015). GLOBK reference manual : Global Kalman filter VLBI and GPS analysis program : Release 10.6 [Computer software manual].

Herring, T. A., King, R. W., Floyd, M. A., & McClusky, S. C. (2018a). GAMIT reference manual : GPS analysis at MIT : Release 10.7 [Computer software manual].

Herring, T. A., King, R. W., Floyd, M. A., & McClusky, S. C. (2018b). Introduction to GAMIT/GLOBK : Release 10.7 [Computer software manual].

Herring, T. A., Melbourne, T. I., Murray, M. H., Floyd, M. A., Szeliga, W. M., King, R. W., ... Wang, L. (2016). Plate Boundary Observatory and related networks: GPS data analysis methods and geodetic products. *Reviews of Geophysics*, *54*, 759–808. doi: https://doi.org/10.1002/2016RG000529

Hirose, H., Hirahara, K., Kimata, F., Fujii, N., & Miyazaki, S. (1999). A slow thrust slip event following the two 1996 Hyuganada earthquakes beneath the Bungo Channel, southwest Japan. *Geophysical Research Letters*, *26*(21), 3237–3240. doi: https://doi.org/10.1029/1999GL010999

Hirose, H., Kimura, H., Enescu, B., & Aoi, S. (2012). Recurrent slow slip event likely hastened by the 2011 Tohoku earthquake. *Proceedings of the National Academy of Sciences*, *109*(38), 15157–15161. doi: https://doi.org/10.1073/pnas.1202709109

Hooper, A., Pietrzak, J., Simons, W., Cui, H., Riva, R., Naeije, M., ... Socquet, A. (2013). Importance of horizontal seafloor motion on tsunami height for the 2011 Mw=9.0 Tohoku-Oki earthquake. *Earth and Planetary Science Letters*, *361*, 469–479. doi: https://doi.org/10.1016/j.epsl.2012.11.013

Ishida, M. (1992). Geometry and relative motion of the Philippine Sea plate and Pacific plate beneath the Kanto-Tokai district, Japan. *Journal of Geophysical Research*, *97*(B1), 489–513. doi: https://doi.org/10.1029/91JB02567

Ito, A. (2004). Fault plane geometry in the source region of the 1994 Sanriku-oki earthquake. *Earth and Planetary Science Letters*, *223*, 163–175. doi: https://doi.org/10.1016/j.epsl.2004.04.007

Ito, T., & Yoshioka, S. (2002). A dike intrusion model in and around Miyakejima, Niijima and Kozushima in 2000. *Tectonophysics*, *359*, 171–187. doi: https://doi.org/10.1016/S0040-1951(02)00510-3

Jara, J., Socquet, A., Marsan, D., & Bouchon, M. (2017). Long-term interactions between intermediate depth and shallow seismicity in North Chile subduction zone. *Geophysical Research Letters*, *44*, 9283–9292. doi: https://doi.org/10.1002/2017GL075029

Kobayashi, A. (2014). A long-term slow slip event from 1996 to 1997 in the Kii Channel, Japan. *Earth, Planets and Space*, *66*(9). doi: https://doi.org/10.1186/1880-5981-66-9

Kobayashi, A., & Tsuyuki, T. (2019). Long-term slow slip event detected beneath the Shima Peninsula, central Japan, from GNSS data. *Earth, Planets and Space*, *71*(60). doi: https://doi.org/10.1186/s40623-019-1037-3

Komori, J., Shishikura, M., Ando, R., Yokoyama, Y., & Miyairi, Y. (2017). History of the great Kanto earthquakes inferred from the ages of Holocene marine terraces revealed by a comprehensive drilling survey. *Earth and Planetary Science Letters*, *471*, 74–84. doi: https://doi.org/10.1016/j.epsl.2017.04.044

Kositsky, A. P., & Avouac, J.-P. (2010). Inverting geodetic time series with a principal component analysis-based inversion method. *Journal of Geophysical Research*, *115*(B03401). doi: https://doi.org/10.1029/2009JB006535

Li, S., Freymueller, J., & McCaffrey, R. (2016). Slow slip events and time-dependent variations in locking beneath Lower Cook Inlet of the Alaska-Aleutian subduction zone. *Journal of Geophysical Research: Solid Earth*, *121*, 1060–1079. doi:

https://doi.org/10.1002/2015JB012491

Loveless, J. P., & Meade, B. J. (2010). Geodetic imaging of plate motions, slip rates, and partitioning of deformation in Japan. *Journal of Geophysical Research*, *115*(B02410). doi: https://doi.org/10.1029/2008JB006248

Loveless, J. P., & Meade, B. J. (2016). Two decades of spatiotemporal variations in subduction zone coupling offshore Japan. *Earth and Planetary Science Letters*, *436*, 19–30. doi: https://doi.org/10.1016/j.epsl.2015.12.033

Marsan, D., Bouchon, M., Gardonio, B., Perfettini, H., Socquet, A., & Enescu, B. (2017). Change in seismicity along the Japan trench, 1990-2011, and its relationship with seismic coupling. *Journal of Geophysical Research: Solid Earth*, *122*. doi: https://doi.org/10.1002/2016JB013715

Materna, K., Bartlow, N., Wech, A., Williams, C., & Bürgmann, R. (2019). Dynamically triggered changes of plate interface coupling in Southern Cascadia. *Geophysical Research Letters*, *46*, 12,890–12,899. doi: https://doi.org/10.1029/2019GL084395

Mavrommatis, A. P., Segall, P., & Johnson, K. M. (2014). A decadal-scale deformation transient prior to the 2011 Mw 9.0 Tohoku-oki earthquake. *Geophysical Research Letters*, *41*, 4486–4494. doi: https://doi.org/10.1002/2014GL060139

Mavrommatis, A. P., Segall, P., & Johnson, K. M. (2017). A physical model for interseismic erosion of locked fault asperities. *Journal of Geophysical Research: Solid Earth*, *122*, 8326–8346. doi: https://doi.org/10.1002/2017JB014533

Mavrommatis, A. P., Segall, P., Uchida, N., & Johnson, K. M. (2015). Long-term acceleration of aseismic slip preceding the Mw 9 Tohoku-oki earthquake: Constraints from repeating earthquakes. *Geophysical Research Letters*, *42*. doi: https://doi.org/10.1002/2015GL066069

Melnick, D., Li, S., Moreno, M., Cisternas, M., Jara-Muñoz, J., Wesson, R., ... Deng, Z. (2018). Back to full interseismic plate locking decades after the giant 1960 Chile earthquake. *Nature Communications*, *9*(3527). doi: https://doi.org/10.1038/s41467-018-05989-6

Melnick, D., Moreno, M., Quinteros, J., Baez, J. C., Deng, Z., Li, S., & Oncken, O. (2017). The super-interseismic phase of the megathrust earthquake cycle in Chile. *Geophysical Research Letters*, *44*, 784–791. doi: https://doi.org/10.1002/2016GL071845

Meltzner, A. J., Sieh, K., Chiang, H.-W., Wu, C.-C., Tsang, L. L., Shen, C.-C., ... Briggs, R. W. (2015). Time-varying interseismic strain rates and similar seismic ruptures on the Nias–Simeulue patch of the Sunda megathrust. *Quaternary Science Reviews*, *122*, 258–281. doi: https://doi.org/10.1016/j.quascirev.2015.06.003

Minoura, K., Hirano, S.-i., & Yamada, T. (2013). Identification and possible recurrence of an oversized tsunami on the Pacific coast of northern Japan. *Natural Hazards*, *68*, 631–643. doi: https://doi.org/10.1007/s11069-013-0640-z

Minoura, K., Imamura, F., Sugawara, D., Kono, Y., & Iwashita, T. (2001). The 869 Jogan tsunami deposit and recurrence interval of large-scale tsunami on the Pacific coast of northeast Japan. *Journal of Natural Disaster Science*, *23*(2), 83–88.

Miyazaki, S., McGuire, J. J., & Segall, P. (2003). A transient subduction zone slip episode in southwest Japan observed by the nationwide GPS array. *Journal of Geophysical Research*, *108*(B2), 2087. doi: https://doi.org/10.1029/2001JB000456

Nakada, S., Nagai, M., Kaneko, T., Nozawa, A., & Suzuki-Kamata, K. (2005). Chronology and products of the 2000 eruption of Miyakejima Volcano, Japan. *Bulletin of Volcanology*, *67*, 205–218. doi: https://doi.org/10.1007/s00445-004-0404-4

Nakagawa, H., Toyofuku, T., Kotani, K., Miyahara, B., Iwashita, C., Kawamoto, S., ... Suguwara, Y. (2009). Development and validation of GEONET new

analysis strategy (Version 4) [in Japanese]. *Journal of the Geographical Survey Institute*, *118*, 1–8.

Newcomb, K. R., & McCann, W. R. (1987). Seismic hisoty and seismotectonics of the Sunda Arc. *Journal of Geophysical Research*, *92*(B1), 421–439.

Niell, A. E. (1996). Global mapping functions for the atmosphere delay at radio wavelengths. *Journal of Geophysical Research: Solid Earth*, *101*(B2), 3227–3246. doi: https://doi.org/10.1029/95JB03048

Nishimura, T., Sagiya, T., & Stein, R. S. (2007). Crustal block kinematics and seismic potential of the northernmost Philippine Sea plate and Izu microplate, central Japan, inferred from GPS and leveling data. *Journal of Geophysical Research*, *112*(B05414). doi: https://doi.org/10.1029/2005JB004102

Noda, A., Hashimoto, C., Fukahata, Y., & Matsu'ura, M. (2013). Interseismic GPS strain data inversion to estimate slip-deficit rates at plate interfaces: application to the Kanto region, central Japan. *Geophysical Journal International*, *193*, 61–77. doi: https://doi.org/10.1093/gji/ggs129

Ochi, T., & Kato, T. (2013). Depth extent of the long-term slow slip event in the Tokai district, central Japan: A new insight. *Journal of Geophysical Research: Solid Earth*, *118*, 4847–4860. doi: https://doi.org/10.1002/jgrb.50355

Okada, Y. (1985). Surface deformation due to shear and tensile faults in a half-space. *Bulletin of the Seismological Society of America*, *75*(4), 1135–1154. doi: https://doi.org/10.1016/0148-9062(86)90674-1

Oskin, M., Perg, L., Shelef, E., Strane, M., Gurney, E., Singer, B., & Zhang, X. (2008). Elevated shear zone loading rate during an earthquake cluster in eastern California. *Geology*, *36*(6), 507-510. doi: https://doi.org/10.1130/G24814A.1

Ozawa, S. (2014). Shortening of recurrence interval of Boso slow slip events in Japan. *Geophysical Research Letters*, *41*, 2762–2768. doi: https://doi.org/10.1002/2014GL060072

Ozawa, S., Murakami, M., Kaidzu, M., Tada, T., Sagiya, T., Hatanaka, Y., ... Nishimura, T. (2002). Detection and monitoring of ongoing aseismic slip in the Tokai region, central Japan. *Science*, *298*(5595), 1009–1012. doi: https://doi.org/10.1126/science.1076780

Ozawa, S., Murakami, M., & Tada, T. (2001). Time-dependent inversion study of the slow thrust event in the Nankai trough subduction zone, southwestern Japan. *Journal of Geophysical Research: Solid Earth*, *106*(B1), 787–802. doi: https://doi.org/10.1029/2000JB900317

Ozawa, S., Nishimura, T., Munekane, H., Suito, H., Kobayashi, T., Tobita, M., & Imakiire, T. (2012). Preceding, coseismic, and postseismic slips of the 2011 Tohoku earthquake, Japan. *Journal of Geophysical Research*, *117*(B07404). doi: https://doi.org/10.1029/2011JB009120

Ozawa, S., Suito, H., Imakiire, T., & Murakmi, M. (2007). Spatiotemporal evolution of aseismic interplate slip between 1996 and 1998 and between 2002 and 2004, in Bungo channel, southwest Japan. *Journal of Geophysical Research*, *112*(B05409). doi: https://doi.org/10.1029/2006JB004643

Ozawa, S., Suito, H., & Tobita, M. (2007). Occurrence of quasi-periodic slow-slip off the east coast of the Boso peninsula, Central Japan. *Earth, Planets and Space*, *59*, 1241–1245. doi: https://doi.org/10.1186/BF03352072

Ozawa, S., Yarai, H., Imakiire, T., & Tobita, M. (2013). Spatial and temporal evolution of the long-term slow slip in the Bungo Channel, Japan. *Earth, Planets and Space*, *65*, 67–73. doi: https://doi.org/10.5047/eps.2012.06.009

Perfettini, H., & Avouac, J. (2014). The seismic cycle in the area of the 2011 Mw9.0 Tohoku-Oki earthquake. *Journal of Geophysical Research: Solid Earth*, *119*, 4469–4515. doi: https://doi.org/10.1002/2013JB010697

Prawirodirdjo, L., McCaffrey, R., Chadwell, C. D., Bock, Y., & Subarya, C. (2010). Geodetic observations of an earthquake cycle at the Sumatra subduction zone:

Role of interseismic strain segmentation. *Journal of Geophysical Research*, *115*(B03414). doi: https://doi.org/10.1029/2008JB006139

Radiguet, M., Cotton, F., Vergnolle, M., Campillo, M., Valette, B., Kostoglodov, V., & Cotte, N. (2011). Spatial and temporal evolution of a long term slow slip event: the 2006 Guerrero Slow Slip Event. *Geophysical Journal International*, *184*, 816–828. doi: https://doi.org/10.1111/j.1365-246X.2010.04866.x

Reverso, T., Marsan, D., Helmstetter, A., & Enescu, B. (2016). Background seismicity in Boso Peninsula, Japan: Long-term acceleration, and relationship with slow slip events. *Geophysical Research Letters*, *43*, 5671–5679. doi: https://doi.org/10.1002/2016GL068524

Rousset, B., Fu, Y., Bartlow, N., & Bürgmann, R. (2019). Weeks-long and years-long slow slip and tectonic tremor episodes on the south central Alaska megathrust. *Journal of Geophysical Research: Solid Earth*, *124*, 13,392–13,403. doi: https://doi.org/10.1029/2019JB018724

Ruiz, S., Moreno, M., Melnick, D., del Campo, F., Poli, P., Baez, J. C., ... Madariaga, R. (2017). Reawakening of large earthquakes in south central Chile: The 2016 Mw 7.6 Chiloé event. *Geophysical Research Letters*, *44*, 6633–6640. doi: https://doi.org/10.1002/2017GL074133

Rust, D., Korzhenkov, A., & Tibaldi, A. (2018). Geologic slip-rate determinations on the Talas-Fergana fault: Mismatch with geodetic slip rate. *Geophysical Research Letters*, *45*, 3880–3888. doi: https://doi.org/10.1002/2017GL076990

Sagiya, T. (2004). Interplate coupling in the Kanto district, central Japan, and the Boso Peninsula silent earthquake in May 1996. *Pure and Applied Geophysics*, *161*, 2327—2342. doi: https://doi.org/10.1007/s00024-004-2566-6

Savage, J. C., & Thatcher, W. (1992). Interseismic deformation at the Nankai Trough, Japan, subduction zone. *Journal of Geophysical Research*, *97*(B7), 11,117–11,135. doi: https://doi.org/10.1029/92JB00810

Shishikura, M. (2014). History of the paleo-earthquake along the Sagami Trough, central Japan: Review of coastal paleo-seismological studies in the Kanto region. *Episodes*, *37*(4), 246–257.

Sugawara, D., Goto, K., Imamura, F., Matsumoto, H., & Minoura, K. (2012). Assessing the magnitude of the 869 Jogan tsunami using sedimentary deposits: Prediction and consequence of the 2011 Tohoku-oki tsunami. *Sedimentary Geology*, *282*, 14–26. doi: https://doi.org/10.1016/j.sedgeo.2012.08.001

Tarantola, A., & Valette, B. (1982). Generalized nonlinear inverse problems solved using the least squares criterion. *Reviews of Geophysics and Space Physics*, *20*(2), 219-232. doi: https://doi.org/10.1029/RG020i002p00219

Tran, D. T. (2009). *Analyse rapide et robuste des solutions GPS pour la tectonique [in French]* (Doctoral dissertation). Université de Nice-Sophia Antipolis, Nice, France.

Tsuji, H., Hatanaka, Y., Hiyama, Y., Yamaguchi, K., Furuya, T., Kawamoto, S., & Fukuzaki, Y. (2017). Twenty-year successful operation of GEONET. *Bulletin of the Geospatial Information Authority of Japan*, *65*, 19-44.

Uhira, K., Baba, T., Mori, H., Katayama, H., & Hamada, N. (2005). Earthquake swarms preceding the 2000 eruption of Miyakejima volcano, Japan. *Bulletin of Volcanology*, *67*, 219–230. doi: https://doi.org/10.1007/s00445-004-0405-3

Walser, P., Fridez, P., Lutz, S., & Dach, R. (2015). Bernese GNSS software Version 5.2 [Computer software manual].

Wang, K., Hu, Y., Bevis, M., Kendrick, E., Smalley, R., Vargas, R. B., & Lauría, E. (2007). Crustal motion in the zone of the 1960 Chile earthquake: Detangling earthquake-cycle deformation and forearc-sliver translation. *Geochemistry, Geophysics, Geosystems*, *8*(Q10010). doi: https://doi.org/10.1029/2007GC001721

Yagi, Y., & Kikuchi, M. (2003). Partitioning between seismogenic and aseismic slip as highlighted from slow slip events in Hyuga-nada, Japan. *Geophysical*

Research Letters, *30*(2), 1087. doi: https://doi.org/10.1029/2002GL015664

Yamanaka, Y., & Kikuchi, M. (2003). Source process of the recurrent Tokachi-oki earthquake on September 26, 2003, inferred from teleseismic body waves. *Earth, Planets and Space*, *55*, e21–e24. doi: https://doi.org/10.1186/BF03352479

Yokota, Y., & Koketsu, K. (2015). A very long-term transient event preceding the 2011 Tohoku earthquake. *Nature Communications*, *6*(5934). doi: https://doi.org/10.1038/ncomms6934

Yoshioka, S., Matsuoka, Y., & Ide, S. (2015). Spatiotemporal slip distributions of three long-term slow slip events beneath the Bungo Channel, southwest Japan, inferred from inversion analyses of GPS data. *Geophysical Journal International*, *201*, 1437–1455. doi: https://doi.org/10.1093/gji/ggv022

Figure 1.

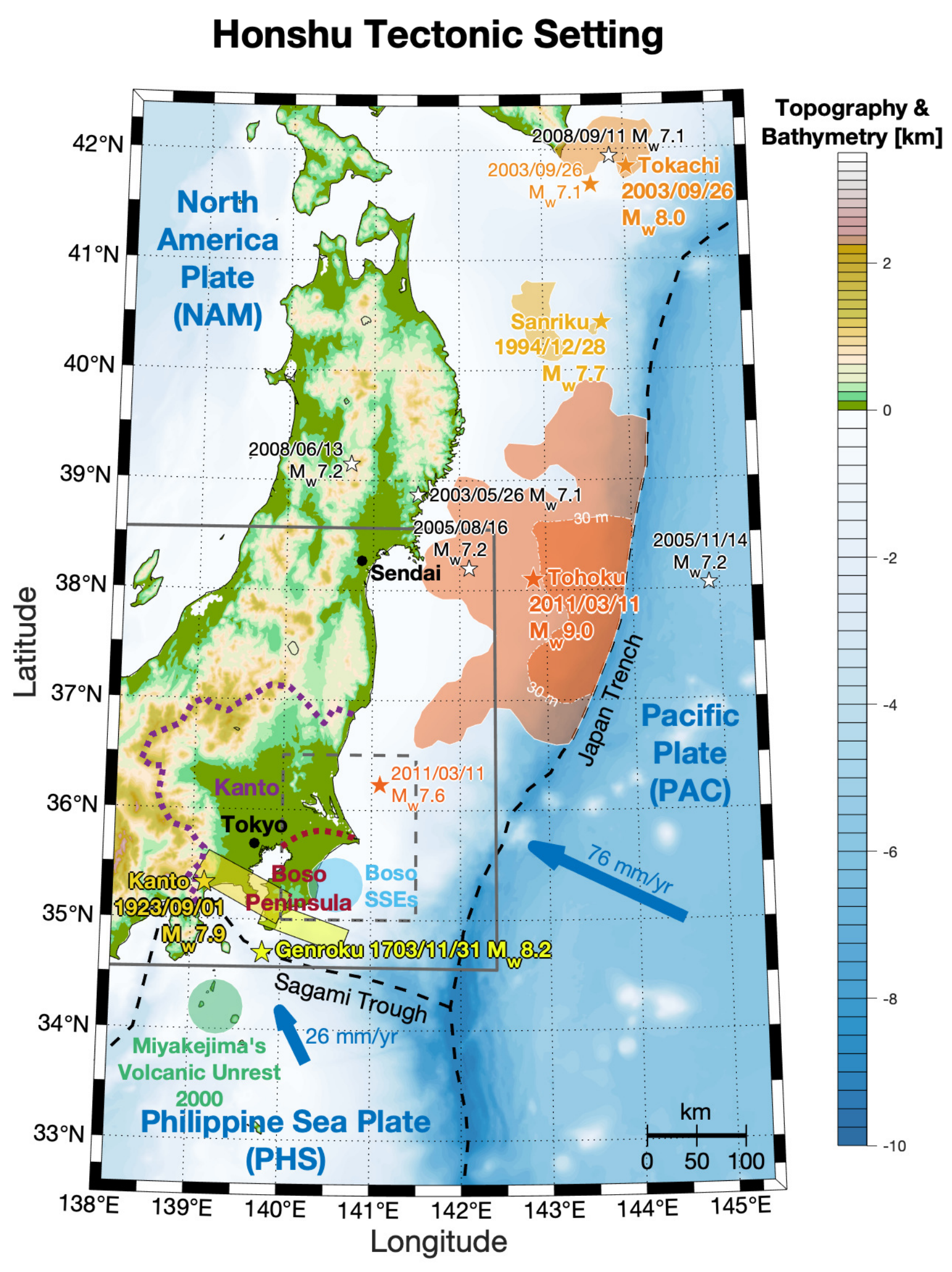
Honshu Tectonic Setting
Topography & Bathymetry [km]
2
0
-2
-4
-6
-8
-10
North America Plate (NAM)
Pacific Plate (PAC)
Philippine Sea Plate (PHS)
2008/09/11 Mw 7.1
2003/09/26 Mw 7.1
Tokachi 2003/09/26 Mw 8.0
Sanriku 1994/12/28 Mw 7.7
2008/06/13 Mw 7.2
2003/05/26 Mw 7.1
2005/08/16 Mw 7.2
2005/11/14 Mw 7.2
Sendai
Tohoku 2011/03/11 Mw 9.0
30 m
30 m
Japan Trench
2011/03/11 Mw 7.6
Kanto
Tokyo
Kanto 1923/09/01 Mw 7.9
Boso Peninsula
Boso SSEs
Genroku 1703/11/31 Mw 8.2
76 mm/yr
Sagami Trough
26 mm/yr
Miyakejima's Volcanic Unrest 2000
km
0 50 100
42°N
41°N
40°N
39°N
38°N
37°N
36°N
35°N
34°N
33°N
138°E
139°E
140°E
141°E
142°E
143°E
144°E
145°E
Latitude
Longitude

Figure 2.

(a)

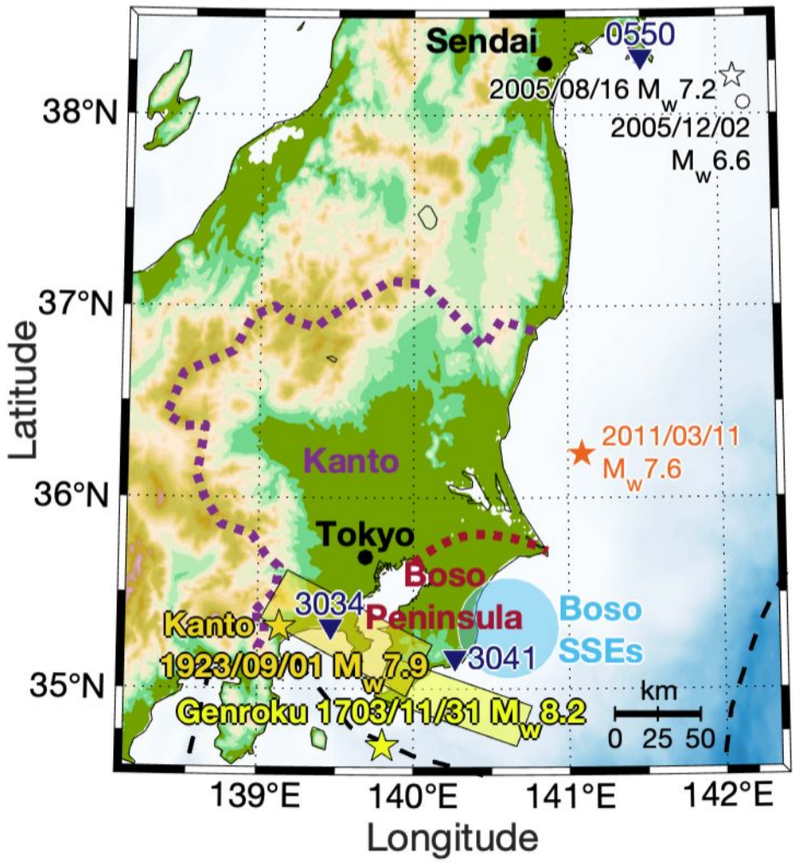
Station positions
Sendai
0550
2005/08/16 M_w 7.2
2005/12/02
M_w 6.6
38°N
37°N
36°N
35°N
Latitude
Kanto
2011/03/11
M_w 7.6
Tokyo
Boso
Peninsula
3034
Kanto
1923/09/01 M_w 7.9
3041
Boso
SSEs
Genroku 1703/11/31 M_w 8.2
km
0 25 50
139°E
140°E
141°E
142°E
Longitude

(b)

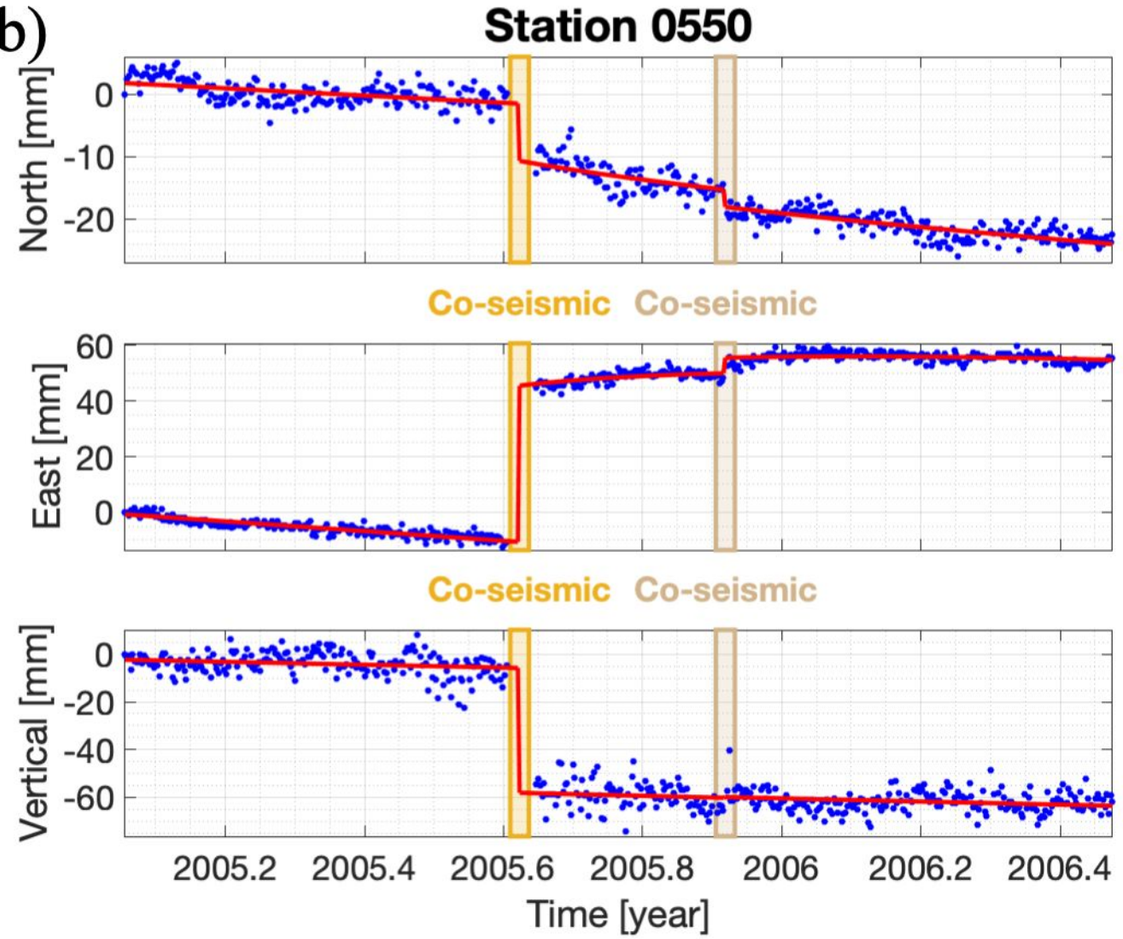
Station 0550
North [mm]
0
-10
-20
Co-seismic
Co-seismic
East [mm]
60
40
20
0
Co-seismic
Co-seismic
Vertical [mm]
0
-20
-40
-60
2005.2
2005.4
2005.6
2005.8
2006
2006.2
2006.4
Time [year]

(c)

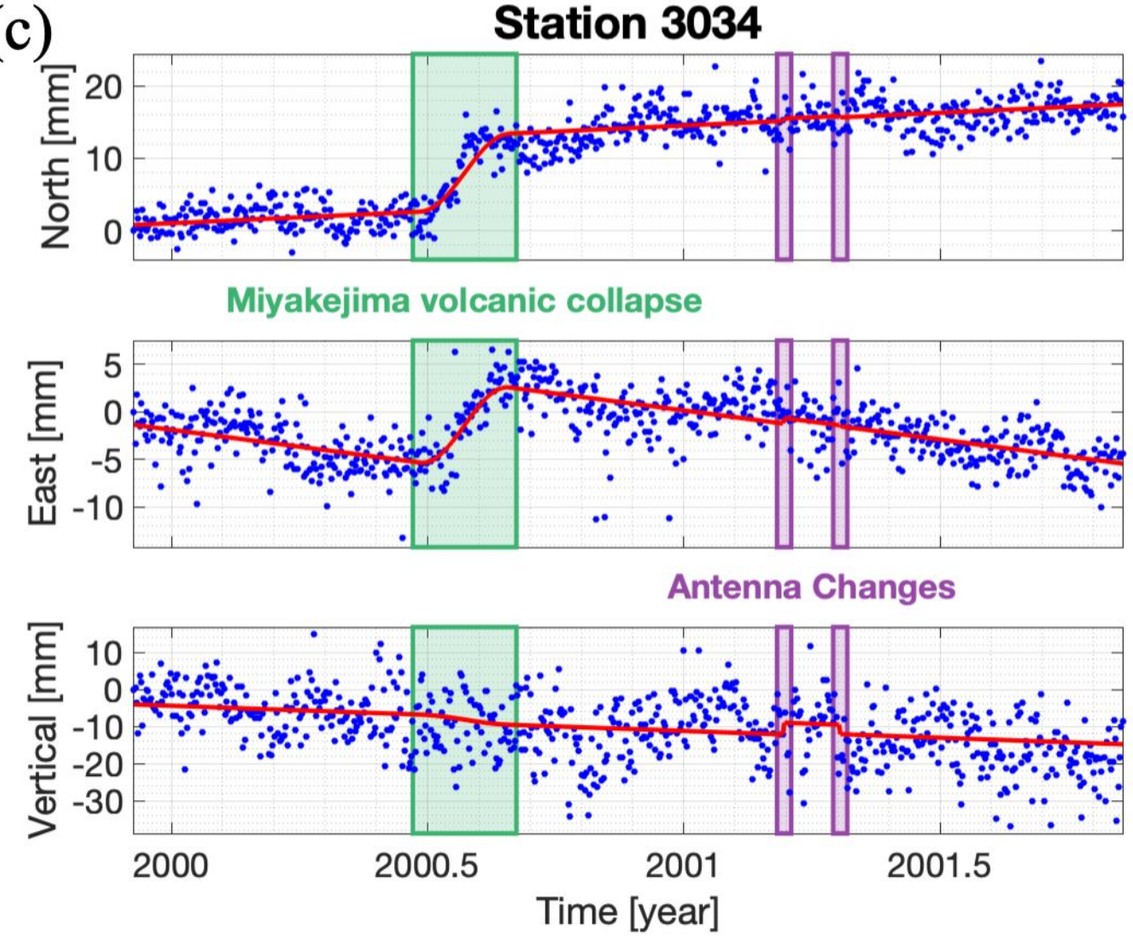
Station 3034
North [mm]
20
10
0
Miyakejima volcanic collapse
East [mm]
5
0
-5
-10
Antenna Changes
Vertical [mm]
10
0
-10
-20
-30
2000
2000.5
2001
2001.5
Time [year]

(d)

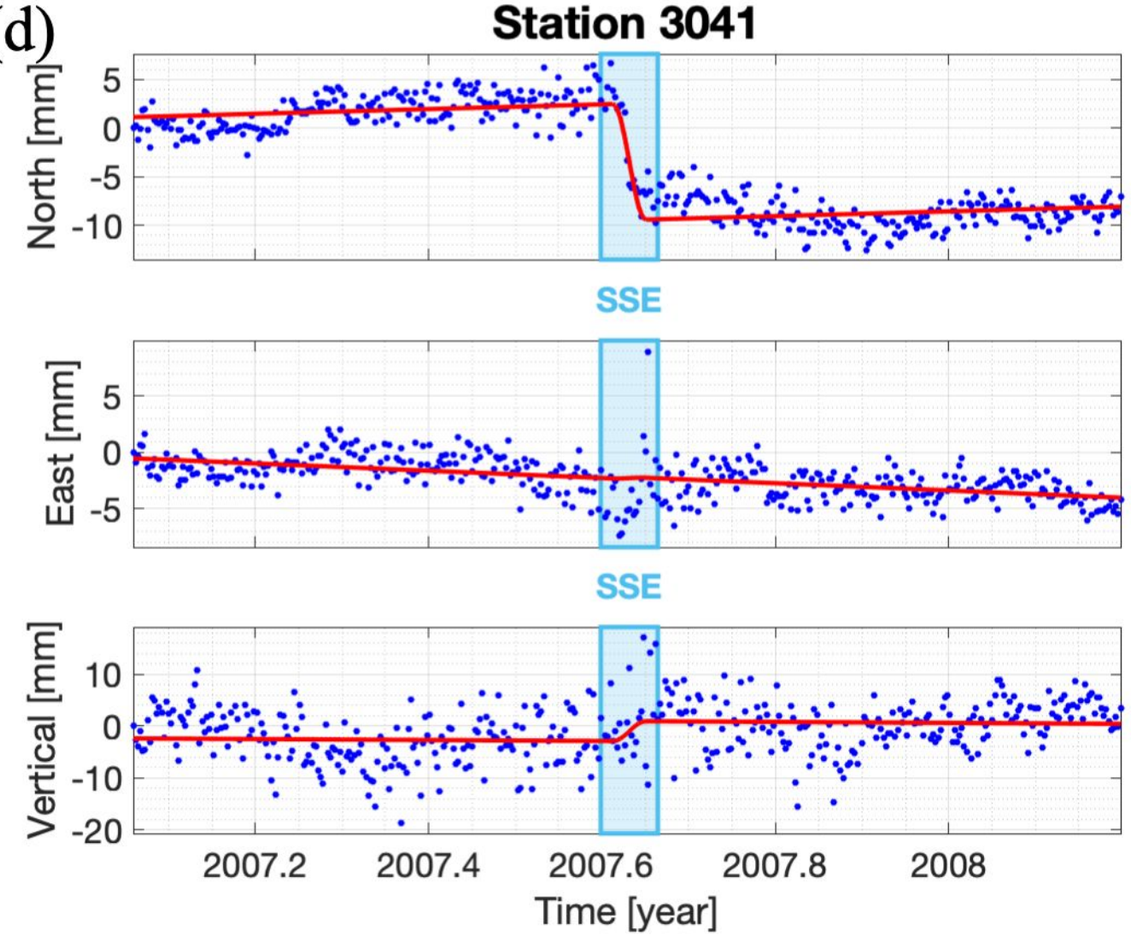
Station 3041
North [mm]
5
0
-5
-10
SSE
East [mm]
5
0
-5
SSE
Vertical [mm]
10
0
-10
-20
2007.2
2007.4
2007.6
2007.8
2008
Time [year]

Figure 3.

(a)

Station 3041 - Linear model

Time series (blue) + Model (red)

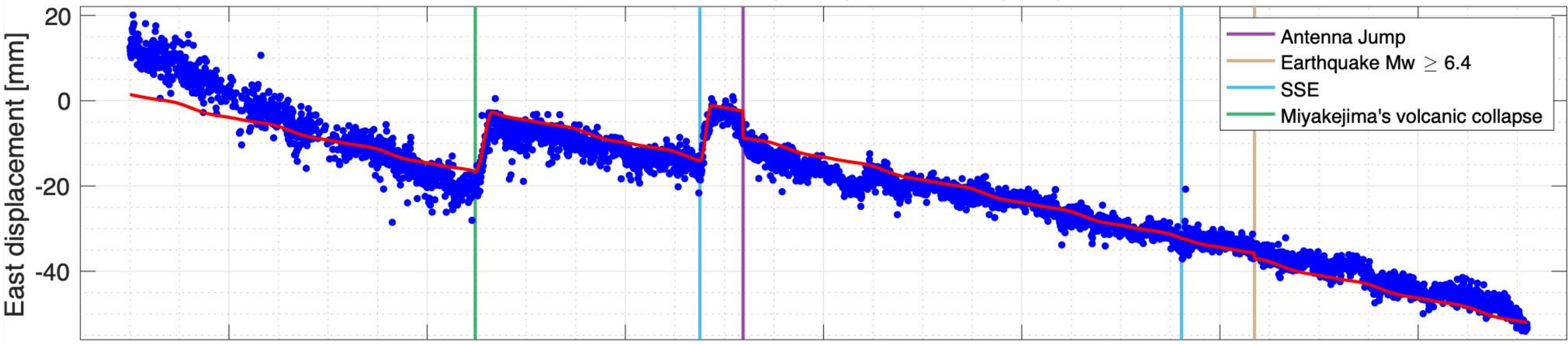

Residuals (green)

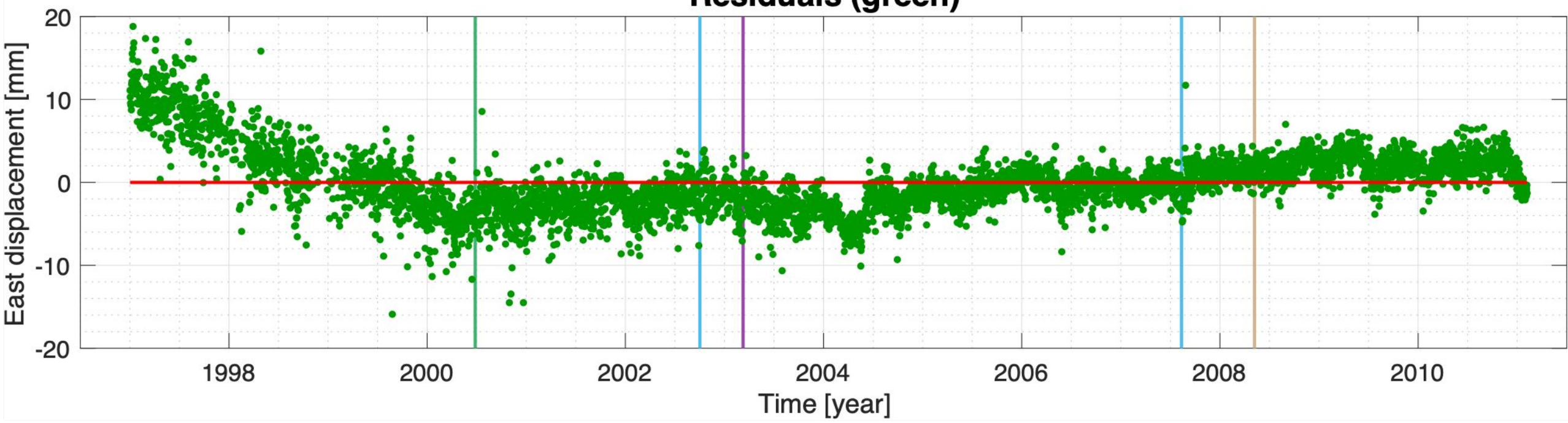

(b)

Station 3041 - Quadratic model

Time series (blue) + Model (red)

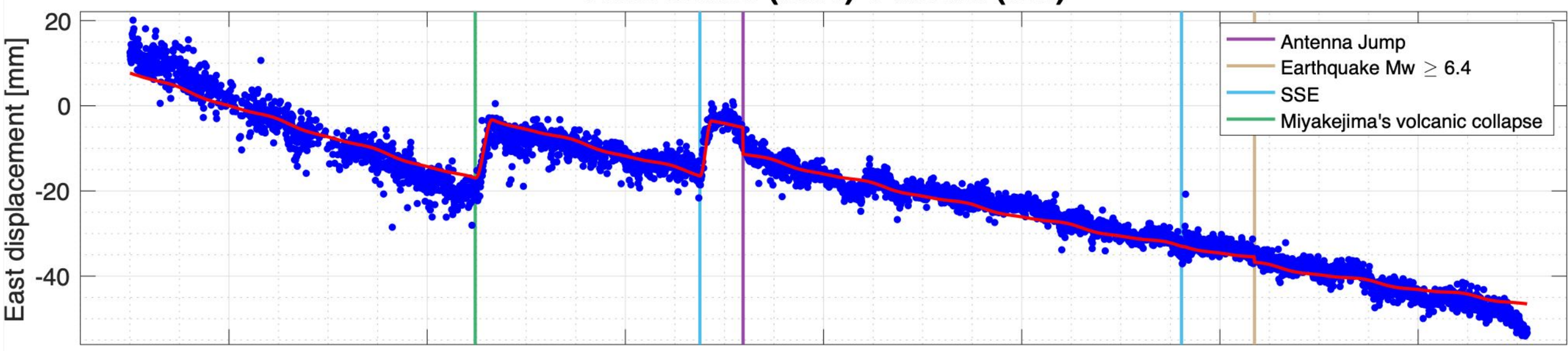

Residuals (green)

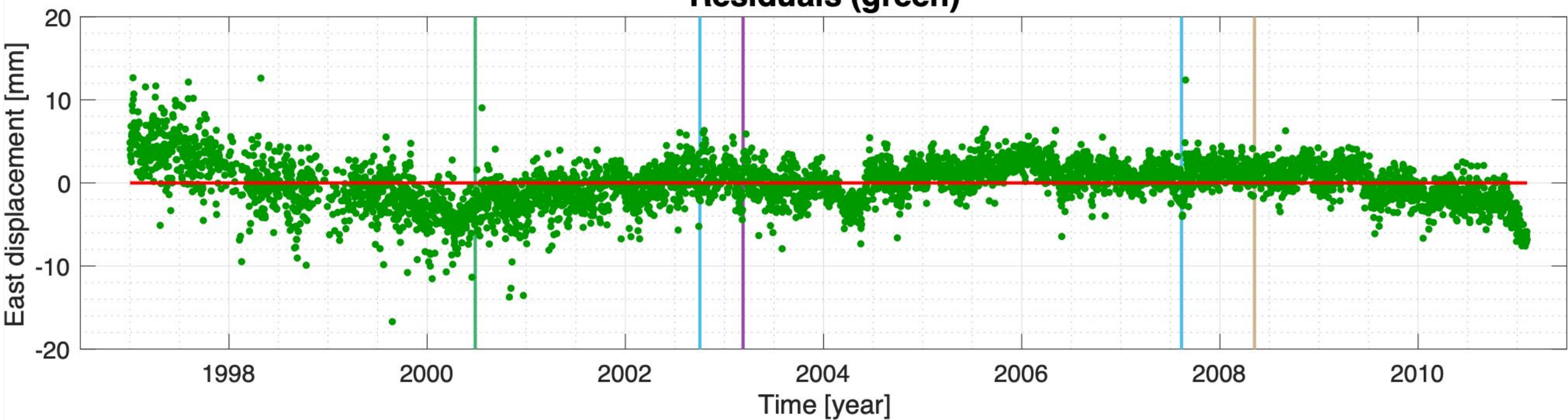

Figure 4.

(a) **Coupling of the PAC-NAM interface**
considering PHS-NAM

(b) **Coupling of the PHS-NAM interface**
considering PAC-NAM

North America Plate (NAM)
Pacific Plate (PAC)
Philippine Sea Plate (PHS)
2008/09/11 M_w7.1
2003/09/26 M_w7.1
Tokachi 2003/09/26 M_w8.0
2005/11/14 M_w7.2
Japan Trench
Kanto 1923/09/01 M_w7.9
Miyakejima's Volcanic Unrest 2000
76 mm/yr
20mm/yr
Observed velocity
Predicted velocity
km
0 50 100
Latitude
Longitude
Coupling [v_{PAC} = 76 mm/yr]
Sanriku 1994/12/28 M_w7.7
2003/05/26 M_w7.1
2005/08/16 M_w7.2
Sendai
Tohoku 2011/03/11 M_w9.0
2011/03/11 M_w7.6
Boso SSEs
Sagami Trough
26 mm/yr
Coupling [v_{PHS} = 26 mm/yr]

Figure 5.

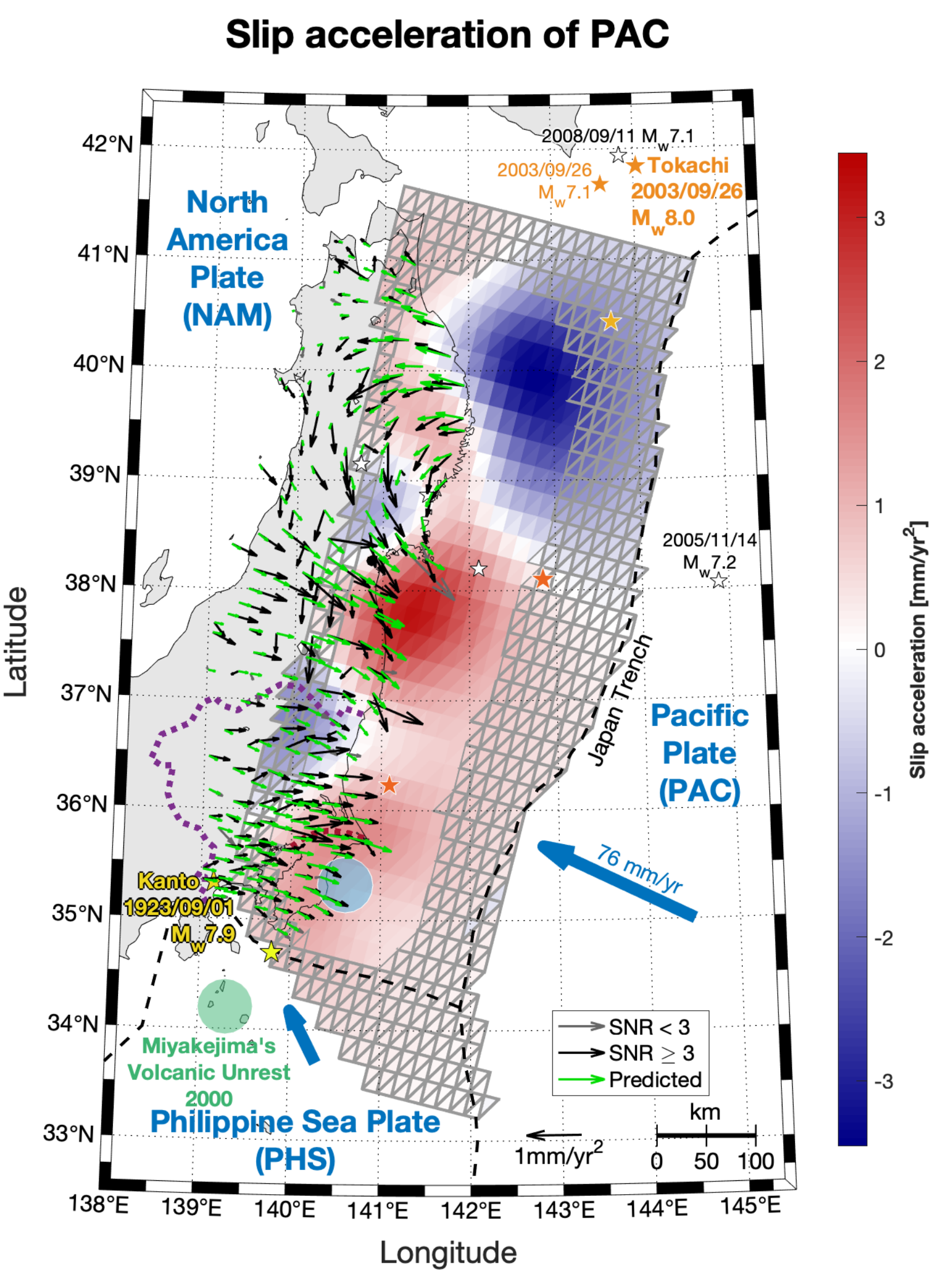
Slip acceleration of PAC
2008/09/11 M_w 7.1
2003/09/26 M_w 7.1
Tokachi 2003/09/26 M_w 8.0
North America Plate (NAM)
2005/11/14 M_w 7.2
Japan Trench
Pacific Plate (PAC)
76 mm/yr
Kanto 1923/09/01 M_w 7.9
Miyakejima's Volcanic Unrest 2000
Philippine Sea Plate (PHS)
SNR < 3
SNR ≥ 3
Predicted
1mm/yr^2
km
0 50 100
Slip acceleration [mm/yr^2]
3
2
1
0
-1
-2
-3
42°N
41°N
40°N
39°N
38°N
37°N
36°N
35°N
34°N
33°N
138°E
139°E
140°E
141°E
142°E
143°E
144°E
145°E
Latitude
Longitude

Figure 6.

(a)

Slip acceleration of PAC

from the F3 solution

(b)

Slip acceleration difference of PAC

between GAMIT/GLOBK processing and the F3 solution

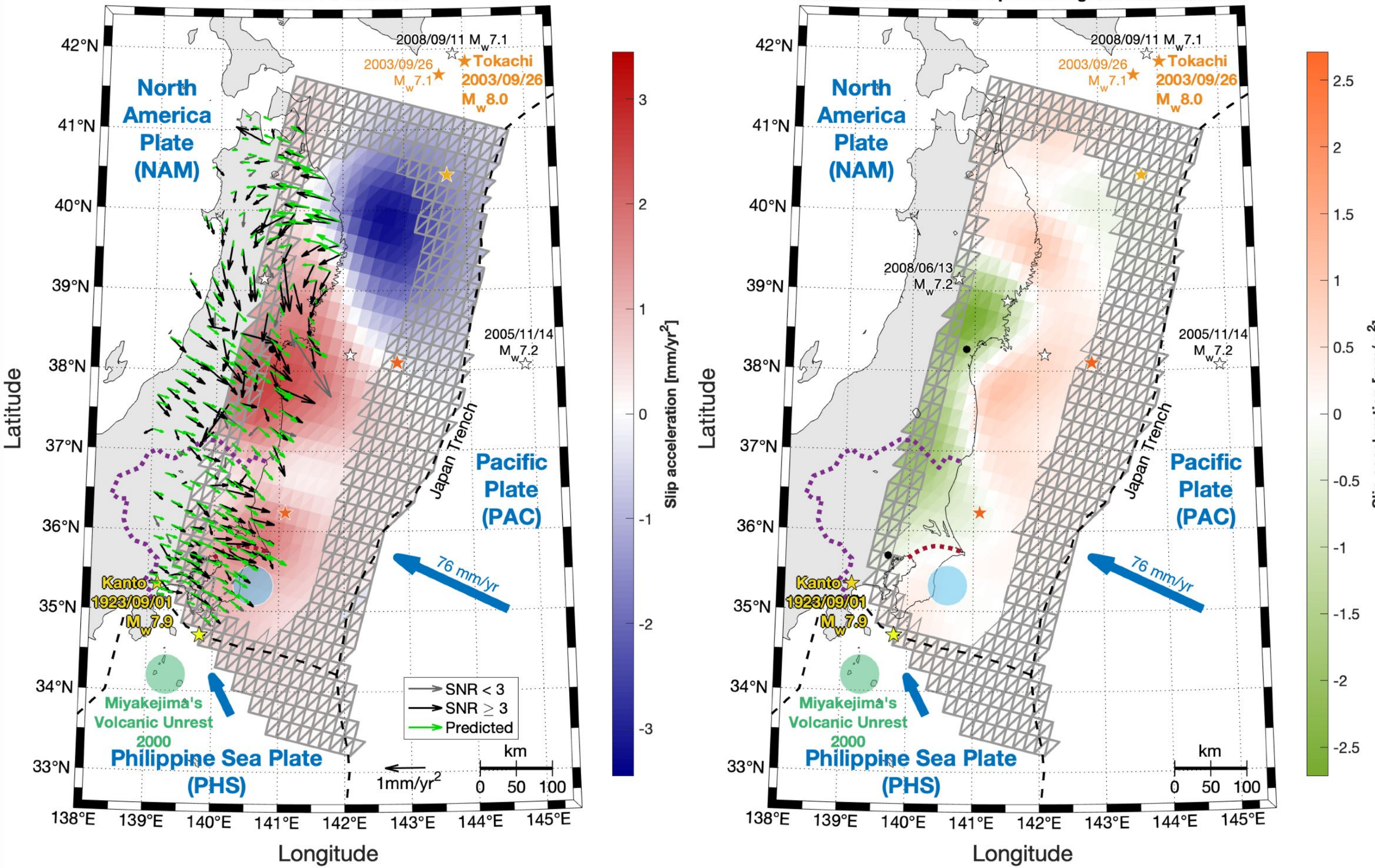

Figure 7.

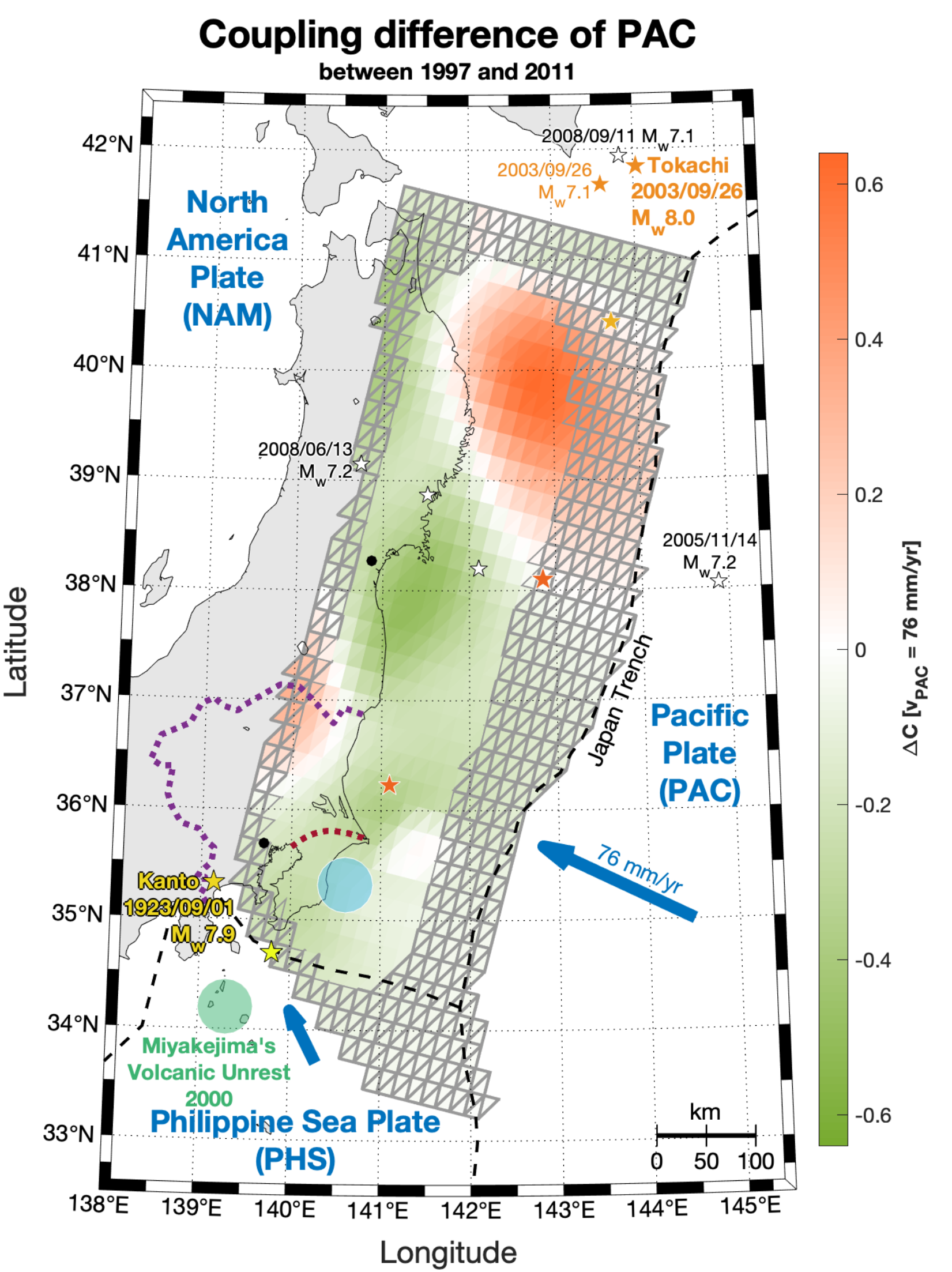
Coupling difference of PAC
between 1997 and 2011
2008/09/11 Mw7.1
2003/09/26
Mw7.1
Tokachi
2003/09/26
Mw8.0
North
America
Plate
(NAM)
2008/06/13
Mw7.2
2005/11/14
Mw7.2
Japan Trench
Pacific
Plate
(PAC)
76 mm/yr
Kanto
1923/09/01
Mw7.9
Miyakejima's
Volcanic Unrest
2000
Philippine Sea Plate
(PHS)
km
0 50 100
42°N
41°N
40°N
39°N
38°N
37°N
36°N
35°N
34°N
33°N
138°E
139°E
140°E
141°E
142°E
143°E
144°E
145°E
Latitude
Longitude
0.6
0.4
0.2
0
-0.2
-0.4
-0.6
ΔC [vPAC = 76 mm/yr]

Figure 8.

(a) **Seismic acceleration**
between 1997 and 2011

(b) **Coupling of the PAC-NAM interface**
in 1997, considering PHS-NAM

(c) **Prior model for slip acceleration of PAC**
from seismic acceleration

(d) **Slip acceleration of PAC**
with seismic acceleration prior model

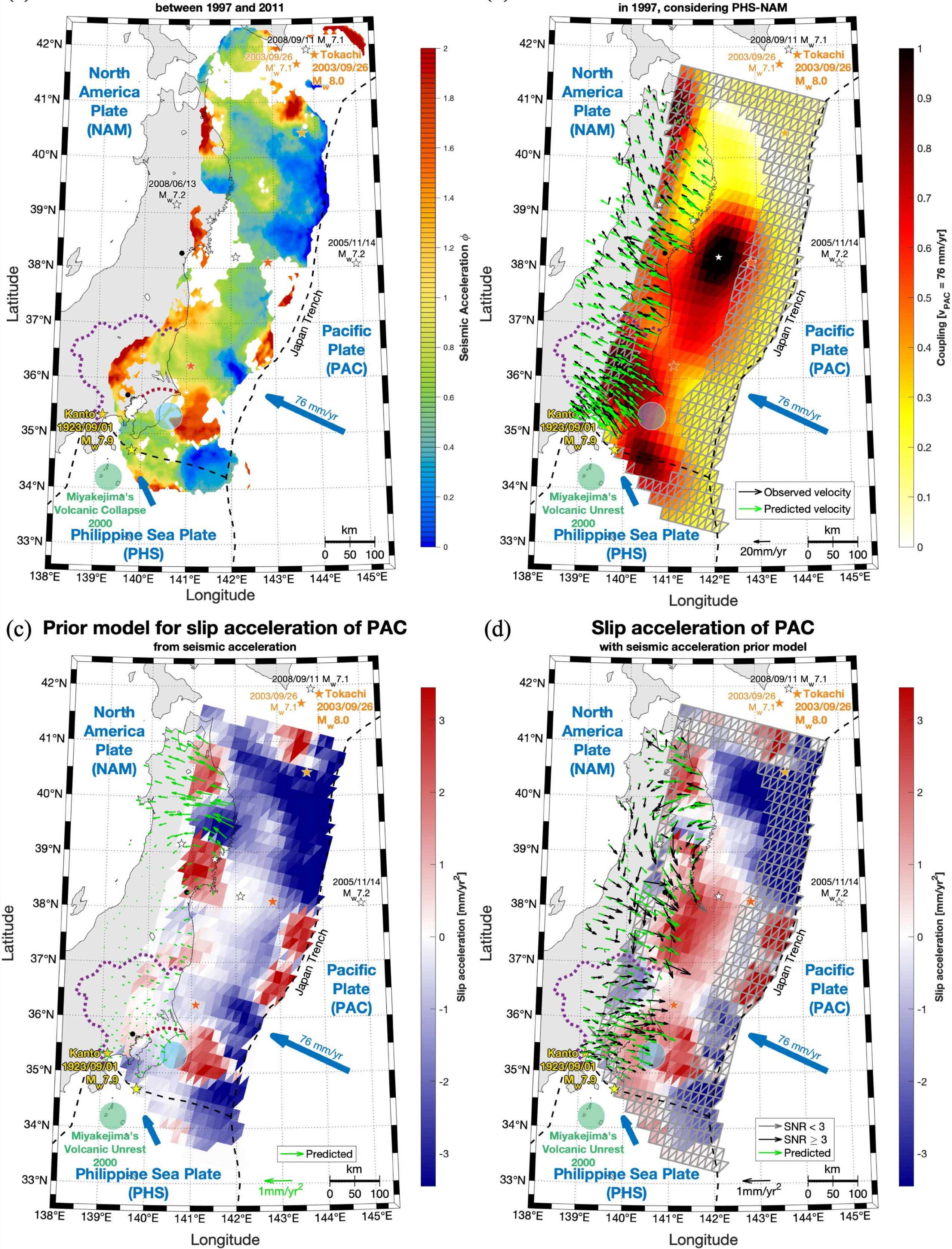

Figure 9.

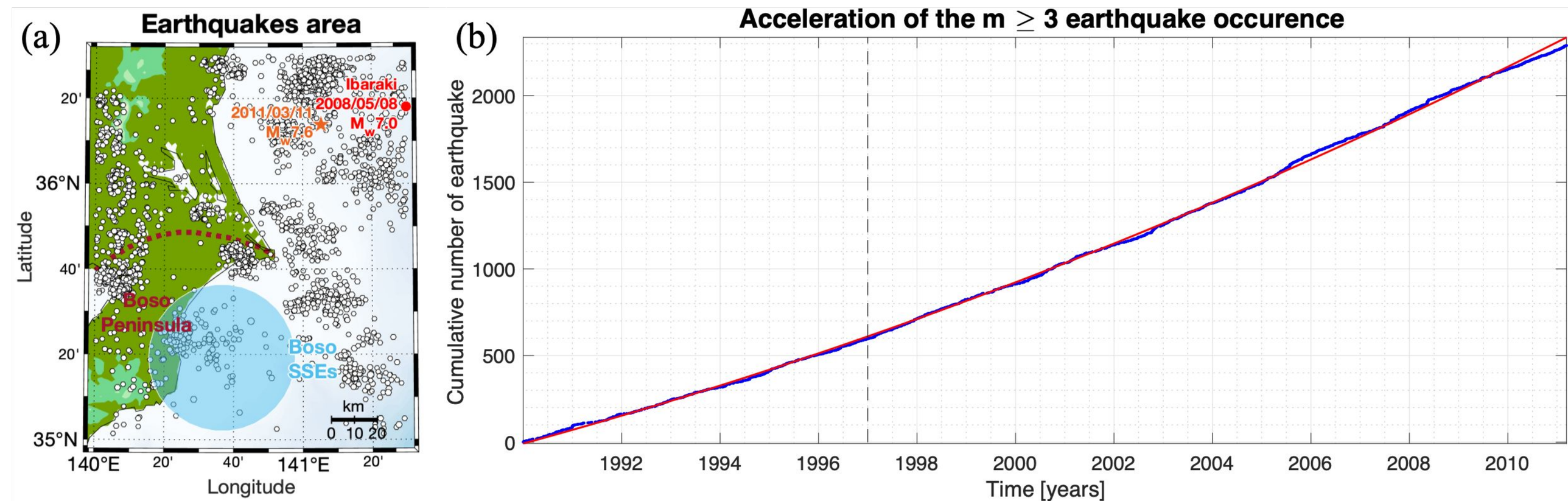
(a)
Earthquakes area
Ibaraki
2008/05/08
M w 7.0
2011/03/11
M w 7.6
Boso
Peninsula
Boso
SSEs
km
0 10 20
20'
36°N
40'
20'
35°N
140°E
20'
40'
141°E
20'
Latitude
Longitude
(b)
Acceleration of the m ≥ 3 earthquake occurence
Cumulative number of earthquake
0
500
1000
1500
2000
1992
1994
1996
1998
2000
2002
2004
2006
2008
2010
Time [years]

Supporting Information for "14-year acceleration along the Japan trench and the Sagami trough"

Lou Marill[1], David Marsan[1], Anne Socquet[1], Mathilde Radiguet [1], Nathalie Cotte[1], and Baptiste Rousset[2]

[1]Univ. Grenoble Alpes, Univ. Savoie Mont Blanc, CNRS, IRD, Univ. Gustave Eiffel, ISTerre, 38000 Grenoble, France

[2]Univ. Calif. Berkeley, Dept. Earth & Planetary Sci., Berkeley, CA 94720 USA

Contents of this file

1. Text S1

2. Table S1

3. Figures S1 to S18

Text S1

To describe the transformation of the GPS time series from ITRF2005 to ITRF2014, we detail here the equations controling this transformation. Equation (1) represent the transformation of one point at the Epoch given time (2010.0), all the parameter values are given in Table S1 :

$$\begin{pmatrix} X_{ITRF2005} \\ Y_{ITRF2005} \\ Z_{ITRF2005} \end{pmatrix} = \begin{pmatrix} X_{ITRF2014} \\ Y_{ITRF2014} \\ Z_{ITRF2014} \end{pmatrix} + \begin{pmatrix} T_x \\ T_y \\ T_z \end{pmatrix} + \begin{pmatrix} D & -R_z & R_y \\ R_z & D & -R_x \\ -R_y & R_x & D \end{pmatrix} \begin{pmatrix} X_{ITRF2014} \\ Y_{ITRF2014} \\ Z_{ITRF2014} \end{pmatrix} \quad (1)$$

Equation (2) shows the value of any parameter P at any time t where $\dot{P}$ is the rate of the parameter :

$$P(t) = P(\text{Epoch}) + \dot{P} \times (t - \text{Epoch}) \quad (2)$$

Table S1. Transformation parameters from ITRF2014 to ITRF2005

Solution	T_x (mm)	T_y (mm)	T_z (mm)	D (ppb)	R_x (.001")	R_y (.001")	R_z (.001")	Epoch
Rates	T_x (mm/yr)	T_y (mm/yr)	T_z (mm/yr)	D (ppb/yr)	R_x (.001"/yr)	R_y (.001"/yr)	R_z (.001"/yr)	
ITRF2005	2.6	1.0	-2.3	0.92	0.00	0.00	0.00	2010.0
Rates	0.3	0.0	-0.1	0.03	0.00	0.00	0.00	

From the International Terrestrial Reference Frame website (http://itrf.ensg.ign.fr)

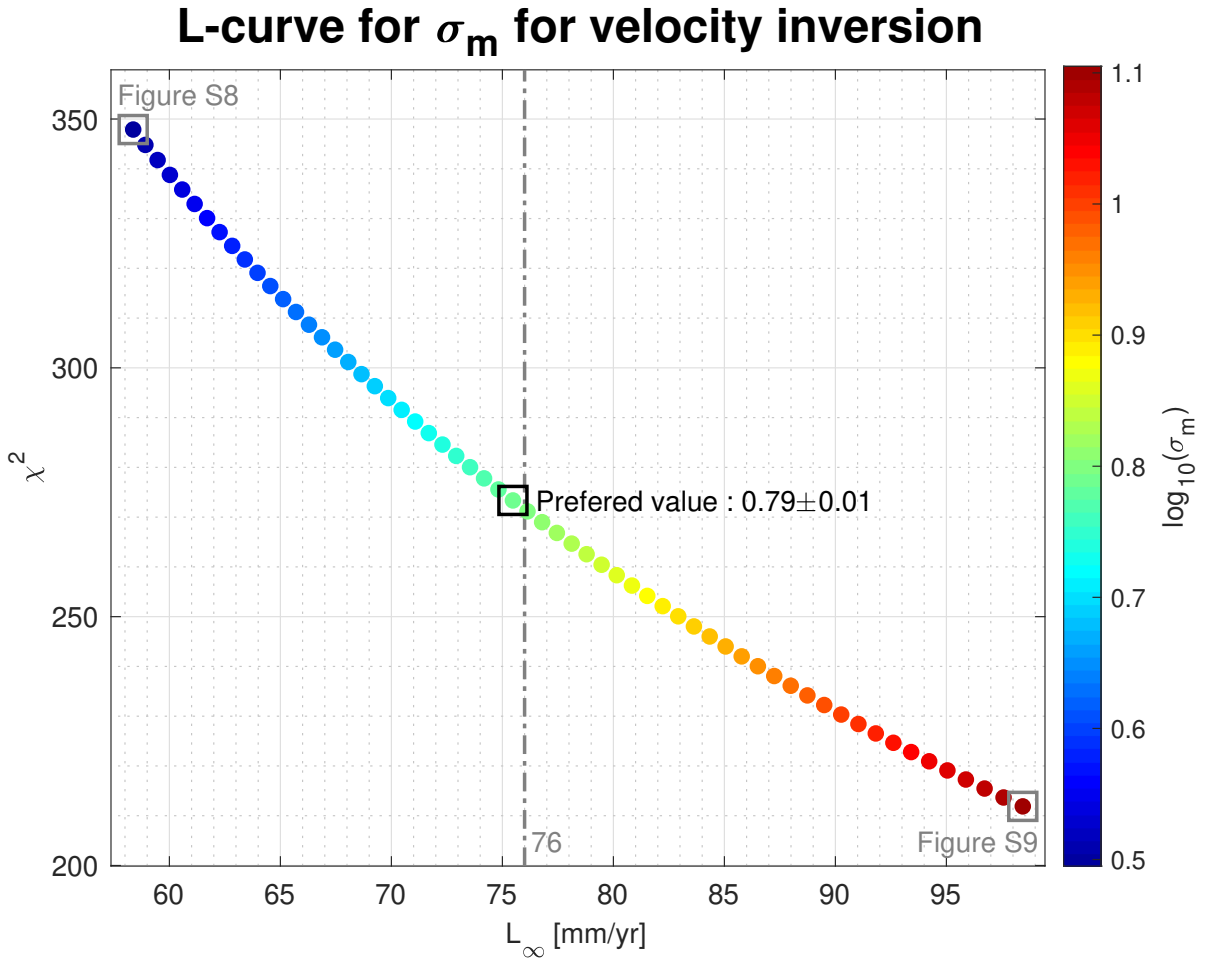

Figure S1. L-curve for σ_m determination for the velocity field inversion. The color correspond to the value of $\log_{10}(\sigma_m)$. Our preferred σ_m value is $10^{0.79}$ ($\log_{10}(\sigma_m) = 0.79$). All the inversion except Figures S8 and S9 are made for $\sigma_m = 10^{0.79}$. Alternative inversions are proposed for $\sigma_m = 10^{0.50}$ (Supplementary Figure S8) and $\sigma_m = 10^{1.10}$ (Supplementary Figure S9).

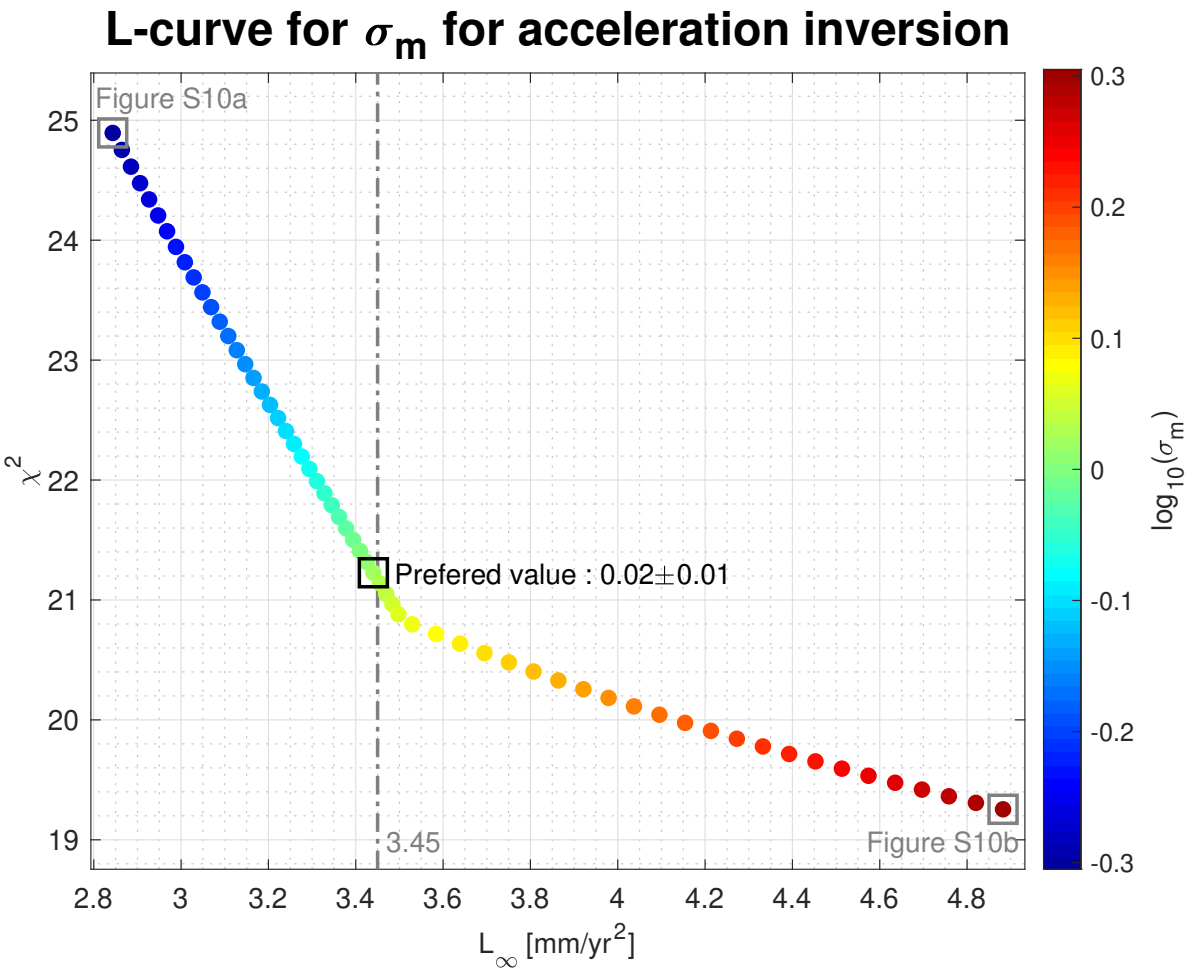

Figure S2. L-curve for σ_m determination for the acceleration field inversion. The color correspond to the value of $\log_{10}(\sigma_m)$. Our preferred σ_m value is $10^{0.02}$ ($\log_{10}(\sigma_m) = 0.02$). All the inversion except Supplementary Figure S10 are made for $\sigma_m = 10^{0.02}$. Alternative inversions are proposed for $\sigma_m = 10^{-0.30}$ (Supplementary Figure S10a) and $\sigma_m = 10^{0.30}$ (Supplementary Figure S10b).

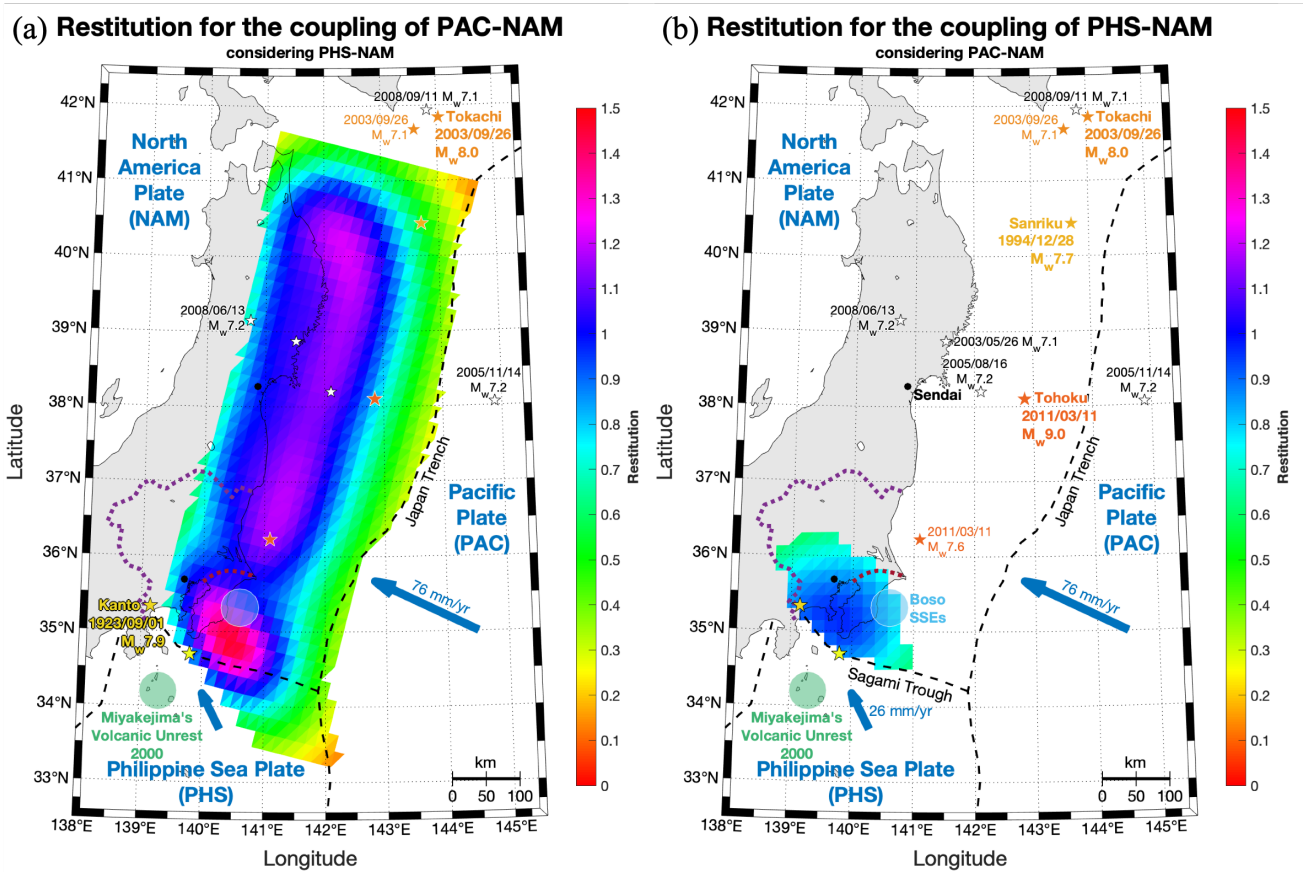

Figure S3. Restitution for the coupling of the Pacific-North America (PAC-NAM) interface (a) and the Philippine Sea-North America (PHS-NAM) interface (b). The color represent the amount of restitution of each sub-fault: 0, the slip is not restored and ∼1, the slip is fully restored. Other elements are described in Figure 1.

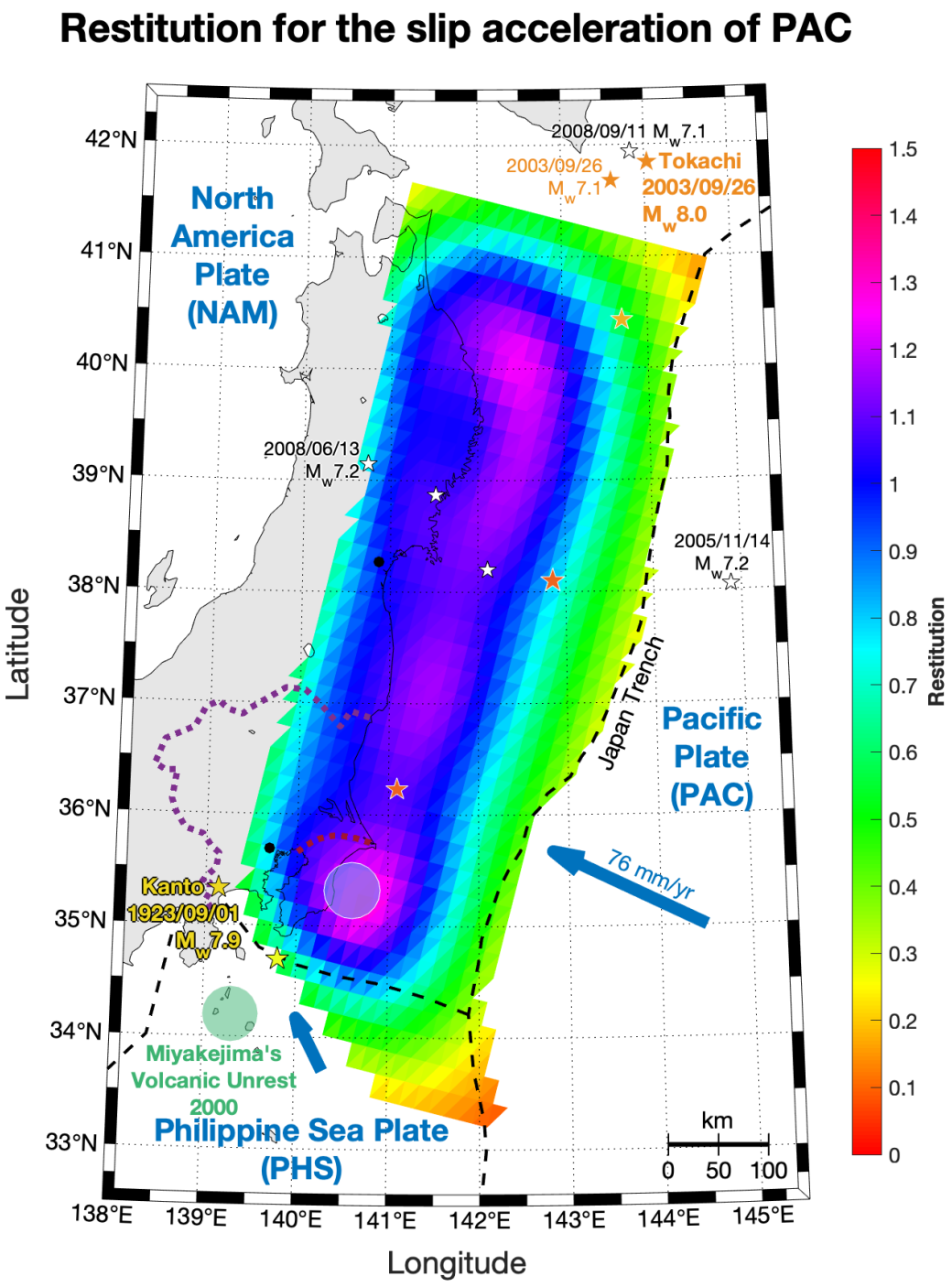

Figure S4. Restitution for the acceleration field inversion of the Pacific (PAC) plate. Same legend than Supplementary Figure S3.

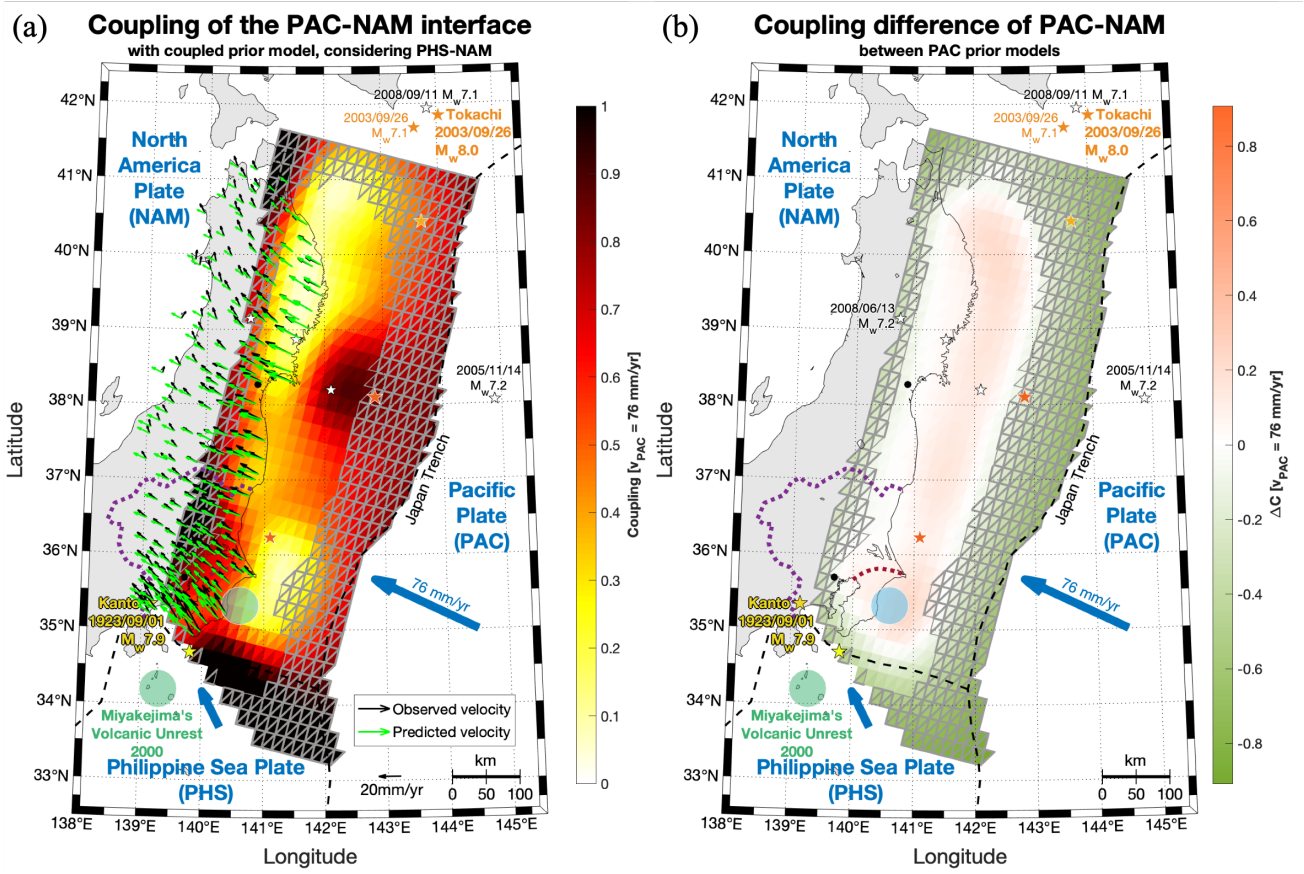

Figure S5. Coupling of the Pacific-North America (PAC-NAM) subduction interface with a fully coupled prior model (a) and the coupling difference between Figure 4a with an uncoupled prior model and (a). (a): Same legend as Figure 4. (b): Orange: sub-fault more coupled for the uncoupled prior model (Figure 4); green: sub-fault less coupled for the uncoupled prior model (Figure 4); other elements are described in Figure 1.

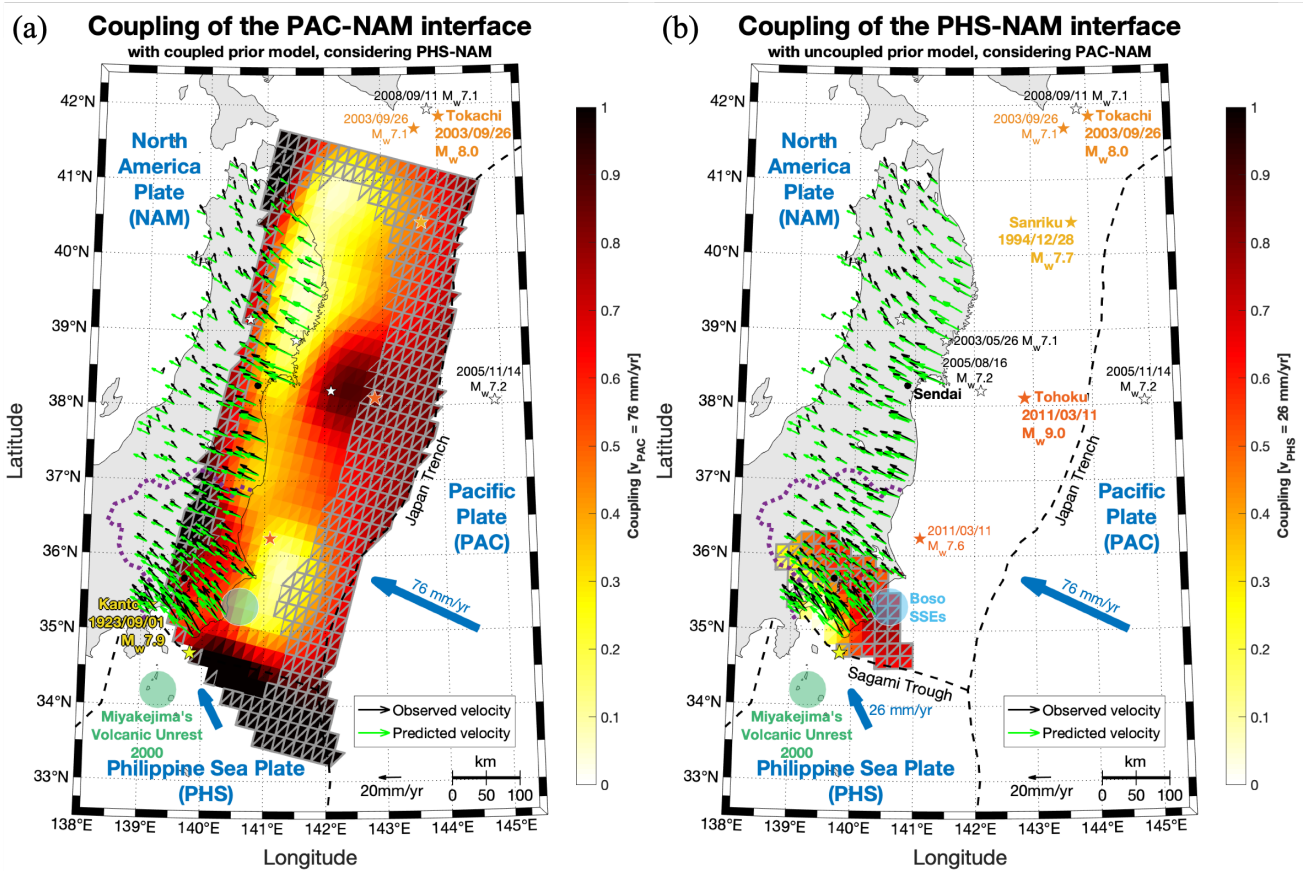

Figure S6. Coupling of the Pacific-North America (PAC-NAM) subduction interface with a fully coupled prior model (a) and coupling of the Philippine Sea-North America (PHS-NAM) subduction interface with a fully uncoupled prior model (b). Same legend as Figure 4.

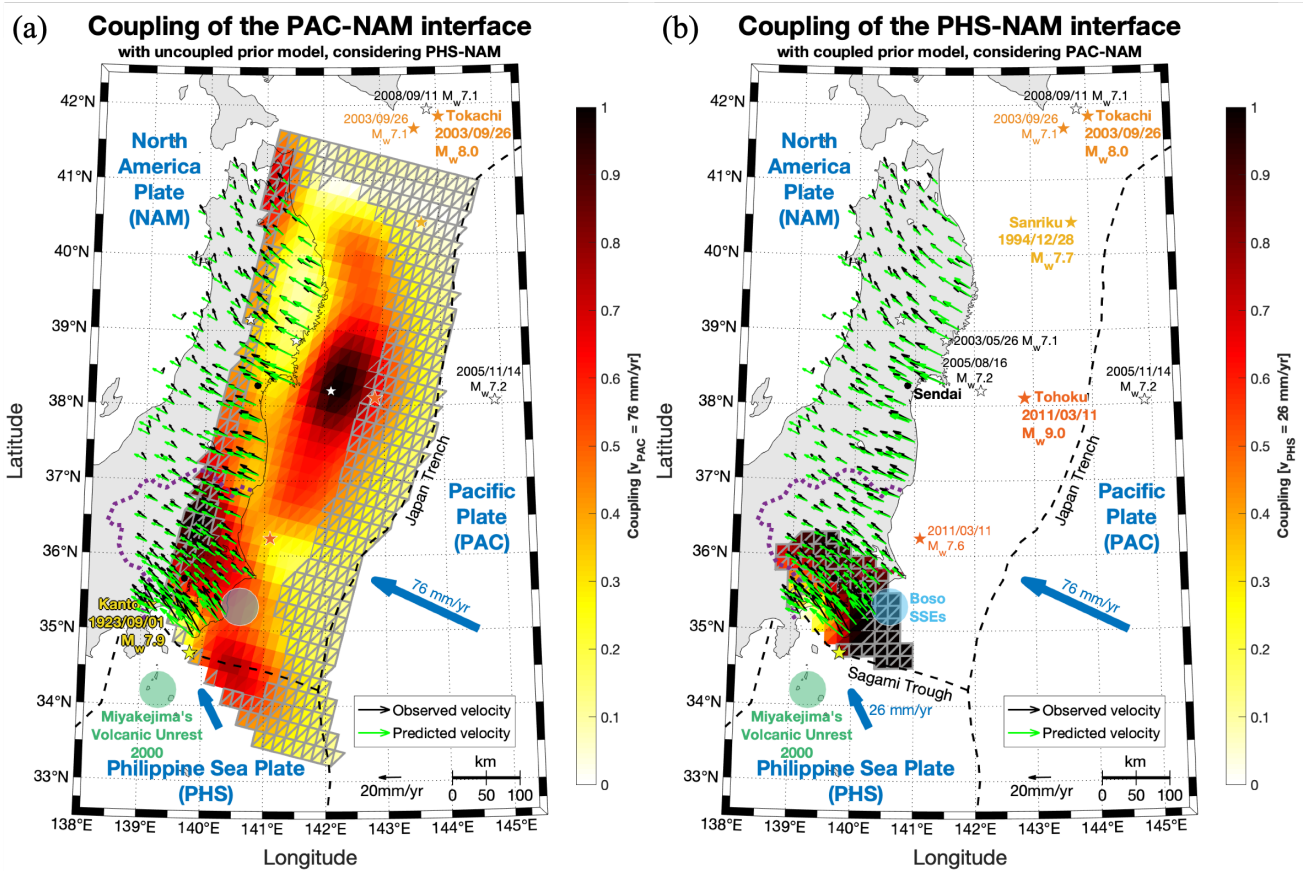

Figure S7. Coupling of the Pacific-North America (PAC-NAM) subduction interface with a fully uncoupled prior model (a) and coupling of the Philippine Sea-North America (PHS-NAM) subduction interface with a fully coupled prior model (b). Same legend as Figure 4.

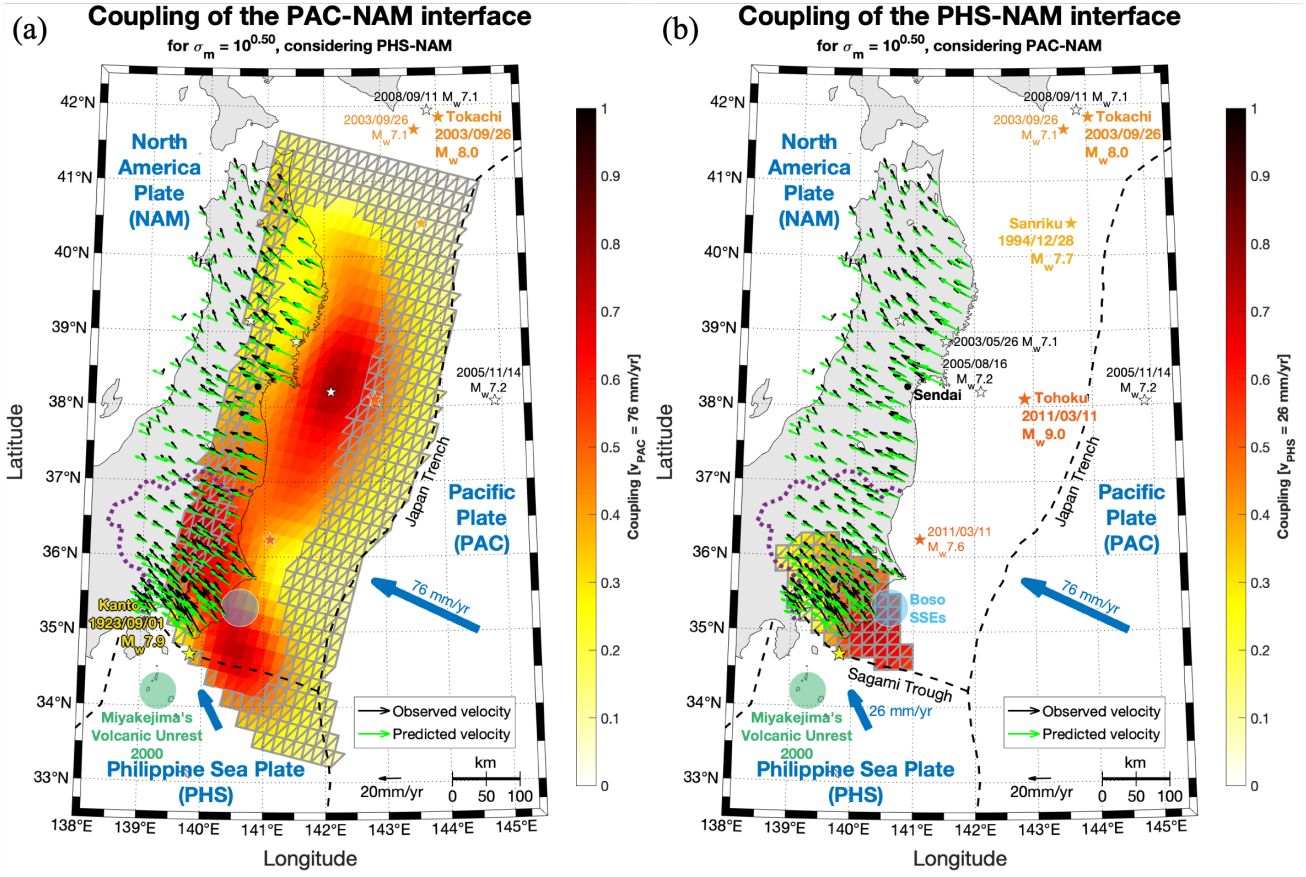

Figure S8. Coupling of the Pacific-North America (PAC-NAM) subduction interface (a) and the Philippine Sea-North America (PHS-NAM) subduction interface (b) for $\sigma_m = 10^{0.50}$. Same legend as Figure 4.

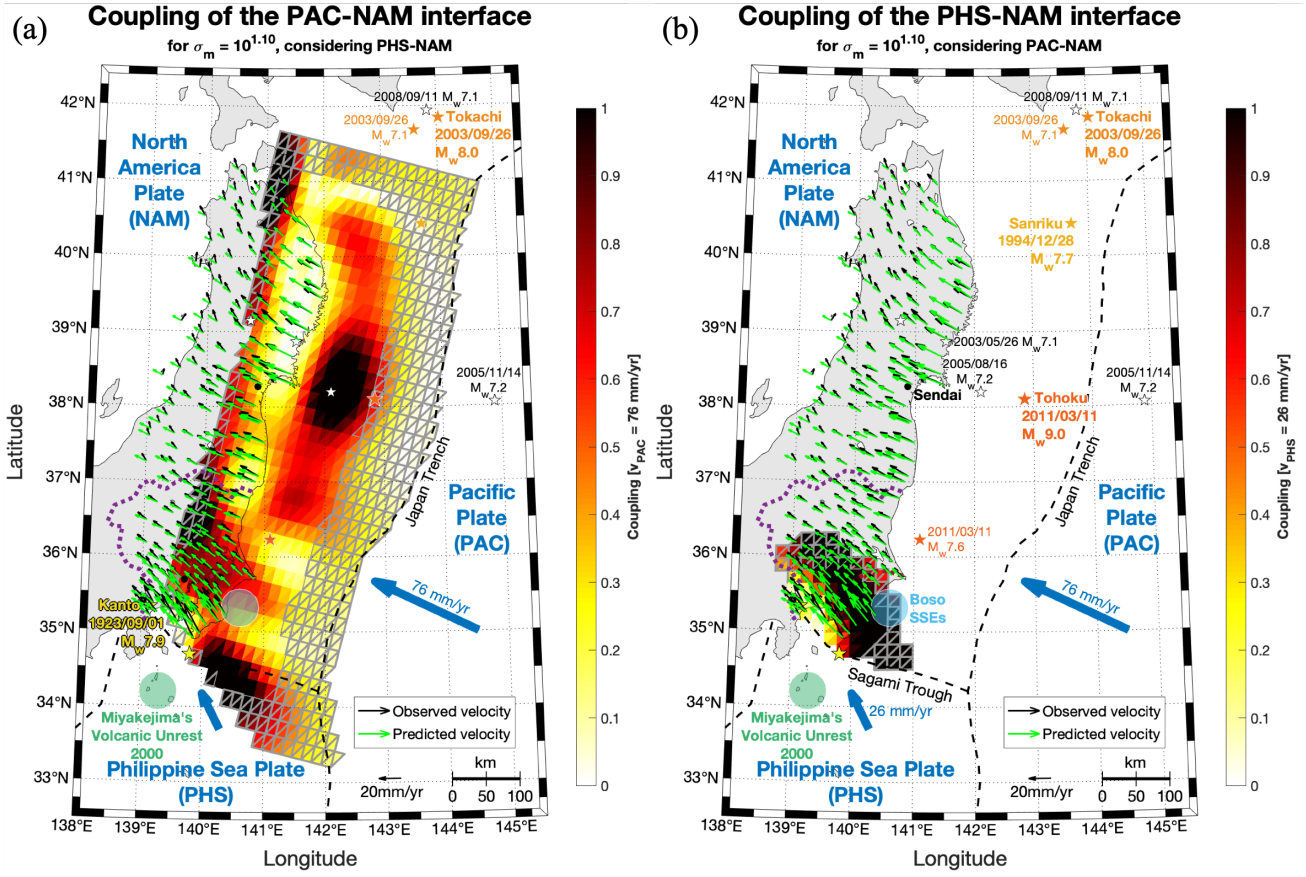

Figure S9. Coupling of the Pacific-North America (PAC-NAM) subduction interface (a) and the Philippine Sea-North America (PHS-NAM) subduction interface (b) for $\sigma_m = 10^{1.10}$. Same legend as in Figure 4.

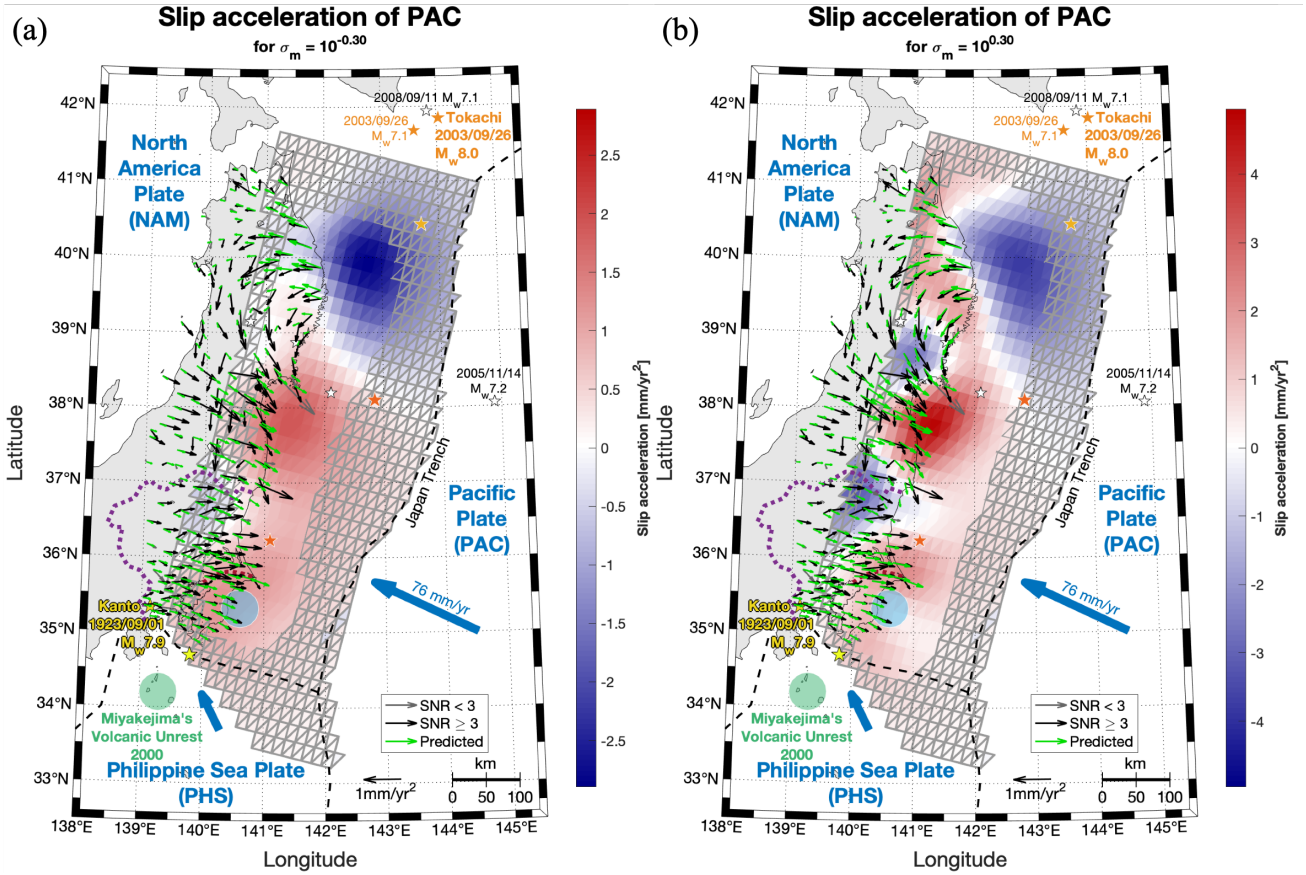

Figure S10. Slip acceleration of the Pacific (PAC) plate for $\sigma_m = 10^{-0.30}$ (a) and $\sigma_m = 10^{0.30}$ (b). Same legend as Figure 5. *Warning:* different colorbar scales!

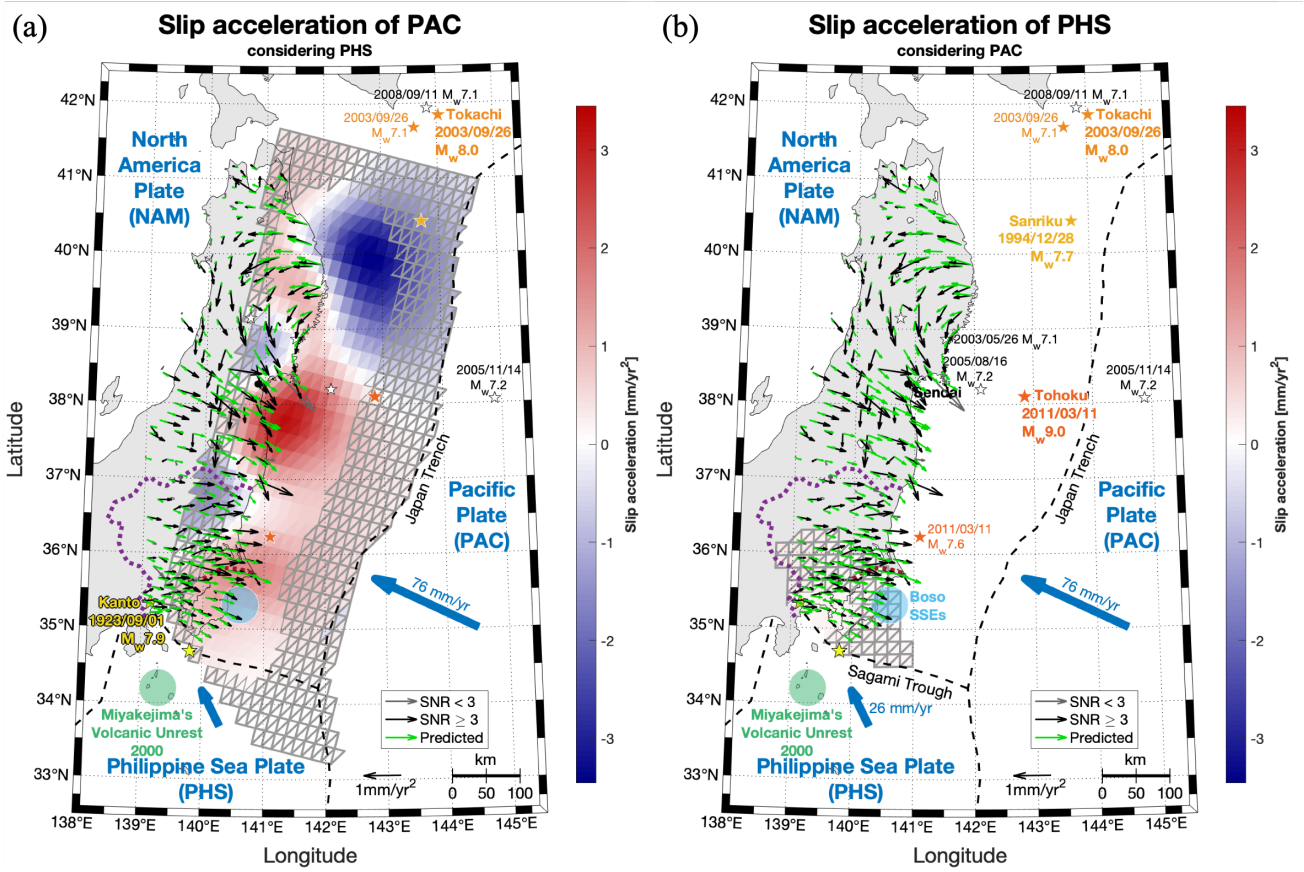

Figure S11. Slip acceleration of the Pacific (PAC) plate (a) and the Philippine Sea (PHS) plate (b) for the 2-plate inversion. Same legend as Figure 5.

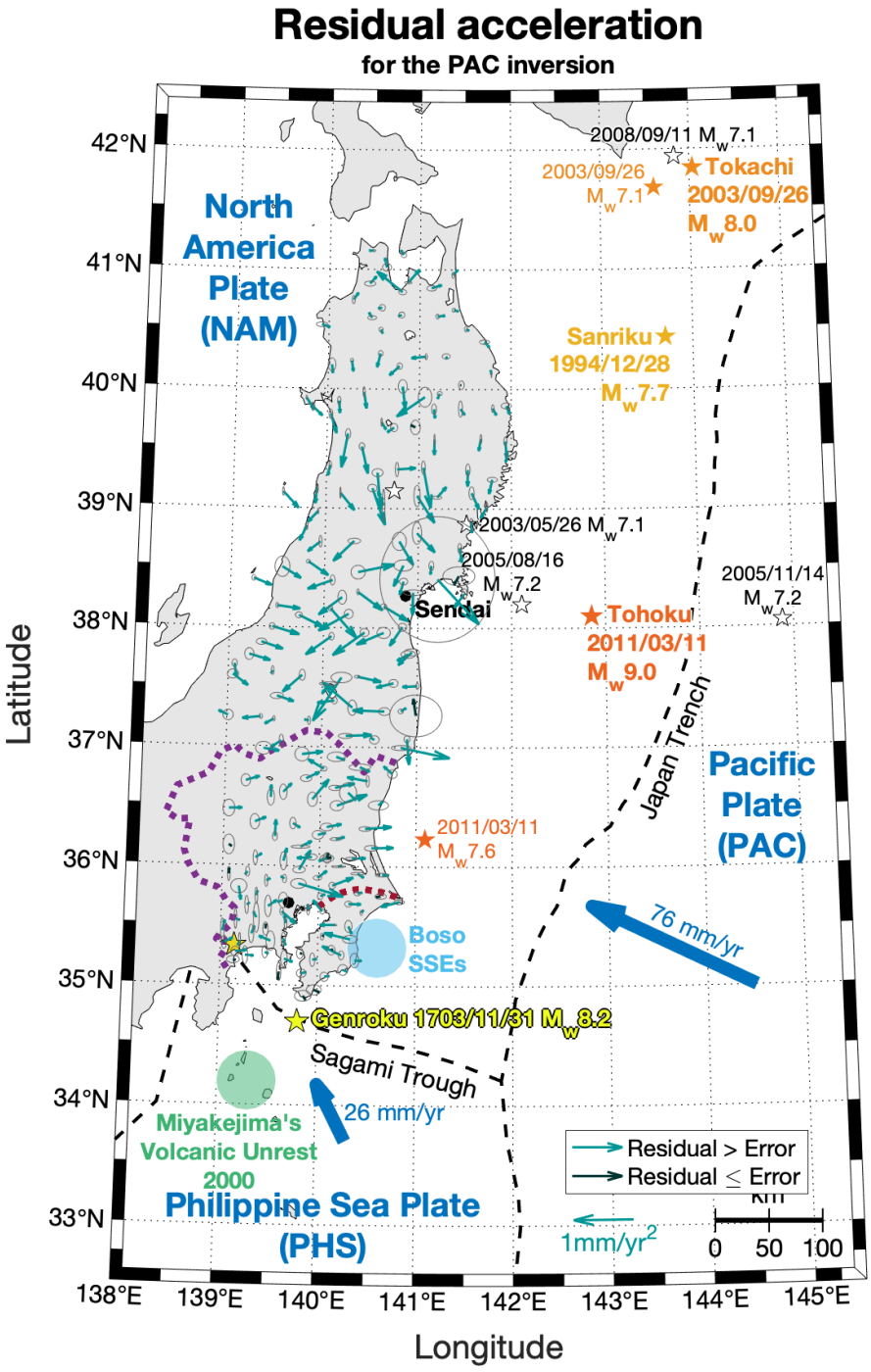

Figure S12. Residuals of the acceleration field inversion of the Pacific (PAC) plate. The error ellipse of the horizontal acceleration are shown for each station , as well as the residuals between the acceleration field (black, gray arrows in Figure 5) and the predicted surface acceleration (green arrows in Figure 5). The light arrows correspond to residuals higher than the acceleration error, and dark, to residuals small or equal to the acceleration error.

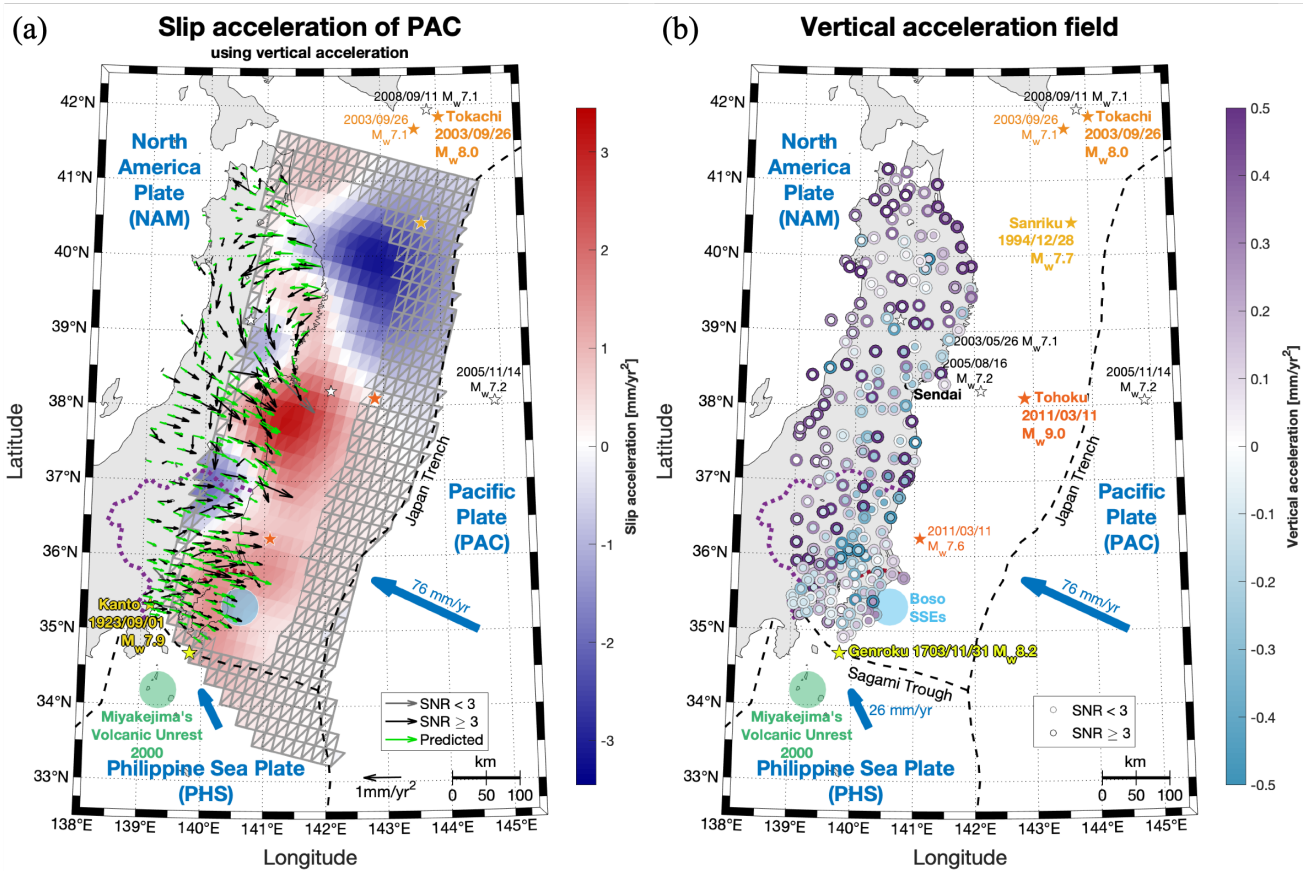

Figure S13. Slip acceleration of PAC accounting for vertical displacement. (a): Horizontal acceleration and slip acceleration; same legend as Figure 5. (b): Vertical acceleration; the outer circle represent the observed vertical acceleration while the inner circle represent the predictions. We distinguish the stations which have a signal-to-noise ratio greater than 3 (black contour), and those which fail to meet this criterion (grey contour, see Section 3.4); other elements are described in Figure 1.

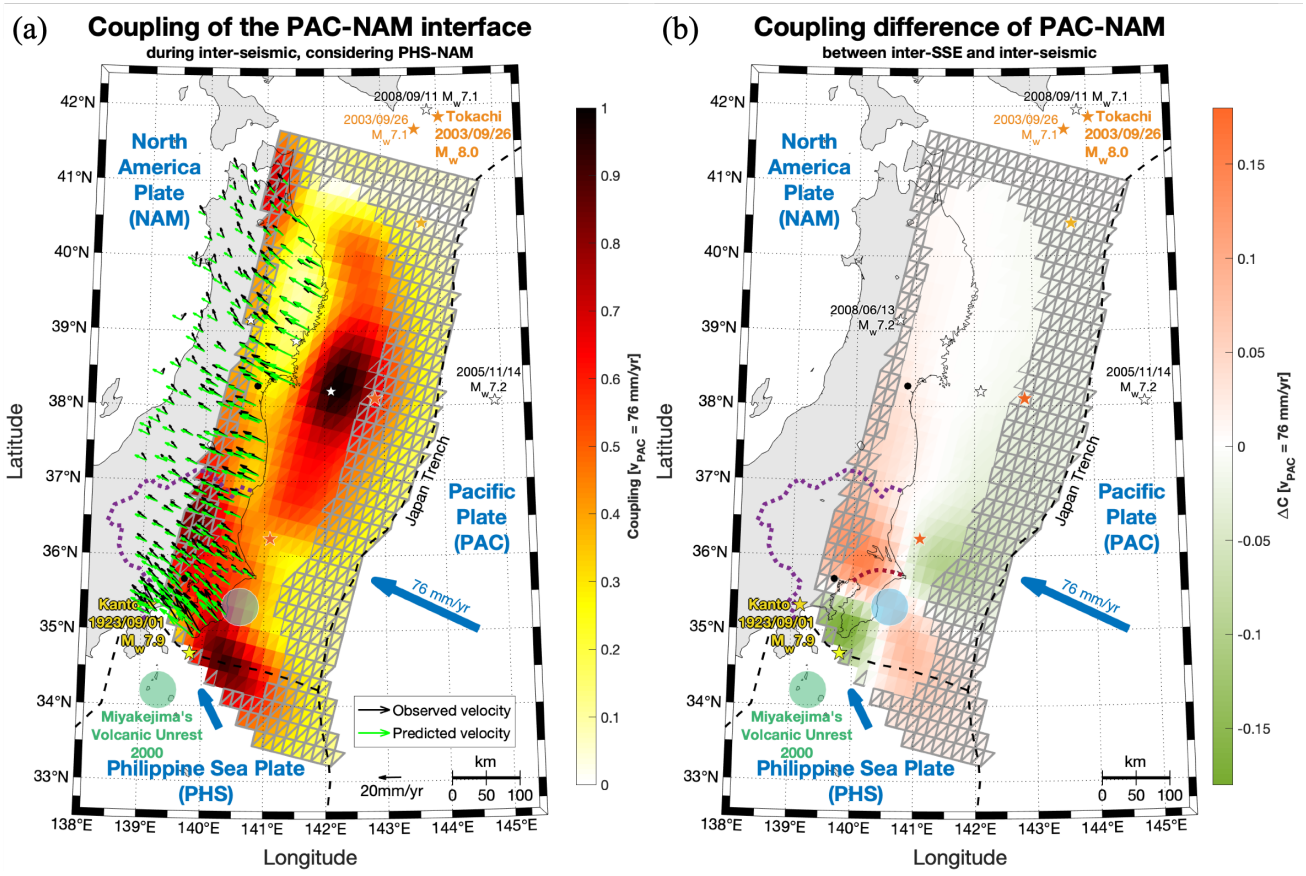

Figure S14. Impact of the Boso SSEs correction on the Pacific-North America (PAC-NAM) subduction interface coupling. (a): Inter-seismic coupling (for time series analysis without SSE modeling); same legend as Figure 4. (b): Coupling difference between inter-SSE coupling (Figure 4a) and inter-seismic coupling (a); orange: sub-fault more coupled with the Boso SSEs correction; green: sub-fault less coupled with the Boso SSEs correction; other elements are described in Figure 1.

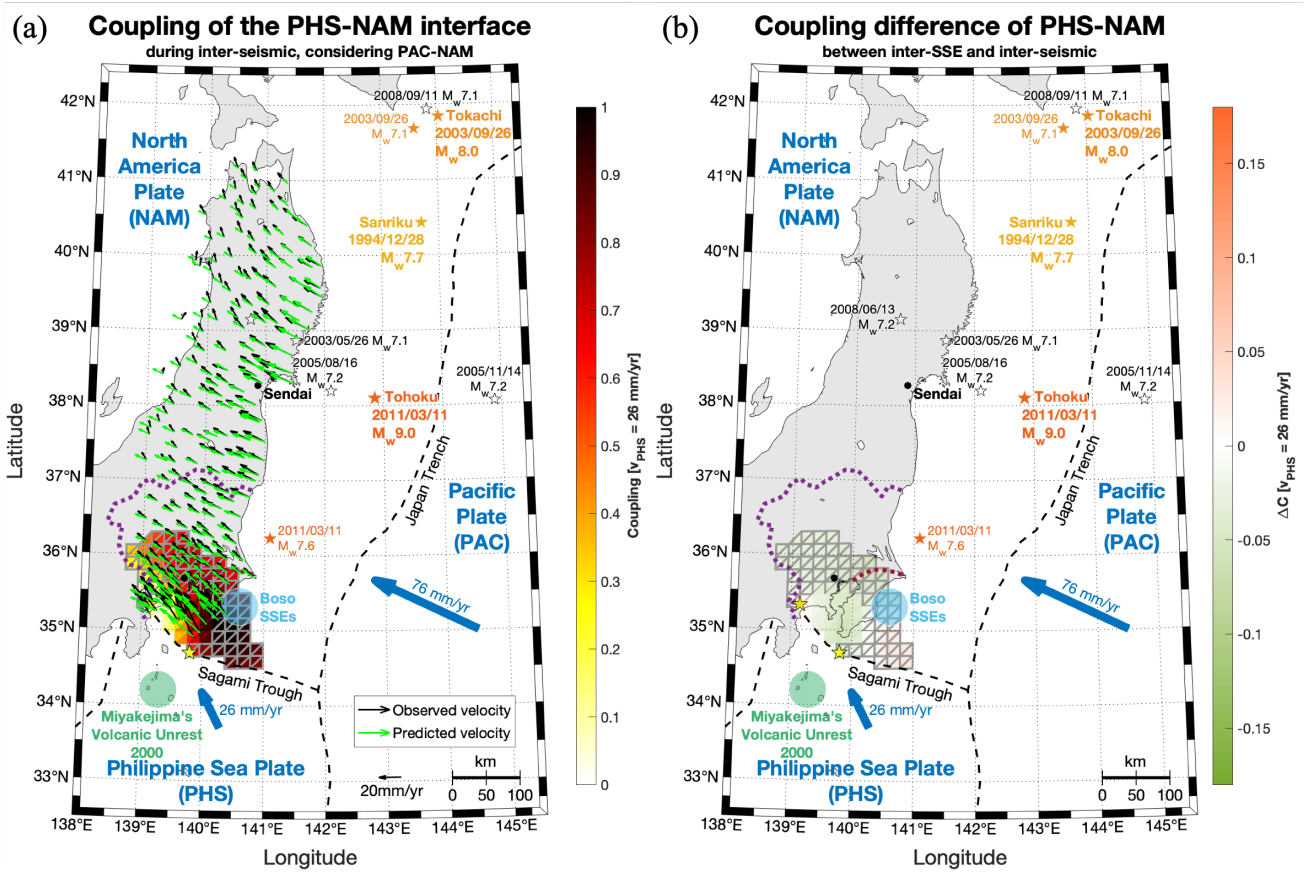

Figure S15. Impact of the Boso SSEs modelling on the Philippine Sea-North America (PHS-NAM) subduction interface coupling. (a): Inter-seismic coupling (for time series analysis without SSE modeling). (b): Coupling difference between inter-SSE coupling (Figure 4b) and inter-seismic coupling (a). Same legend as Figure S14.

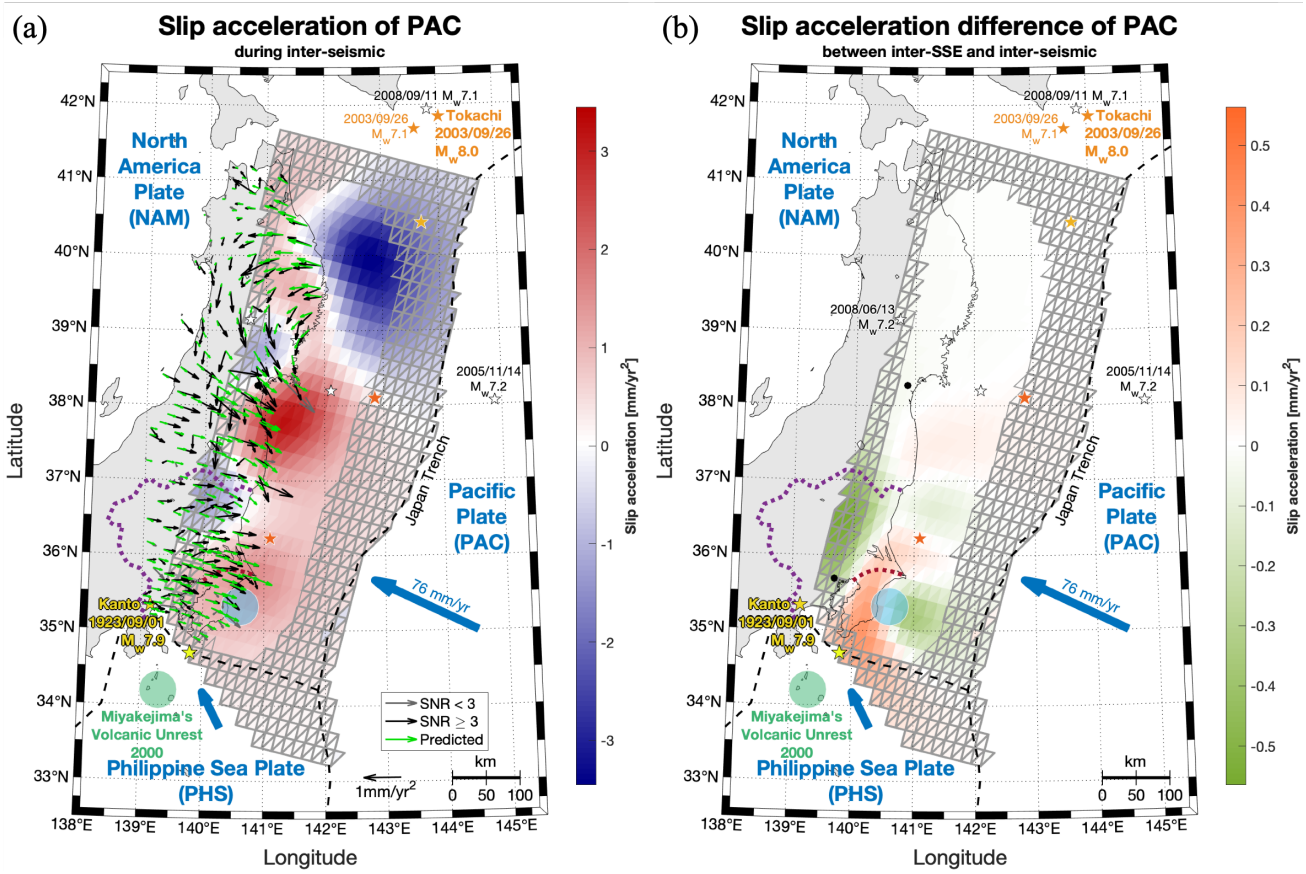

Figure S16. Impact of the Boso SSEs modelling on the Pacific (PAC) plate slip acceleration. (a): Inter-seismic slip acceleration (for time series analysis not modeling SSE); same legend as Figure 5. (b): Difference between the inter-SSE slip acceleration (Figure 5) and the inter-seismic slip acceleration (a).

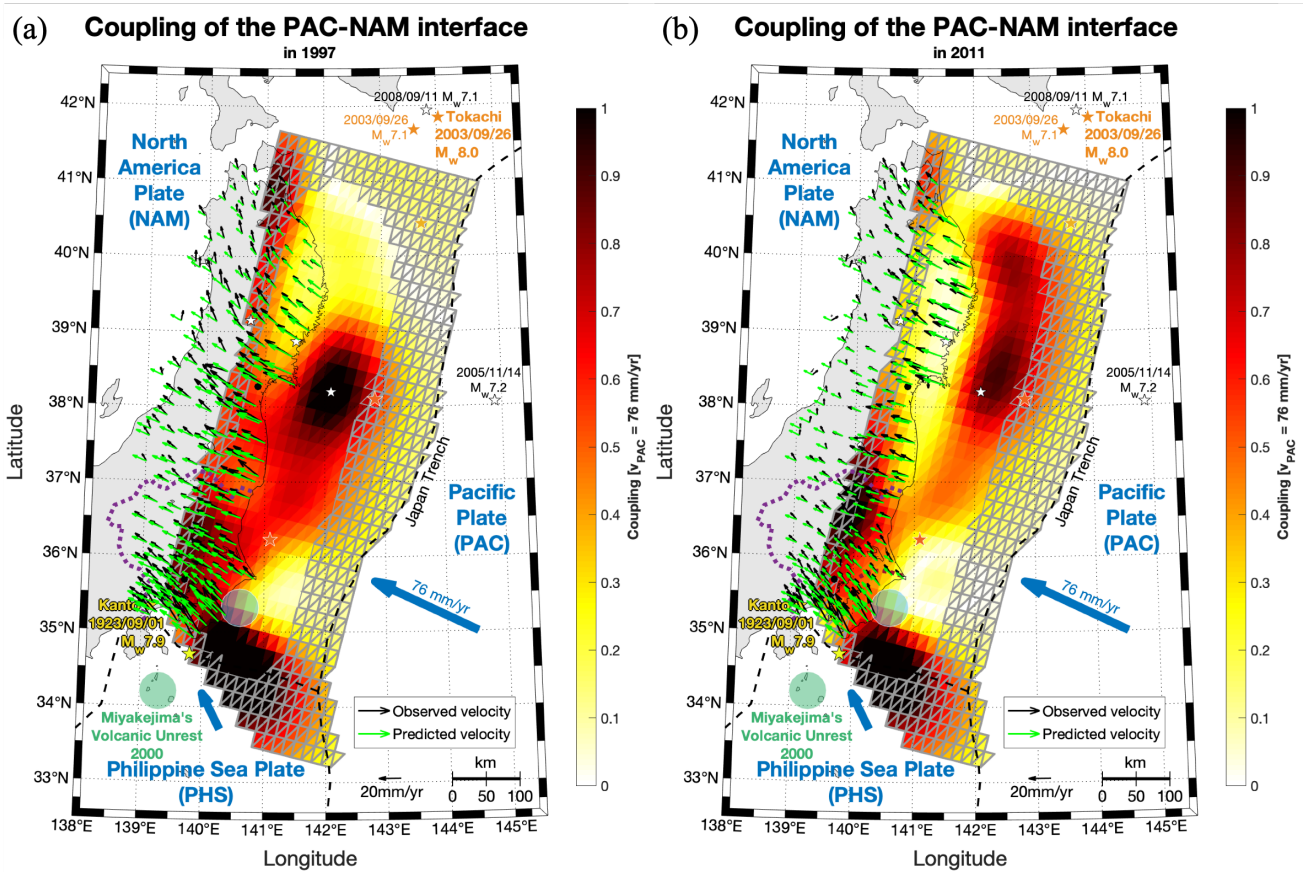

Figure S17. Coupling of the Pacific-North America (PAC-NAM) subduction interface in 1997 (a) and 2011 (b). Same legend as Figure 4.

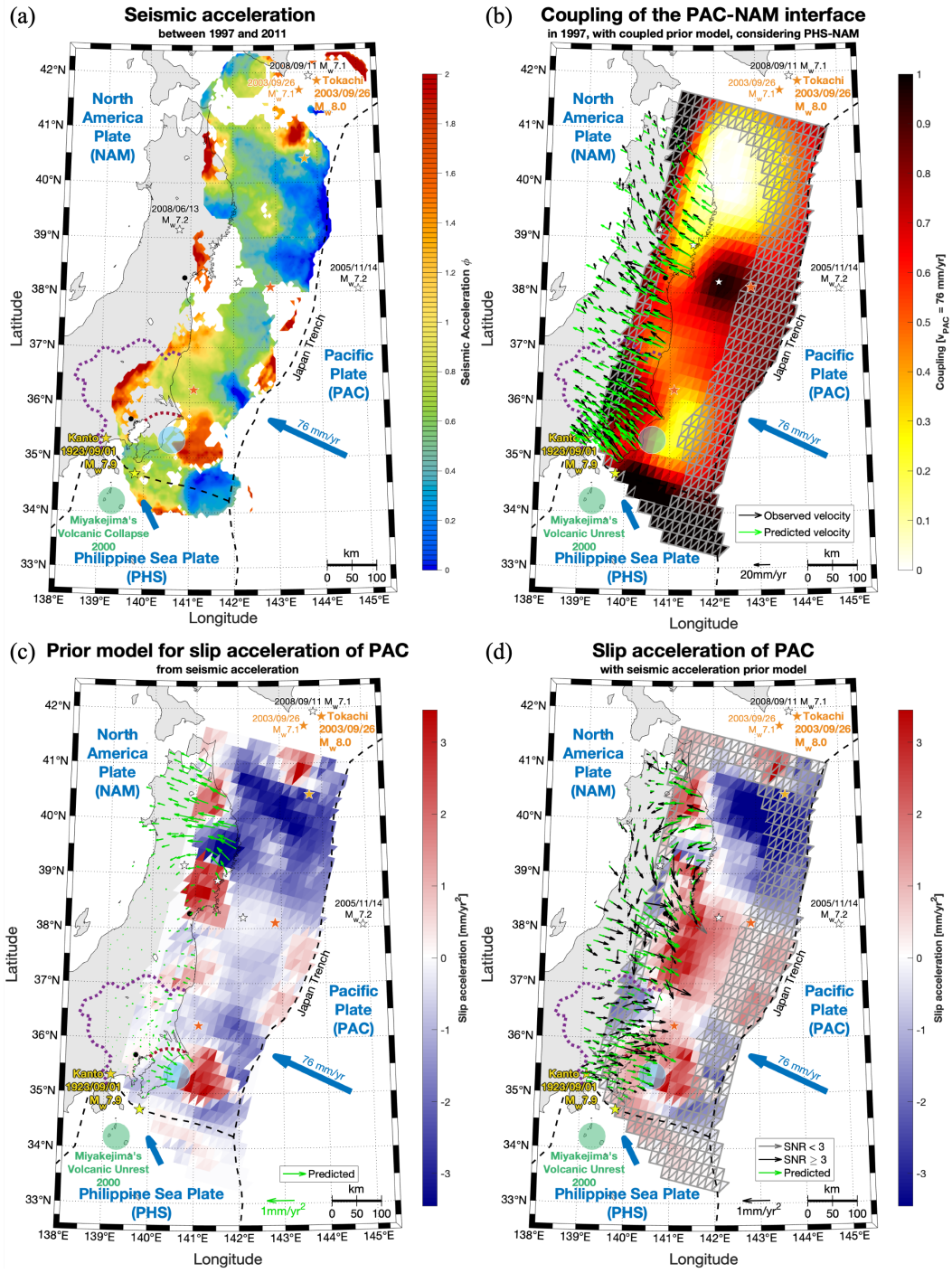

Figure S18. Seismic acceleration on the Pacific (PAC) plate between 1997 and 2011 as slip rate acceleration prior. (a): Seismic acceleration of the Pacific (PAC) plate between 1997 and 2011. (b) Coupling of the Pacific-North America (PAC-NAM) interface. (c): Prior slip acceleration model of the PAC plate based on the seismic acceleration (a) and the coupling (b) with Equation (18). (d): Slip acceleration of the PAC plate. Same legend as Figure 8.